Synthesis of Al-α-Fe_2O_3/rGO Nanostructures for Plasmon-Enhanced Photocatalytic Herbicide (2,4-D) Degradation and Hydrogen Production via PEC Water Splitting

Ayana Fikadu Gonfa

A Thesis Submitted to the Department of Applied Chemistry
College of Applied Natural Science

Presented in Partial Fulfillment of the Requirement for the Degree of Mas ter's in Applied Chemistry (Physical Chemistry)

Office of Graduate Studies
Adama Science and Technology University

October, 2025
Adama, Ethiopia

Synthesis of Al-α-Fe_2O_3/rGO Nanostructures for Plasmon-Enhanced Photocatalytic Herbicide (2,4-D) Degradation and Hydrogen Production via PEC Water Splitting

Ayana Fikadu Gonfa

Main Advisor: Lemma Teshome (Ph.D.)

Co-Advisor: Bedasa Abdisa (Ph.D.)

A Thesis Submitted to the Department of Applied Chemistry

College of Applied Natural Science

Presented in Partial Fulfillment of the Requirement for the Degree of Master's in Applied Chemistry (Physical Chemistry)

Office of Graduate Studies

Adama Science and Technology University

October, 2025

Adama, Ethiopia

DECLARATION

I confirm that the thesis entitled "**Synthesis of Al-α-Fe_2O_3/rGO Nanostructures for Plasmon-Enhanced Photocatalytic Herbicide(2,4-D) Degradation and Hydrogen Production via PEC Water Splitting** " is my own work and has not been presented to any other university for similar objectives. The sources referred to in this thesis have been duly acknowledged with proper citations.

Ayana Fikadu _____ _____

Name of student Signature Date

\

RECOMMENDATION OF ADVISORS

We, the advisors of this thesis work, hereby certify that we have closely advised the student while developing the proposal and have read the draft thesis work, "**Synthesis of Al-α-Fe_2O_3/rGO Nanostructures for Plasmon-Enhanced Photocatalytic Herbicide(2,4-D) Degradation and Hydrogen Production via PEC Water Splitting**," prepared under our guidance by Ayana Fikadu. Therefore, we recommend submission of the thesis work to the department for further review and evaluation.

Lemma Teshome (PhD)	_____	_____
Major Advisor	Signature	Date
Bedasa Abdisa (PhD)	_____	_____
Co-advisor	Signature	Date

APPROVAL SHEET

We hereby certify that the recommendations and suggestions given by the thesis review committee are appropriately incorporated into the final thesis entitled "**Synthesis of Al-α-Fe_2O_3/rGO Nanostructures for Plasmon-Enhanced Photocatalytic Herbicide (2,4-D) Degradation and Hydrogen Production via PEC Water Splitting**" by Ayana Fikadu.

Major Advisor	Signature	Date
Lemma Teshome (PhD)	_____	_____
Co-advisor	Signature	Date
Bedasa Abdisa (PhD)	_____	_____

We, the undersigned, members of the Board of Reviewers of the thesis open defense by **Ayana Fikadu,** have read and evaluated the thesis entitled "**Synthesis of Al-α-Fe_2O_3/rGO Nanostructures for Plasmon-Enhanced Photocatalytic Herbicide (2,4-D) Degradation and Hydrogen Production via PEC Water Splitting**" and assessed the understanding of the candidate about the research work. This is, therefore, to certify that the thesis is accepted, and we recommend the implementation of this thesis.

Gemechu Deressa (PhD)	_____	_____
Chairperson	Signature	Date
Fedlu Kedir (PhD)	_____	_____
Internal Examiner	Signature	Date
Getachew Adam (PhD)	_____	_____
External Examiner	Signature	Date

Final approval and acceptance of the thesis is contingent upon submission of its final copy to the Office of Postgraduate Studies (OPGS) through the Department Graduate Council (DGC) and College Graduate Committee (CGC).

_____	_____	_____
Department Head	Signature	Date
_____	_____	_____
College Dean	Signature	Date
_____	_____	_____
Office of Postgraduate Studies, Dean	Signature	Date

ACKNOWLEDGEMENT

Above all, I want to express my gratitude to Almighty God for his protection, strength, ability and guidance in all aspects of my study. Next, I would like to express my thanks to my advisors, Lemma Teshome (PhD) and Bedasa Abdisa (PhD), for your invaluable and tireless efforts in supporting, constructive comments and sharing valuable professional experience in correcting my mistakes to write this thesis. I am also thankful head of the Department of Chemistry, Gemechu Deressa (PhD), for His leadership and continuous encouragement during my study. I would also like to express my gratitude to my family for their constant motivation and support throughout the course of my studies. I thank the staff and faculty members of the Chemistry Department for providing me with the necessary resources and facilities to carry out research. My sincere gratitude goes to my friends and colleagues, whose advice and arguments have shaped my thoughts on this research. Lastly, I would like to thank Adami Tulu Pesticide Processing Factory for providing my study with the 2,4-D analytical standard.

TABLE OF CONTENTS

LIST OF ACRONYMS AND ABBREVIATIONS

2,4-D	2,4-dichlorophenoxyacetic acid
BET	Brunauer-Emmett-Teller
CA	chronoamperometry
CV	cyclic voltammetry
EIS	electrochemical impedance spectroscopy (EIS)
FTIR	Fourier transform infrared
LSPRs	localized surface plasmon resonances
LSV	linear sweep voltammetry
NNPMs	non-noble plasmonic metals
PEC	photoelectrochemical
PL	Photoluminescence
PV	photovoltaic
rGO	reduced graphene oxide
ROS	reactive oxygen species
SC	semiconductor
SEM-EDX	scanning electron microscopy-energy dispersive X-ray
UV	ultraviolet
UV-DRS	ultraviolet-diffuse reflectance spectroscopy
XPS	X-ray photoelectron spectroscopy
XRD	X-ray diffraction

LIST OF FIGURES

LIST OF TABLES

ABSTRACT

This study mainly focused on the synthesis of Al-α-Fe_2O_3/rGO nanostructure through the sol-gel method with sonication route, followed by characterization for photocatalysts degradation of 2,4-dichlorophenoxyacetic acid (2,4-D) and hydrogen production via photoelectrochemical (PEC) water splitting. The morphology, optical, structural properties, elemental composition and electrochemical properties of the prepared nanomaterial were investigated using X-ray diffraction (XRD), field emission scanning electron microscopy (FESEM), energy dispersive X-ray (EDX), X-ray photoelectron (XPS), Fourier transform infrared (FTIR), Brunauer-Emmett-Teller, photoluminescence (PL), ultraviolet-visible spectroscopy (Uv-Vis), electrochemical impedance spectroscopy (EIS), linear sweep voltammetry (LSV), cyclic voltammetry (CV) and chronoamperometry (CA) techniques and confirmed the successful formation of crystalline hematite, lattice incorporation of Al^{3+}, and intimate contact with reduced graphene oxide (rGO). The photocatalytic activity of Al-α-Fe_2O_3/rGO nanostructure was evaluated by degrading 2,4-D under visible light, achieving 93.95% removal efficiency within 60 minutes. While the PEC water splitting to produce hydrogen of Al-α-Fe_2O_3/rGO nanostructure tested in 1 M NaOH and delivered photocurrent density of 3.12 mA/cm² at 1.23 V vs RHE, which is 22.28 times higher than bare α-Fe_2O_3, and exhibited excellent stability over 35,000 seconds under continuous illumination. The enhanced attributes that Al doping improve charge separation and reduce recombination, through a plasmonic enhancer by inducing localized surface plasmon resonance (LSPR) that increases visible light absorption and promotes hot electron generation. Coupling with rGO provides an efficient charge transport pathway and results in high electrical conductivity. These findings indicate the potential of Al-α-Fe_2O_3/rGO nanostructures as efficient, stable, and low-cost plasmon-enhanced photocatalysts for environmental remediation and solar-driven PEC hydrogen production

***Key Word**: 2,4-dichlorophenoxyacetic acid (2,4-D), Al-α-Fe_2O_3/rGO nanostructure, hydrogen production, localized surface plasmon resonance (LSPR), photoelectrochemical (PEC), water splitting*

CHAPTER ONE

INTRODUCTION

1.1 Background of the study

The modern world faces the dual crises of upcoming climate change, driven by fossil fuel combustion, and widespread environmental contamination from industrial and agricultural activities (Singh, 2021). Global warming, mainly caused by emissions of CO_2 from burning fossil fuels, is estimated to have potentially serious consequences for the environment (Hosseini, 2022). Simultaneously, environmental contamination, by persistent herbicides like 2,4-dichlorophenoxyacetic acid (2,4-D), which are highly used in agriculture, poses to the environment and human health due to its harmful effects and ability to persist in the soil and water (Meftaul *et al.*, 2020). Thus, to achieve environmental cleanup and sustainability, it is necessary to promote the technologies of clean hydrogen production and the sufficient degradation of pollutants, such as 2,4-dichlorophenoxyacetic acid (2,4-D).

Hydrogen (H_2), an energy carrier with many uses, is regarded as among the most encouraging sources of renewable energy for addressing numerous energy concerns, and has recently gained remarkable attention, because of its high gravimetric energy density, potential for use with current industrial infrastructure, and almost zero greenhouse gas emissions, hydrogen (H_2) is considered the foremost possibility for replacing hydrocarbon fuels contribute to global warming, ozone layer depletion, and environmental pollution (Sharma *et al*., 2021; Song *et al*., 2022).

While hydrogen presents a clean energy solution, water pollution through persistent chemicals is a serious issue. Addressing challenges like water contamination has lot of attention due to its harmful impacts on both human health and the ecosystem (Singh *et al*., 2024). The growth of agricultural activity and the widespread use of herbicides contribute to residual in water (Jorfi *et al*., 2021). 2,4-dichlorophenoxyacetic acid (2,4-D) is the main active ingredient in about 1,500 herbicide marketed products (Malindzisa, 2022). The 2,4-D is commonly used for systemic herbicides controlling mainly broad-leaf weeds. Because 2,4-D has a lengthy half-life, there is a lot of time for it to spread to surface and subsurface water and cause problems in both humans and animals.

The concentration of 2,4-D must be eliminated from water due to its high solubility and association with numerous diseases, such as cancer, liver, renal and endocrine problems (Mohd Ghazi *et al*., 2023). Various methods have been employed to remove 2,4-D from aqueous solutions using a variety of methods, including adsorption (Fernandez *et al.*, 2022), biological degradation (Dargahi, Shokoohi, *et al.*, 2021), chemical oxidation and photocatalytic degradation (Girón-Navarro *et al.*, 2021). Photocatalytic degradation has gained valuable attention due to its environmentally friendly, clean, and green technology. In this process, a semiconductor photocatalyst uses light energy to generate highly reactive species (ROS), superoxide radicals(O_2^-) and hydroxyl radicals ($OH^•$), which can mineralize persistent organic pollutants (Girón-Navarro *et al.*, 2021). Nevertheless, the currently available techniques of treating 2,4-D have shortcomings such as partial degradation, high energy requirement or secondary pollution. Therefore, the current research aims to develop effective, visible-light-active, low-cost photocatalysts, i.e., Al-α-Fe_2O_3/rGO nanostructures, that could be effective in removing 2, 4-D and, at the same time, be environmentally friendly. Many naturally occurring resources, such as water (H_2O), hydrocarbons (like methane, or CH_4), and other organic compounds, are convertible to hydrogen. Currently, coal gasification, methane partial oxidation, and steam methane reforming generate over 90 % of the world's H_2 from fossil fuels, resulting in annual emissions of over 830 million tons of CO_2, or more than 2% of global CO_2 emissions ((Matus *et al.*, 2022). As a result, the potential contribution of H_2 fuels produced by traditional fossil-fuel-based approaches to mitigating global warming is insignificant or even negative. Hence, there is a need to establish viable solutions to produce H_2 with minimum or no carbon emission (Sánchez-Bastardo *et al*., 2021).

Solar energy is a widespread, renewable energy source for sustainable H_2 generation (Song *et al.*, 2022). There are numerous strategies for hydrogen production, including photoelectrolysis, photoelectrochemical, and photocatalytic (Song *et al.*, 2022), and these techniques have minimal emissions and are more environmentally friendly than other methods, according to Dincer and Acar (Karaca, 2023). According to Hosseini and Wahid, the photoelectrochemical (PEC) method is an appropriate choice for producing hydrogen due to its direct conversion from renewable energy sources, through water splitting (Hosseini & Wahid, 2020). In PEC, the photoanode consists of photoactive (light-responsive) light-absorbing semiconductor material that creates an electron-hole pair. The excited electron moves to the cathode, which is primarily

composed of Pt mesh, and interacts with the H^+ ions in the solution to produce H_2, while the corresponding hole oxidizes hydroxide ions to O_2 (Wyżga *et al.*, 2024).

Photocatalyst semiconductor metal oxides are frequently employed in photocatalysis. Since Fujishima and Honda introduced TiO_2 as a photoanode and a Pt counter electrode in PEC water splitting, other photoelectrode materials have been created in large numbers and include metal oxides such as TiO_2, Fe_2O_3, WO_3, and $BiFeO_3$(Amano, 2021). The photocatalytic activities of nanoparticles, such as TiO_2, SnO_2, WO_3, CeO_2, Fe_2O_3, Bi_2O_3, ZnO, Ag-based photocatalyst (Gao *et al*., 2022) under investigation in their photocatalytic studies in the visible and ultraviolet light irradiation. It is no secret that titanium dioxide (TiO_2) is a superior choice for photocatalytic degradation, as it is cheap, stable, non-toxic, and a highly efficient semiconductor (Gatou *et al.*, 2024). Moreover, the application of TiO_2 in the ultraviolet (UV) light is not as applicable, as the material has a relatively large band gap (about 3.2 eV), constituting approximately 4% of the solar spectrum, to activate (Gatou *et al*., 2024).

To overcome this limitation, researchers have turned to materials that can utilize visible light. Hematite (α-Fe_2O_3) is one of the semiconductor materials that is gaining a lot of attention for applications using visible light-driven photocatalysis (Wan *et al.*, 2023). Fe_2O_3 is of considerable interest due to its natural abundance, chemical stability in aqueous media, low cost, nontoxicity, and small bandgap (~2.1eV) (which absorbs a large portion of the visible solar spectrum (46%), making it suitable for photocatalytic water treatment and photoelectrochemical splitting applications (Wan *et al.*, 2023). However, the photocatalytic performance of α-Fe_2O_3 is limited due to poor electrical conductivity, high electron-hole recombination and short hole diffusion lengths (2-4 nm), resulting in lower photoactivity and a higher overpotential for PEC water splitting (Huang *et al*., 2023).

To overcome these limitations, an innovative approach is needed to improve hematite's electrical conductivity and electron-hole recombination separation efficiency. There are numerous investigations have been developed, for modification of Fe_2O_3, including elemental doping (Tamboli *et al*., 2022), Plasmonic modification (Mammar & Hamadou, 2023) morphology control (Liu *et al.*, 2017), surface modification and nanostructuring (Yuan *et al*., 2020), composite formation(Sun *et al*., 2021), and heterostructures formation (Synowiec *et al*., 2023) Plasmonic photocatalysts improve solar-to-chemical conversion by increasing light absorption through surface plasmon resonance (SPR), powerful localized electromagnetic fields are created

close to excited plasmonic nanostructures, which promote of electron-hole pairs on the surface of the photocatalyst, and injecting energetic “hot electrons” to drive interfacial chemical reactions (Amirjani *et al.*, 2023).

Recent studies have focused on combining plasmonic photocatalysts made of noble metals, including Ag and Au, with semiconductor materials to improve the performance of photocatalytic (Li *et al*., 2021). However, the limited range of SPR tuning and the high cost of those noble metals prevent them from being widely used (Li *et al*., 2021). Non-noble plasmonic metals (NNPMs) have been suggested as substitutes for noble-metal plasmonics, since they are naturally abundant, inexpensive, and have tunable SPR properties that span a broad spectral which has range from UV to IR. These NNPMs include cobalt (Co), nickel (Ni), magnesium (Mg), aluminium (Al), copper (Cu), and bismuth (Bi).(Sayed *et al*., 2022). For example, aluminium (Al) is 2×10^7 and 1×10^6 times more abundant in the earth's crust than Au and Ag, but costs 2.5×10^4 and 290 times less, respectively (Sayed *et al*., 2022).

A sustainable and efficient way to improve photocatalytic performance is to combine non-noble plasmonic metals (NNPMs), like aluminium (Al), with a photocatalyst like α-Fe_2O_3.(Liu *et al.*, 2023). This effect can be further combining the composite with reduced graphene oxide (rGO) sheets because of their high electrical conductivity. rGO is a solid-state electron bridge, which can readily receive hot electrons, either α-Fe_2O_3 or Al, and transmit them to the reaction sites, making the process more efficient and fewer charge recombination(Sim *et al*., 2022).

Therefore, this research aims to address critical challenges in both clean energy production and environmental remediation by synthesizing a nanostructured material that will allow improved photocatalytic activity and the economic viability of non-noble, inexpensive metals.

1.2 Statement of the Problem

The widespread use of 2,4-dichlorophenoxyacetic acid (2,4-D) in agriculture has led to persistent contamination of water and soil, posing a severe hazard to ecosystems and human health. Conventional treatment methods, including physical, chemical, and biological approaches, are limited by incomplete pollutant mineralization, high energy demand, generation of hazardous by-products. Also, the increasing demand to use clean and sustainable energy is a strong indication of the urgent necessity of effective hydrogen (H_2) production technologies. Current methods of hydrogen production are heavily based on fossil fuels and contribute to high

levels of CO_2 emissions and climate change. Solar photocatalysis and photoelectrochemical water splitting offer a clean, sustainable alternative for both environmental remediation and sustainable energy. However, its practical application is hindered by high electron-hole recombination rates, poor charge carrier mobility (low electrical conductivity), and high overpotential, which makes increased energy consumption requirements for water splitting, resulting in low efficiency in conventional semiconductor materials like hematite (α-Fe_2O_3). Recent developments in plasmonic nanostructures have demonstrated potential effects to overcome these limitations by improving visible-light absorption and charge carrier dynamics via localized surface plasmon resonance (LSPR). However, the prevalent plasmonic systems are based on the expensive noble metals such as Au and Ag, limiting their high cost rarely restricts large-scale use applications.

Therefore, low-cost, earth-abundant non-noble metal, plasmonic nanostructure such as aluminium (Al), with α-Fe_2O_3 coupled with reduced graphene to enhance photocatalytic activity and stability. This research addresses this gap by focusing on the development of a novel Al-α-Fe_2O_3/rGO nanostructure, a material designed for improved light absorption, charge separation, and stability to enhance the dual challenges of 2,4-D degradation and sustainable hydrogen production.

1.3 Objectives of Study

1.3.1 General Objective

To synthesis and characterize of Al-α-Fe_2O_3/rGO nanostructures for plasmon-enhanced photocatalytic herbicide (2,4-D) degradation and hydrogen production

1.3.2 Specific Objectives

- To synthesize Al-α-Fe_2O_3/rGO nanostructures via the sol-gel method.
- To characterize the synthesized Al-α-Fe_2O_3/rGO nanostructures by analyzing the structural, optical, and morphological properties.
- To evaluate the photocatalytic efficiency of Al-α-Fe_2O_3/rGO in degrading 2,4-D herbicide
- To optimize key operational parameters (e.g., pH, catalyst dosage, and herbicide concentration).

- To evaluate the photocatalytic efficiency of Al-α-Fe_2O_3/rGO in hydrogen production through water splitting.
- To investigate the long-term stability of the Al-α-Fe_2O_3/rGO photoanode for overall PEC water splitting

1.4 Significance of the Study

The significance of this study on the synthesis of Al-α-Fe_2O_3/rGO nanostructures for plasmon-enhanced photocatalytic for degrading 2, 4-dichlorophenoxyacetic acid (2, 4-D), a common herbicide, causes considerable environmental and health concerns. and promotes sustainable hydrogen production through water splitting. The incorporation of rGO with Al-α-Fe_2O_3 enhances light absorption and charge separation, improving photocatalytic activity. This incorporation allowed the ability to use a broad spectrum of light by the LSPR technique, which facilitated effective degradation of 2, 4-D when exposed to sunlight and hydrogen production. Thus, this study aims to sustainable impact on both environmental and renewable energy by creating a high-performance, low-cost photocatalyst.

1.5 Scope of the Study

The scope of the study includes the synthesis and characterization of Al-α-Fe_2O_3/rGO nanostructures for plasmon-enhanced photocatalysis for 2,4-D dichlorophenoxyacetic acid degradation and hydrogen production through photoelectrochemical (PEC) water splitting. The nanostructures are synthesized using cost-effective sol-gel methods. Their structural, optical, and functional properties were characterized through techniques including XRD, FE-SEM, SEM, SEM-EDS, XPS, FTIR, BET, PL, UV-DRS, UV-Vis's spectroscopy, CV, EIS, LSV and CA. Furthermore, the study evaluates the photocatalytic efficiency of Al-α-Fe_2O_3/rGO for 2,4-D degradation and hydrogen production by photoelectrochemical (PEC) water splitting.

CHAPTER TWO

LITERATURE REVIEW

2.1 Overview of Photocatalytic Water Splitting and Degradation.

Photocatalysts are nanomaterials having semiconducting properties, including light absorption, charge transfer, and a favorable electronic structure (Feliczak-Guzik, 2022). Photocatalytic degradation regime in which a semiconductor photocatalyst, like Fe_2O_3, CdS, ZnO, WO_3, ZnS, ZrO_2, and TiO_2, absorbs photon energy (hv) equal to or higher than its bandgap, enabling electrons to migrate from the valence band to the conduction band and form pairs of electrons and holes (Navidpour *et al.*, 2023). These charge carriers undergo redox reactions with adsorbed species, producing ROS such as superoxide anions (O_2^-) and hydroxyl radicals (·OH) and damage organic compounds. pollutants like herbicides into harmless products (CO_2, H_2O and other byproducts) (Adfar *et al*., 2025).

In PEC water splitting, a semiconductor photoelectrode absorbs light to the production of charge carriers that engage in oxidation and reduction processes at different electrodes. The photoanode oxidized water to oxygen, while the cathode reduced protons to hydrogen (Xi & Liu, 2025). Efficient charge separation and extraction are necessary for producing sustainable hydrogen fuel utilizing solar energy.

2.2 Properties and Challenges of Fe_2O_3 (Hematite) Nanostructure

Iron oxide is available in several stoichiometric and crystalline forms, such as hematite (α-Fe_2O_3), magnetite (Fe_3O_4), wustite (FeO), and maghemite γ-Fe_2O_3 (Busti *et al*., 2021). α-Fe_2O_3 (hematite) is a rhombohedral-centered corundum hexagonal structure (isostructural with a-Al_2O_3), the oxygen lattice is densely packed with two-thirds of the octahedral positions occupied by Fe^{3+} ions. α-Fe_2O_3 belongs to the *R*3c space group and has lattice parameters of a = 5.0356 Å and c = 13.7489 Å with the most stable iron oxide in the ambient atmosphere (Lai *et al*., 2022). Hematite's red appearance is primarily due to its indirect bandgap, which typically ranges from about 2.0 eV to 2.3 eV, corresponding to wavelengths between 625 and 564 nm (Liu, 2023). This bandgap energy enables hematite (Fe_2O_3) to absorb visible light in the red region,

which gives it its characteristic red color (Busti *et al*., 2021; Liu, 2023). Hematite (α-Fe_2O_3) nanoparticles are widely studied, because of, its excellent light absorption behavior in the visible light region, availability, non-toxicity, and low bandgap (2 to 2.3 eV), stable phase of iron (III) oxide, which crystallizes and it is considered a promising material use in environmental (organic pollutant degradation) and energy applications(PEC water splitting) due to its high visible absorption, high stability in alkaline solution (Busti *et al*., 2021)

However, α-Fe_2O_3's low quantum efficiency limits its application in photocatalytic degradation and PEC fields. Hematite's high electron-hole pair recombination rates (Lai *et al*., 2022), low conductivity($\sim 10^{-14}\ \Omega^{-1}\ cm^{-1}$) (Mehralipour *et al*., 2023), and short hole diffusion length (recombination distance 2 -4 nm) are commonly attributed to this phenomenon (Vinayagam *et al*., 2022).

2.2.1 Strategies to Enhance the Photoactivity of Hematite

To overcome these challenges, numerous investigations have been developed, including elemental doping (Tamboli *et al*., 2022), plasmonic modification (Mammar & Hamadou, 2023) morphology control (Liu *et al.,* 2017), surface modification and nanostructuring(Yuan *et al*., 2020), composite formation(Sun *et al*., 2021), and heterostructures formation (Synowiec *et al*., 2023)**.**

Doping

Elemental doping is a widely employed modification strategy to improve the photocatalytic and PEC performance of Fe_2O_3 by altering its electronic structure and optical characteristics, enhancing charge carrier separation, and increasing conductivity (Mamun & Talukder, 2025). By directly altering its doping techniques for hematite with metal, non-metal, and oxygen-deficient elements enhance the material's properties. Various dopants have been reported for hematite photocatalytic modification strategies, like Zn, Cu (Alp, 2023), Sn, Ti ,Co, Ce (Tahir *et al*., 2021). For Example, Sn doping into Fe_2O_3 up to 5% yielded enhanced visible-light photocatalytic performance with increased carrier separation and bandgap narrowing (Popov *et al*., 2022), Cobalt (Co) doping at 4-5% into Fe_2O_3 exhibited improved photodegradation (>90%) for methylene blue dye (Kumar *et al*., 2023)

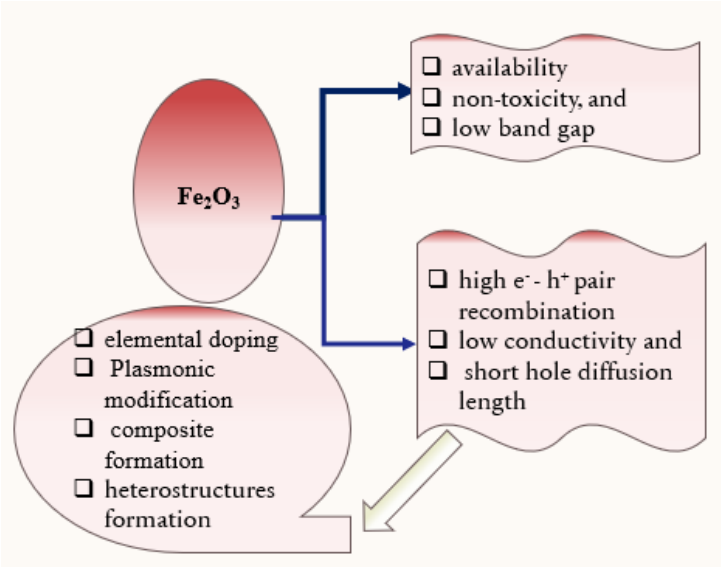

Figure 2.1. Advantages, limitations, and modification strategies of Fe_2O_3 photocatalyst

2.3 Plasmonic photocatalysts

The plasmonic photocatalysts are a class of nanomaterials that combine plasmonic metal nanoparticles, typically noble metals like Au and Ag (Zhou *et al*., 2012), and non-noble metals: Al, Cu (Jiang *et al*., 2018), with semiconductor materials to increase photocatalytic efficiency (Kumar *et al*., 2022). This innovative approach utilizes plasmonic metallic materials, which exhibit localized surface plasmon resonances (LSPRs) when exposed to light. These LSPRs significantly enhance light absorption at visible and near-infrared wavelengths and enable the generation of energetic charge carriers, thereby improving the efficiency of chemical reactions, including the degradation of pesticides and hydrogen production(Awan *et al*., 2025)

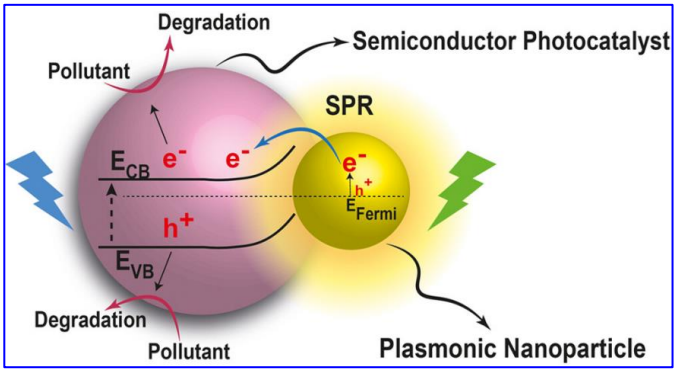

Figure 2.2. Schematic diagrams of plasmon-enhanced photocatalysis of the degradation of pollutants (Amirjani *et al*., 2023)

The optical attractive properties of plasmonic nanotechnology have attracted the attention of many scientists and technologists. Noble metal photocatalysts, including gold (Au) and silver (Ag), have been investigated based on the plasmonic nature (Stucchi *et al*., 2022). These plasmonic materials can be used in different applications, such as the degradation of pollutants and hydrogen generation using photoelectrochemical water splitting. It has been established in research studies that the plasmonic alterations with noble metals, including gold and silver, have considerable enhancements in the photocatalytic efficiency of Fe_2O_3 (Awan *et al*., 2025). As an example, Gao et al. found that a thin-film iron oxide photoanode coated on arrays of Au nanopillars improved photocurrent by optical absorption to attain the effects of SPR and photonic-mode light trapping in the nanostructured, with a net enhancement of photocurrent across the solar spectrum by up to 50 per cent (Gao *et al*., 2012). Similarly, Wang et al demonstrated that the Au-decorated Fe_2O_3 nanoflake electrodes were found to be effective as compared to bare Fe_2O_3 in the enhancement of photoactivity about water oxidation in the UV/Visible region. The Au nanoparticle decoration acted as plasmonic photosensitizers, increasing optical absorption and achieving a maximum photocurrent of 2.0 mA cm^2at 1.6 V RHE under AM 1.5 illumination in 1 M KOH (Wang *et al*., 2015).

However, while noble metals such as Au and Ag have shown remarkable plasmonic enhancement effects in Fe_2O_3 and other semiconductor photocatalysts, it limited by several factors like large-scale photocatalysis application is limited due, noble metals being rare and expensive, which makes their widespread use economically unfeasible (Sayed *et al*., 2022).

Non-noble plasmonic metals are alternatives to plasmonic material to exhibit localized surface plasmon resonances (LSPR) and improve visible to near-infrared light absorption, enabling enhanced photocatalytic efficiencies(Sayed *et al*., 2022). Those non-noble materials are earth-abundant, cost-effective options, including metals like copper, aluminium, and bismuth, along with addressing economic and sustainability concerns over noble metals. Studies highlight strategies to harness non-noble plasmonic effects for photocatalyst systems.

2.3.1 Mechanism of Non-Noble Metal Plasmonic Photocatalysts

NNPM, when coupled with a semiconductor, promotes localized surface plasmon resonance (LSPR), which is caused by the collective oscillation of conduction electrons at the metal surface

when excited by incident light of specific frequencies (Agrawal *et al*., 2018). This oscillation generates a strong, localized electromagnetic field near the metal nanoparticles**.**

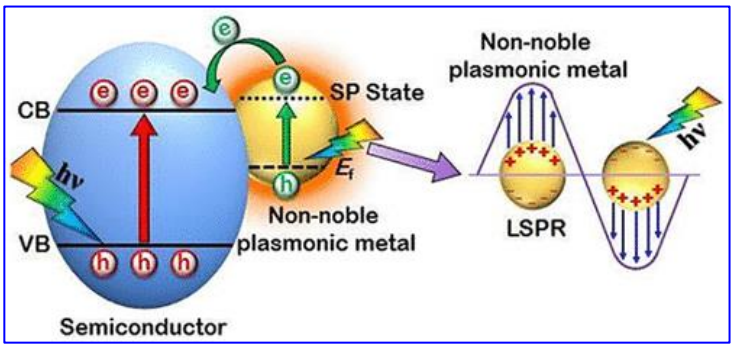

Figure 2 3. Schematic diagram for plasmon-enhanced photocatalytic mechanism in non-noble plasmonic metal (Agrawal *et al*., 2018).

The plasmonic nanoparticle absorbs light, causing its conduction electrons to oscillate and generate localized surface plasmon resonances (LSPR) through Photoexcitation (Agrawal *et al*., 2018)

$M + h\nu \rightarrow M^{*} \rightarrow e^{-}_{hot} + h^{+}$ ……...1

(Where M is the non-noble metal plasmonic nanoparticle, hν is the incident light energy, M^{*} is the excited state, e^{-}_{hot} is the hot electron, and h^{+} is the hole). The LSPR generates energetic (hot) electrons that are transferred from the plasmonic nanoparticles to the conduction band of the adjacent semiconductor are excited to higher energy states(Li *et al*., 2023).

e^{-}_{hot} →Semiconductor conduction band…….2

Semiconductor also absorbs light, energy equal to or greater than its bandgap, creating additional electron-hole pairs (e^{-} and h^{+}) that will be generated in the conduction and valence band, respectively (Sayed *et al*., 2022).

$SC + hv \rightarrow SC\ (e^{-}_{CB}) + h^{+}_{VB}$……3

The hot electrons and holes generated by both the plasmonic nanoparticle and the semiconductor are separated. The separated electrons and holes drive different chemical reactions (reduction-oxidation) on the semiconductor's surface. Electrons drive reduction reactions

$O_2 + e^- \rightarrow \cdot O_2^-$ ……4

While holes drive oxidation reactions

$H_2O + h^+ \rightarrow \cdot OH + H^+$…….5

The superoxide radical anion ($\cdot O_2^-$)and hydroxyl radical ($\cdot OH$) are highly reactive and can degrade organic pollutants such as 2, 4-dichlorophenoxyacetic acid (2, 4-D) into less harmful substances (Sayed *et al*., 2022).

Organic pollutants + $^{\bullet}OH \rightarrow$ Degraded Products……6

The photogenerated electrons reduce protons to produce hydrogen gas (H_2)

$2H^+ + 2e^- \rightarrow H_2$……7

Among non-noble metal plasmonic materials, aluminium (Al) exhibits localized surface plasmon resonance (LSPR) characteristics that are abundant, inexpensive and enhance light absorption, particularly in the visible spectrum. Research has shown that aluminium nanoparticles can effectively couple with semiconductor materials like titanium dioxide (TiO_2), significantly improving photocatalytic efficiency (Mesbah *et al*., 2020).

2.4 Synthesis Methods of Fe_2O_3

Fe_2O_3 (hematite) nanostructures can be synthesized using various methods, like physical, chemical methods and green methods

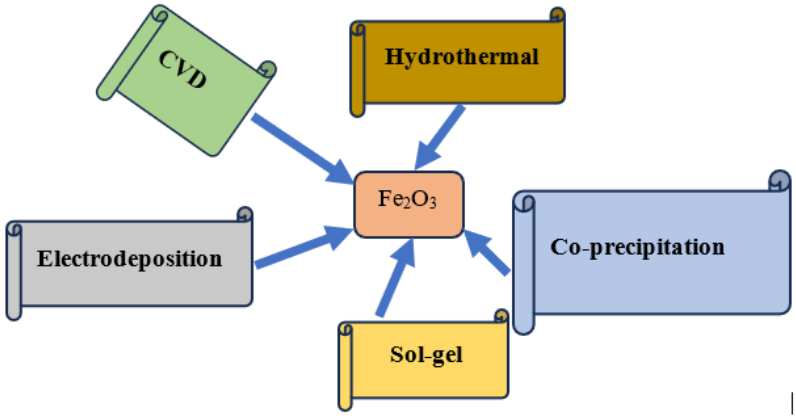

Figure 2.4. Various synthesis method of Fe_2O_3 nanostructure,

2.4.1 Hydrothermal Method

The hydrothermal synthesis of Fe_2O_3 involves chemical reactions in aqueous solution inside a sealed autoclave at elevated temperatures (typically 120–200°C) and pressures (Hang *et al.*, 2021). This method allows precise control over particle size and shape, leading to diverse nanostructures such as nanorods, nanospheres, and nanosheets with high crystallinity (Hang *et al.*, 2021). For example, hematite nanoparticle is synthesized by the hydrothermal method as follows procedure 1.8 g $Fe(NO_3)_3 \cdot 9H2O$ was dissolved in 20 ml of distilled water. To adjust the pH to approximately 9, NH_3 was added to the aforesaid solution while swirling continuously. The solution was transferred to a 25 ml stainless-steel autoclave lined with Teflon after being stirred for 20 minutes. Different temperatures were applied to the sealed tank. (80, 100, 120, and 150 1C) in an oven for 10 hours before naturally cooling to room temperature. The items were cleaned with distilled water and 100% absolute ethanol numerous times before drying at 80^0C for 12 hours (Bhat *et al.*, 2025),

2.4.2 Sol-Gel Method

The sol-gel technique is a versatile method for Fe_2O_3 nanostructure synthesis. Its mechanism was metal salt precursors undergoing hydrolysis and condensation to form a gel, then the gel is dried and calcined, yielding Fe_2O_3 nanostructure.

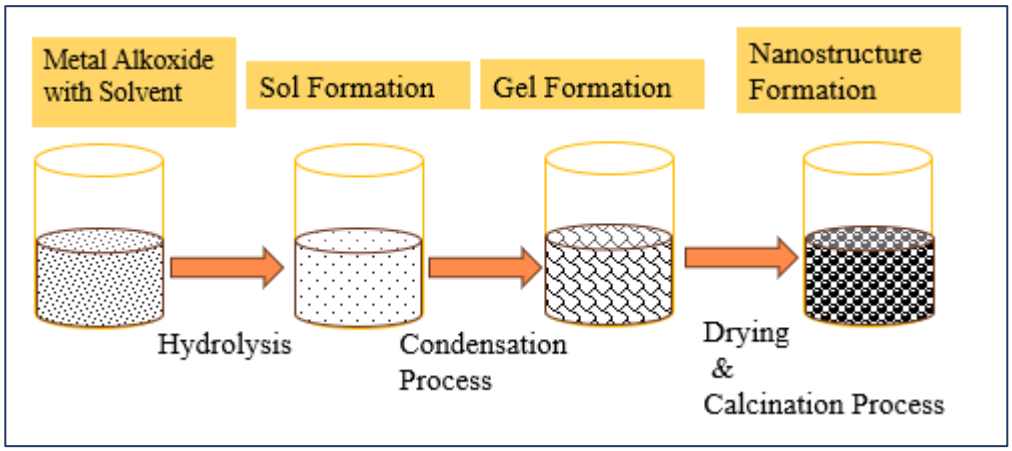

Figure 2.5. Sol-gel synthesis of Fe_2O_3 nanostructure

For example, according to Rasheed *et al* (2018), hematite nanomaterial was synthesized by the sol-gel method as follows. Typically, an experiment using α-Fe_2O_3 nanomaterial was conducted in a 500 ml beaker. 10 g of ferric nitrate was dissolved in 100 ml of deionised water. The solution was stirred for 15 minutes with a magnetic stirrer at ambient temperature to achieve complete salt dissolution and clarity. To prepare the solution, dissolve $NaHCO_3$ (sodium bicarbonate) 6.2376 g in 40 mL of deionized water in a baker (100 mL) and stir with a magnetic stirrer for 15 minutes at room temperature. Transfer the solution to a volumetric flask (50 ml) and fill to the mark. Begin by placing the first solution (ferric nitrate) on the magnetic stirrer and starting the engine. Then, add the second solution (sodium bicarbonate) to the burette. Add 2–3 drops of burette solution to the first solution at a time, stirring continuously. Brown precipitate forms with each addition to the base and can be used to verify the pH solution using litmus paper until the pH reaches 8, indicating complete interaction. The precipitate is removed from the solution and rinsed. Wash with distilled water many times until the solution is neutral. After washing the precipitate with ethanol 2-3 times, it was separated by centrifugation. Dried the precipitate, then used an electric furnace at a temperature of 100°C, and the precipitate was a brown-red powder(Rasheed *et al*., 2018)

2.4.3 Co-precipitation Method

The co-precipitation technique is the most popular method for producing iron oxide nanostructures due to its cost-effectiveness, environmental friendliness, and ease of

experimentation. production of Fe_2O_3 nanoparticles (Patil & Jagadale, 2023). The experimental procedure is as follows, according to Besnard *et al* (2020), to synthesize, stir to dissolve 10 g of $FeCl_3 \cdot 6H_2O$ in 150 mL of distilled water. At room temperature, a 2 mL NH_4OH solution was gradually added to the swirling mixture at a rate of 1 mL per minute. Throughout the synthesis, the pH was constant. After one hour of continuous stirring at ambient temperature, the black dispersion was heated to 80 °C and evaporated for two hours to yield a brown powder. After cooling to ambient temperature, the product was calcined at 500 °C for four hours. The as-prepared samples were calcined at temperatures ranging from 400 to 800 °C (Besenhard *et al*., 2020)

2.5. Reduced Graphene Oxide (rGO)

Graphene is a thin sheet structure of 2D with sp^2 carbon atoms arranged in an ordered form of a honeycomb. It possesses a great level of electrical conductivity (charge-carrier mobility of over 15,000 $cm^2\ V^{-1}\ s^{-1}$ at room temperature), mechanical strength, gas barrier properties, and a massive surface area. It is important to mention that rGO is structurally similar to graphene, except that it includes oxygen-containing functions that alter its electrical properties (Zhu *et al*., 2020). Combined with reduced graphene oxide (rGO), semiconducting oxides have emerged as an object of immense research interest lately and enhancing the charge separation and transportation. The rGO is characterized by a high electron mobility, conductivity, surface area, and cost-effectiveness(Mondal *et al*., 2021). The rGO stands out for its high electron mobility, conductivity, surface area, and cost-effectiveness(Mondal *et al*., 2021).

The reduced graphene oxide (RGO) is normally obtained through a modified Hummers process on graphite. During this process, graphite undergoes chemical oxidation followed by exfoliation to produce graphene oxide (GO). The oxidation stage usually cleaves the sp^2 hybridization and offers oxygen functionalities; thus, the gap between graphite layers and the delamination of the GO layers becomes easy. GO has functional groups with oxygen, including -COOH, -OH, -CHO, and epoxy groups. GO can be reduced to rGO that contains more defects than graphene because of the remaining oxygen-containing functions (Scheme 2.6); therefore, rGO and graphene cannot be considered the same. Various carbon forms can be obtained after reduction procedures, e.g. heat treatment and chemical treatments(Zhu *et al*., 2020).

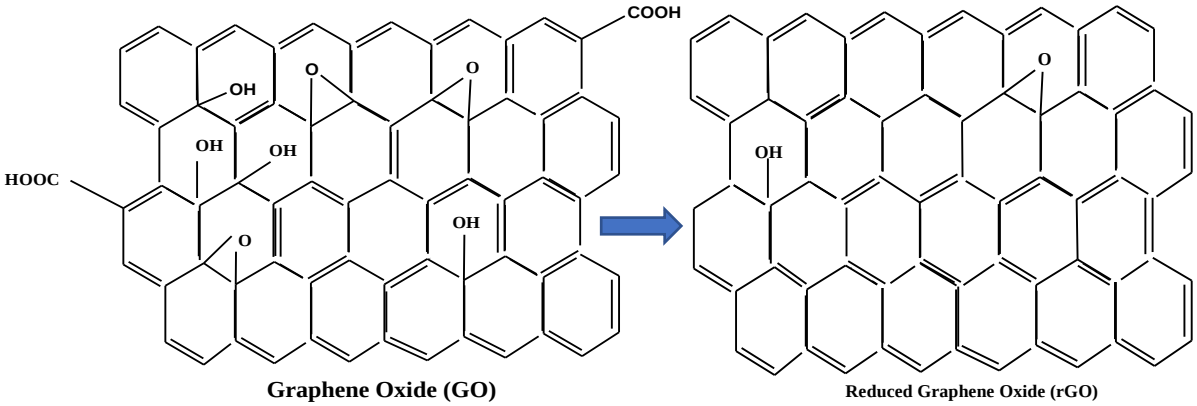

Figure 2.6. Scheme diagram of graphene oxidation and reduction

2.6 Overview of Herbicides

Pesticides are the chemicals to avoid, kill, repel or mitigate any pest such as insects, weeds, fungi, rodents or any other organism which may damage crops, animals or human health (Johri *et al.*, 2023). Pesticides can be categorized based on the type of pests they target and their chemical composition, the organism they kill, the route of entry, and the active ingredient of their chemical structure, categorized as fungicides, herbicides, bactericides, rodenticides, insecticides, nematicides, molluscicides, organophosphate pesticides, organochlorine pesticides, carbamates, urea, anilides, and pyrethroids (Ahamad *et al.*, 2023).

Among these, herbicides are the most common type, representing approximately 47.5-53% of total pesticide use (Beckie *et al.*, 2021). Herbicides are widely used in agriculture to control unwanted plants, typically weeds, and improve crop yields. Herbicides themselves functionally, they are also classified can be classified as selective, which target specific weed species while leaving crops unharmed, and non-selective, which kill most types of plant life (Gwatidzo *et al.*, 2023). Herbicides are also categorized based on their chemical nature and mechanism of action, with common groups including the phenoxyacetic acids (e.g., 2,4-D), triazines (atrazine), and organic phosphorus compounds like phosphonomethylamino acids (glyphosate) (Székács, 2021). Among these, the most widely utilized herbicides are 2,4-dichlorophenoxyacetic acid (2,4-D), used to control broad-leaf weeds in numerous crops (Ganzagh *et al.*, 2025). Its popularity is evident, with over 1,500 commercial herbicide products containing 2,4-D as an active ingredient (Martins *et al.*, 2024). 2,4-D is a synthetic auxin herbicide with the molecular formula $C_8H_6Cl_2O_3$ and a molecular weight of 221.0 g/mol (Magnoli *et al.*, 2020). It appears as

a white crystalline solid in some formulations, with moderate water solubility (850-900 mg/L at 25°C), a pKa of about 2.64 -2.8, and low vapor pressure (1.4*10-7), which reduces volatility. The half-life of 2,4-D varies between 7 and more than 300 days depending on the conditions under which it is used (Martins *et al.*, 2024). These 2,4-D herbicides may pollute the soil, water, and air with adverse consequences on biodiversity, such as the insects, birds, and aquatic organisms. In human beings, acute poisoning and prolonged health problems have been observed to be the effects of these chemicals, including cancer, reproductive injury, and endocrine disturbance (Ahamad *et al.*, 2023). Also, the herbicide can be accumulated in the food chain not only to those who are directly exposed but future generations. The fact that these chemicals have remained in the environment highlights the critical need to use safer and more sustainable approaches towards their management (Kaur *et al*., 2025)

2.6.1 Herbicide Degradation Methods

Several different removal techniques have been invented to deal with 2, 4-D contamination, and they are broadly grouped into physical, biological and chemical methods (Girón-Navarro *et al*., 2021).

2.6.1.1 Physical methods

Physical remediation techniques concentrate on the separation of contaminants, during which no chemical change/chemical transformation of the contaminants takes place. The use of physical methods such as adsorption has been common in the remediation of 2,4-D (Mathew *et al*., 2025). One of the best researched methods of eliminating 2,4-D in water is adsorption. It consists of attaching 2,4-D molecules (adsorbate) to the surface of a solid substance (adsorbent), e.g. agricultural waste (coffee waste, corncob, groundnut shell ash), commercially activated carbon, synthetic materials (inorganic-organic bentonites, silica gel, and metal-organic frameworks (MOF)(Trivedi *et al*., 2019). For example, studies have shown that granular activated carbon application led to an experimental adsorption capacity of 487 mg/g from the original concentration of 600 mg/L of 2,4-D (Coelho *et al*., 2020). In another example involving an agricultural-based adsorbent, date stone-derived activated carbon demonstrated an experimental adsorption capacity of 218.33 mg/g under an initial concentration of 400 mg/L(Hameed *et al*., 2009).

The limitation of this process is, it could be time-consuming compared to catalytic processes, it generates a secondary solid waste that still must be disposed of, and the most effective adsorbents (commercial activated carbon) may have high costs(Mathew *et al*., 2025). The process of adsorption can be slow, with the time required to reach equilibrium. It also generates solid waste in the form of the used adsorbent, which must then be regenerated or safely disposed of. Furthermore, better adsorption capacity commercial activated carbons can be expensive for large-scale use(Trivedi *et al*., 2019).

2.6.1.2 Biological remediation

Biological treatments utilize living organisms, more precisely microorganisms, to break down contaminants. The primary biological treatment is biodegradation, a green and natural process whereby bacterial strains or microbial consortia metabolize 2,4-D, degrading it into harmless compounds such as carbon dioxide and water (Chen *et al*., 2024). Special bacterial strains and sophisticated biological systems are used for this purpose. Examples of microorganisms used include Pseudomonas putida, Achromobactin sp., and Azotobacter sp., which are conducted in systems such as sequencing batch reactors (SBRs) or through bioaugmentation schemes (Muter, 2023). One such study with the Pseudomonas putida M1443 bacterial strain demonstrated a 100% death of a 160 ppm 2,4-D solution in 62 hours(Köksoy & Uraz, 2023). A different example with a microbial consortium of soil gave a 100 per cent removal in 3 days of a 400 ppm 2,4-D solution(Vanitha *et al*., 2023). The main drawbacks of biodegradation include its extremely slow rate of reaction with other processes and its high susceptibility to environmental factors like temperature, which necessitates sensitive and expensive control of the process and makes it difficult to scale up scale(Liu *et al*., 2025).

2.6.1.3 Chemical methods

The use of chemical treatment is common in the remediation of pesticides in water and soil because of its ability to destroy or convert the toxic substances (Kaur *et al*., 2021). These processes are encompassed by different chemical reactions whereby the molecules of pesticides are converted into less harmful compounds or they are eliminated in the environment(Kaur *et al*., 2021). Often, chemical methods such as ozone, where ozone gas is added to water to oxidize and break down pesticides (Joseph *et al*., 2021), and coagulation, where pesticides are combined with coagulants that are added to water to form larger particles and be easily eliminated (Koul

et al., 2022). Advanced oxidation processes (AOPs) combine oxidants like hydrogen peroxide with catalysts or UV light to produce highly reactive species that degrade pesticides(Sandoval *et al*., 2022). For examples of popular mechanisms of chemical remediation. Advanced oxidation processes (AOPs) involve the use of oxidants such as hydrogen peroxide combined with catalysts or UV light to generate overly reactive species that destroy pesticides (Sandoval *et al*., 2022). The Photo-Fenton process is an improvement of the Fenton reaction and generates more hydroxyl radicals to degrade, whereas the Photo-Fenton process operates using the light-activated catalysts, here TiO_2, to degrade pesticides(Akash *et al*., 2022). An example of a chemical degradation process is the Fenton process. In this enhanced oxidation reaction, hydrogen peroxide (H_2O_2) and iron salts (Fe^{2+} / Fe^{3+}) are used to produce hydroxyl radicals (OH). These radicals are highly reactive and can effectively degrade pesticides such as 2,4-D (Forti *et al*., 2020). The treatment of pesticide-contaminated environments using chemicals has its weaknesses, including the fact that most AOPs cannot remove 100 per cent of pesticides. Also, the techniques may produce adverse intermediates. The presence of degradation products or metabolites is complicated by their low concentrations as well as the fact that they are easily interfered with by the environmental matrices(Ahmad *et al*., 2024).

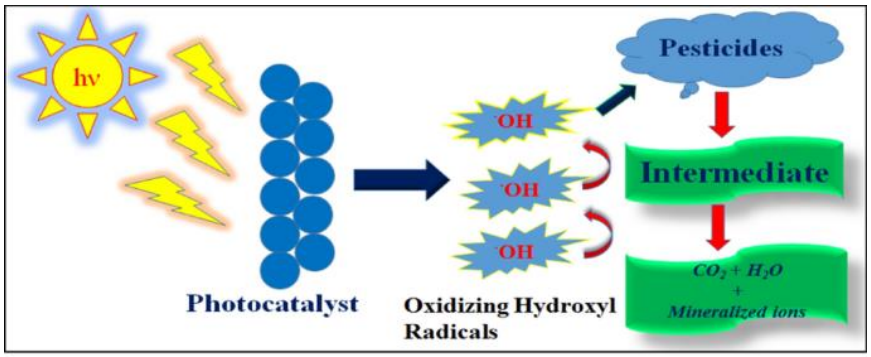

Figure 2.7. Schematic diagram for the general representation of the degradation of pesticides by photocatalysis (Shamim *et al*., 2024)

2.7 Hydrogen Production Methods

There are many ways of producing hydrogen, and each of them has its pros and cons. The most common method, steam methane reforming (SMR), involves the conversion of methane with steam to generate hydrogen, but it is also known to produce a lot of CO_2, which leads to climate

change. Similarly, coal gasification generates hydrogen but is highly carbon-intensive. On the renewable side, a cleaner option is water electrolysis driven by solar, producing hydrogen and oxygen from water without emitting any emissions. Solar energy, being the most abundant and renewable energy source, holds the most promise for sustainable H_2 production due to its abundance and energy production potential(Z. Wang *et al*., 2019; Z. Zou *et al*., 2001). Over the past five decades, significant progress has been made in the development of various solar-driven H_2 production technologies, and remarkable headway has been achieved in promoting the application and implementation of solar H_2 generation by resolving concerns with system prices, durability, and performance (Chen *et al*., 2020; Sharma & Arya, 2017; Q. Wang & Domen, 2020).

As illustrated in Figure 2.8, the current techniques for producing H_2 from solar energy can be broadly divided into the following categories: photothermal catalytic (PTC) H_2 production from fossil fuels (mainly CH_4), photocatalytic (PC) water splitting, photoelectrochemical (PEC) water splitting, photovoltaic-electrochemical (PV-EC) water splitting, solar thermochemical (STC) water splitting, and photobiological (PB) H_2 production.)(Chen *et al*., 2020; J. H. Kim *et al*., 2019; Pregger *et al*., 2009; Q, Wang & Domen, 2020). Photocatalytic (PC) water splitting, where sunlight excites catalysts to split water, though its efficiency is still low. Photoelectrochemical (PEC) water splitting stands out for its higher efficiency and direct use of solar energy, where semiconductors absorb sunlight to drive water-splitting reactions. PEC can be regarded as one of the most promising techniques because it can be scaled up and it can integrate with the already existing solar methods. The solar thermochemical (STC) water splitting involves the use of concentrated solar heat to split water, but it requires high temperatures, which is a technological challenge. Photothermal catalytic (PTC) hydrogen generation is a type of reaction that uses heat and light to catalyze the hydrogen generation of methane to reduce emissions, but not to stop the dependence on fossil fuels. Finally, photobiological (PB) hydrogen is produced by using microorganisms such as algae to generate hydrogen by use of sunlight, but this process is yet to be developed. There are many ways of producing hydrogen, and each of them has its pros and cons. The most common method, steam methane reforming (SMR), involves the conversion of methane with steam to generate hydrogen, but it is also known to produce a lot of CO_2, which leads to climate change. PEC can be regarded as one of the most promising techniques because

it can be scaled up and it can integrate with the already existing solar methods. The solar thermochemical (STC) water splitting involves the use of concentrated solar heat to split water, but it requires high temperatures, which is a technological challenge. Photothermal catalytic (PTC) hydrogen generation is a type of reaction that uses heat and light to catalyze the hydrogen generation of methane to reduce emissions, but not to stop the dependence on fossil fuels. Finally, photobiological (PB) hydrogen is produced by using microorganisms such as algae to generate hydrogen by use of sunlight, but this process is yet to be developed.

Photoelectrochemical (PEC) water splitting has been deemed as one of these approaches, as it is typically more efficient and can be scaled more easily. It is a direct, sustainable technology since semiconductor materials are used to convert solar energy to hydrogen; therefore, it is more viable in large-scale clean hydrogen production

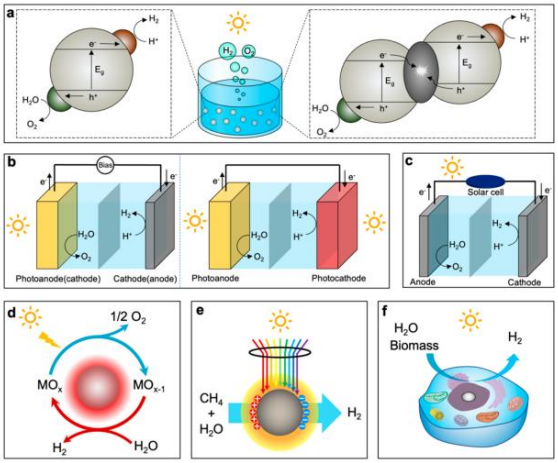

Figure 2.8. Different methods for producing H_2 using solar energy: (a) splitting water through photocatalysis (PC), (b) splitting water through photo electrochemistry (PEC),(c) splitting water through photovoltaic-electrochemistry (PV-EC), (d) splitting w d) splitting water through solar thermochemistry (STC), (e) producing H_2 through photothermal catalysis (PTC), and (f) producing H_2 through photobiology (PB)(Song *et al.*, 2022)**.**

2.8 Photoelectrochemical (PEC) water splitting

Hydrogen has also received much interest because of its carbon-free nature and high density of energy storage, enabling the use of photoelectrochemical techniques to split water into hydrogen and electricity in the process known as PEC water splitting (Rajeshwar, 2011; Staffell *et al.*, 2019). Since the earliest attempts to use TiO_2 as a photoanode, and Pt as a counter electrode to

split water into H_2 and O_2, the PEC cell has been engineered, in which half-cell reactions triggered the oxidation and reduction processes (Honda, 1910; Su & Vayssieres, 2016), thus splitting water in half, without the help of an external bias(Kumar *et al*., 2022). The entire principle behind the working of Photoelectrochemical (PEC) is as follows: The general notion is that light energy is consumed in the catalytic reaction to form the activation energy

2.8.1 Working Principle of Photoelectrochemical (PEC)

The process of splitting water into oxygen and hydrogen with the assistance of sunlight and bias, called PEC water splitting (Figure 2.9), is used to separate water (Rajitha *et al*., 2022), as illustrated in Figure 2.8. An appropriate supporting electrolyte, a counter electrode (often Pt), and a photoactive semiconductor serving as the working electrode are all components of a conventional PEC cell (Chiu *et al*., 2019). The basic PEC process consists of three steps(Fu *et al*., 2024; Kumar *et al*., 2022): (i) light absorption (the production of electrons and holes in the photoanode when irradiated by photons whose energy exceeds its bandgap), (ii) separation and transmission of electrons and holes produced by photosynthesis in the semiconductor to the electrode surface, (iii) participation of holes on the electrode surface in the half-reaction of oxidation of water and electron involvement in the half-reaction of water reduction. The process of electron-hole pairs recombining presents a considerable problem in water splitting with PEC. The semiconductor's valence band (VB) and conduction band (CB) must be properly positioned for water molecule reduction or oxidation. For the HER reaction, The CB of the semiconductor must be less than the reduction potential of H^+ (ECB < E0 red), while the VB must be higher than the water oxidation potential (EVB > E^0ox). Photoelectrochemical (PEC) reactions driven by solar energy require the possible potential window for splitting water into H_2 and O_2 is 1.23 V. The process of splitting water includes the oxidation of water using the oxygen evolution reaction (OER) uses four electrons, and the proton reduction process uses two electrons. in the hydrogen evolution reaction (HER). The following equations can be used to illustrate these half-cell reactions (Kumar *et al*., 2022):

$$Anode: 2H_2O(l) \rightarrow O_2(g) + 4H^+ + 4e^-$$

$$Cathode: 4H^+ + 4e^- \rightarrow 2H_2(g)$$

$$Over\ all\ 2H_2O(l) \rightarrow O_2(g) + H_2(g)$$

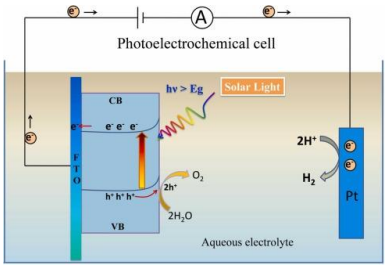

Figure 2.9. Photoelectrochemical (PEC) cell water splitting mechanism(Rajaitha *et al*., 2022)

2.9 Research Gap

Fe_2O_3 is a popular nanomaterial in photoelectrochemical (PEC) water splitting and photocatalytic degradation of organic pollutants, because of the superior light absorption in the visible spectrum, availability, non-toxicity, and low band gap (Sharma *et al*., 2019). But its performance efficiency remains limited due to challenges such as rapid charge carrier recombination, low electrical conductivity, and a short hole diffusion length (Johnston & Herz, 2016). Different methods are explored to overcome this limitation, including elemental doping, plasmonic modification, composite formation, and heterostructure (Vinoth *et al*., 2016). However, these methods have not fully resolved the fundamental issues affecting efficiency.

Most studies investigating localized surface plasmon resonance (LSPR), plasmonic metal-semiconductor photocatalysts offer a viable approach to improve light harvesting and encourage hot electron transport, successfully solving (Gao *et al*., 2012). Plasmonic metal-semiconductor photocatalyst enhancement has focused on noble metals, which are effective for both photocatalytic and PEC applications(Zada *et al*., 2020). But their rarity and expense limit their use for widespread (Wang *et al*., 2016). In contrast, non-noble metal plasmonics, such as aluminium (Al), possess the essential plasmonic properties and offer a promising alternative (Jiang *et al*., 2018), but remain underexplored in combination with Fe_2O_3. While Fe_2O_3/rGO composites are studied, promising enhancements in conductivity and surface properties are explored for PEC and photocatalytic applications (Uma *et al*., 2020). But the integration of aluminium-doped Fe_2O_3/rGO for hydrogen production via PEC water splitting and 2,4-D photocatalytic degradation remains unexplored. Addressing this gap, this study aims to develop stable and cost-effective photocatalysts based on Al-α-Fe_2O_3/rGO, advancing sustainable PEC and 2,4-D degradation

CHAPTER THREE

MATERIALS AND METHODS

3.1 Study Site Description

The synthesis of Al-α-Fe_2O_3/rGO was carried out at the Applied Chemistry Department, Postgraduate laboratory, Adama Science and Technology University (ASTU). Characterizations of the synthesized Al-α-Fe_2O_3/rGO nanostructure, including X-ray diffraction (XRD) and UV-Diffuse Reflectance Spectroscopy (UV-DRS) were conducted at ASTU's Department of Materials Science and Engineering. Photoluminescence (PL) analysis took place at the ASTU, Applied Physics laboratory, and Fourier Transform Infrared (FTIR) analysis took place at Addis Ababa Science and Technology University (AASTU). Energy Dispersive X-ray Scanning Electron Microscopy (SEM-EDX) and Field Emission Scanning Electron Microscopy (FESEM) characterizations were performed at Chungnam National University, South Korea. Photoelectrochemical water splitting experiments were conducted at the electroanalytical laboratory of the Department of Applied Chemistry, ASTU. Photocatalytic activity measurements were performed at the Department of Chemistry laboratory, Wallaga University.

3.2 Reagents and Chemicals

The solvents, reagents, and compounds utilized in this investigation were iron (III) nitrate nonahydrate ($Fe(NO_3)_3 \cdot 9H_2O$, 98%, Loba Chemie, India) as a source of Fe^{3+}, aluminum nitrate nonahydrate ($Al(NO_3)_3 \cdot 9H_2O$, 98%, Alpha Chemika, India) as a source of Al^{3+}, citric acid monohydrate ($C_6H_8O_7 \cdot H_2O$, 99.5%, Loba Chemie, India) as capping or stabilizing agent, ammonia solution (NH_4OH, 25%, AR, Sigma-Aldrich) for pH adjustment

Graphite flakes (99%, mesh size 100 mm), potassium permanganate ($KMnO_4$, 99.5%, AR, Alpha Chemika, India), hydrogen peroxide (H_2O_2, 30%, Fisher Scientific, India), L-Ascorbic acid (98%, Merck, Germany), concentrated sulfuric acid (H_2SO_4, 98 %, AR, India), and hydrochloric acid (HCl, 37%, Merck, Germany) were employed in the production of reduced graphene oxide (rGO) and analytical standard 2,4-Dichlorophenoxyacetic acid (99% Tianjin Chemical Reagent Co., Ltd. China) was obtained from Adami Tulu Pesticide Processing Factory. The test work used all the chemicals without further purification.

3.3 Instruments and equipment's

The crystallinity, average crystal size, and phase structure of the synthesized samples were examined using a powder X-ray diffractometer (model XRD-7000, Shimadzu, Japan) with Cu Kα radiation (λ = 1.5405 Å) as an X-ray source in the 2θ range of 10 to 80°. FTIR (IS50 ABX Thermo Scientific, USA) was used to confirm vibrational modes and bond formation between metal and oxygen between 400 and 4000 cm^{-1}. The chemical analysis, grain size, and surface morphological characterization of the samples that were synthesized were carried out using an energy-dispersive X-ray (SEM-EDX)-equipped scanning electron microscope (model SU7000, Hitachi, Japan). The optical response and energy band gaps of synthesized materials were examined using a spectrophotometer with diffuse reflectance (UV-DRS) (ElicoSL-150) in the 200-800 nm range. A Fluorescence Spectrometer (Agilent Cary Eclipse, USA) was used to measure photoluminescence (PL) in the 200-800 nm range. During the photocatalytic analysis, the optical characteristics were measured using a UV-Vis spectrophotometer (DU800R, DRAWELL). Electrochemical characterizations of the samples and application experiments were carried out using a potentiostat (model A-09048 Potentiostat, Eindhoven, Netherlands) equipped with a three-electrode conjugation system and electrochemical system software (IviumSoft).

3.4 Synthesis of Materials

3.4.1 Synthesis of the α-Fe_2O_3 and Al-α-Fe_2O_3 Nanostructures

Sol-gel synthesis was used to synthesis the α-Fe_2O_3 and Al-α-Fe_2O_3 nanostructures, following the procedure previously reported by (Alagiri & Hamid, 2015; Khan *et al*., 2015). A typical experiment involved dissolving 1.5 g (0.062 M) of iron (III) nitrate nonahydrate ($Fe(NO_3)_3 \cdot 9H_2O$) in 60 mL of deionized water. Next, 3 g (0.238 M) of citric acid monohydrate ($C_6H_8O_7 \cdot H_2O$) was added to the above solution and stirred for 2 hours. The pH of the mixed solution was adjusted to 10 by adding a 25% ammonia solution (NH_4OH). To get a homogeneous solution, the liquid was magnetically stirred, then slowly evaporated at 70 °C for 2 hours. Then the solution was dried at 100 °C, and a gel precursor was formed. To obtain the final products, α-Fe_2O_3 nanostructure, the gel was calcined in an electrical muffle furnace at 650°C for 3 hours

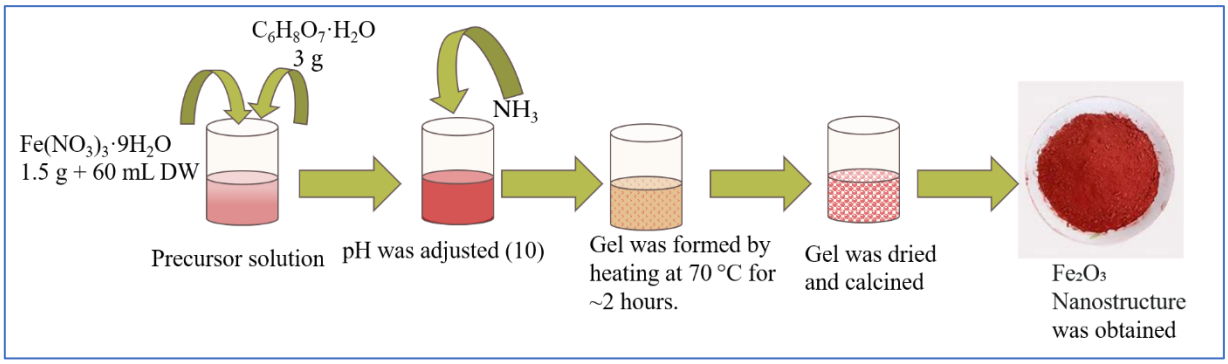

Figure 3. 1. Schematic illustration of the sol-gel synthesis process for α-Fe_2O_3 nanostructure

Al-doped α-Fe_2O_3 was synthesized using the same sol-gel technique. The procedure was identical to the synthesis of pure α-Fe_2O_3, but with the addition of $Al(NO_3)_3 \cdot 9H_2O$ salt as the aluminium precursor. This sol-gel technique was used to synthesize a series of nanostructures with varying molar percentage of the aluminum (Al) relative to iron (Fe), the following $Al(NO_3)_3 \cdot 9H_2O$ were added: 0.0139 g for 1% of Al doping, 0.0418 g for 3%, 0.0696 g for 5%, 0.0975 g for 7%, and 0.1253 g for 9% Al doping added. Then, 3 g (0.238 M) of citric acid monohydrate was added to the above solution and stirred for 2 hours. The pH of the mixed solution was adjusted to 10 by adding a 25% ammonia solution (NH_4OH). To get a homogeneous solution, the liquid was magnetically stirred, then slowly evaporated at 70 °C for 2 hours. Then the solution was dried at 100 °C, and a gel precursor was formed. To form the final products, Al-α-Fe_2O_3 nanostructure, the gel was calcined in an electrical muffle furnace at 650°C for 3 hours

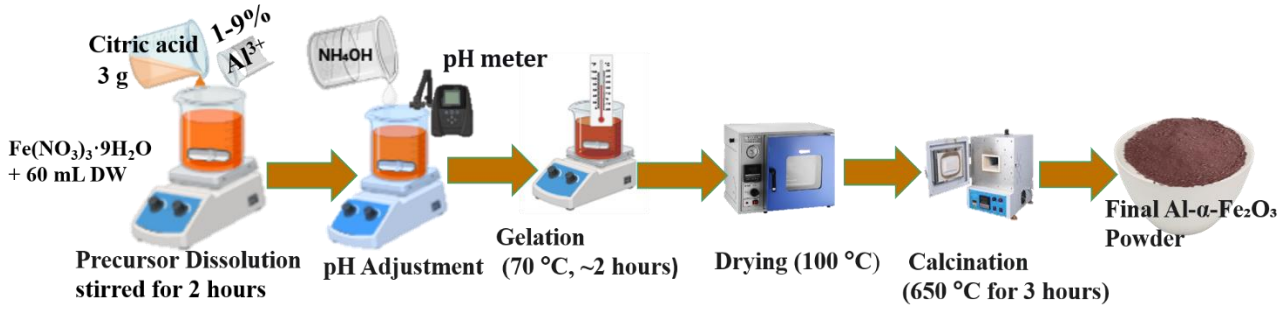

Figure 3.2. Schematic illustration of the sol-gel synthesis process for Al-α-Fe_2O_3 nanostructure

3.4.2 Graphene oxide (GO) and reduced graphene oxide (rGO) synthesis

The Reduction of rGO was conducted in three steps, namely intercalation (oxidation) and exfoliation, then reduction (Habte & Ayele, 2019). First, Graphene oxide (GO) was prepared through a modified Hummers process, which entails the oxidation of graphite, according to the steps that had been reported before (Tufa *et al*., 2018). In this step, graphite (0.3 g) and concentrated H_2SO_4 (40 mL) were mixed in a reaction vessel, with continuous stirring. Potassium permanganate ($KMnO_4$, 1.8 g) was then added gradually under continuous stirring while maintaining the temperature below 10°C under an ice bath. Then the reaction mixture was heated to 45 ^{0}C and stirred for 6 hours to complete oxidation. The distilled water was then added slowly by slowly and the temperature of the solution was not exceeded 250 °C. Then 40 mL of H_2O_2 was added, and the solution was stirred to terminate the oxidation. The mixture was then left to rest for another 24 hours without stirring. Lastly, the product was centrifugation and washed using ethanol,10% HCl solution and distilled water.

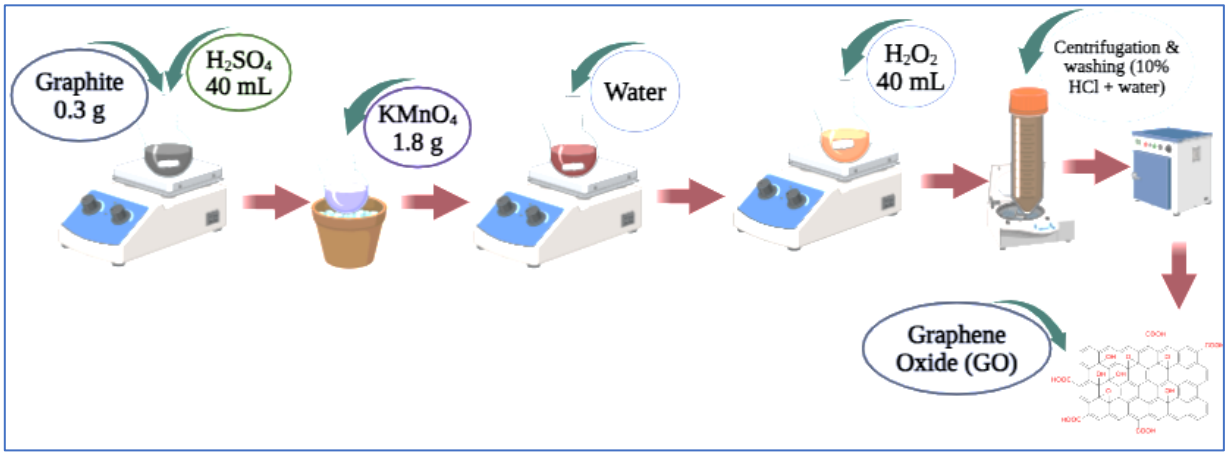

Figure 3.3. Schematic Illustration of Graphene Oxide (GO) Synthesis via Modified Hummers Method

Habte *et al*. (2019) described a method of the reduction of synthesized graphene oxide (GO) to reduced graphene oxide (rGO) with ascorbic acid. First, 40 mg of synthesized GO was dispersed in 400 mL of double-distilled water (0.1 mg/mL) and stirred using a magnetic stirrer in 20 minutes. The suspension was left to ultrasonically treat for 1 hour to exfoliate the layer of graphene oxide sheets. After exfoliation, 1.6 g of ascorbic acid concentration (AA) was added into the suspension and stirred-mixed of the mixture at 70 ^{0}C by using a hot plate and magnetic stirrer for 30 minutes. The color of the suspension transformed into black, which meant that rGO

had been produced. The black product was then left to stand, then filtered through Whatman filter paper, washed thrice with the use of ethanol and double-distilled water, and dried overnight at 120 ^{0}C in an oven(Habte & Ayele, 2019). The powder was crushed with a mortar and pestle and kept for future characterization and application research.

3.4.3 Al-α-Fe_2O_3/rGO Nanostructures Synthesis

A sol-gel synthesis method involving a sonication path was used to produce an Al-α-Fe_2O_3/rGO nanostructure by modifying a previous procedure of α-Fe_2O_3/rGO composites (Nag *et al*., 2016). It began by setting up the dispersion of 5mg graphite oxide (GO) in 50 mL of distilled water (0.1 mg/mL), followed by the 1-hour sonication (De Silva *et al*., 2018). In a separate step, an aqueous solution was prepared by dissolving 0.149 g of ferric nitrate nonahydrate ($Fe(NO_3)_3 \cdot 9H_2O$) and 0.00696 g of aluminium nitrate with homogeneous stirring with a magnetic stirrer. The amount of ferric nitrate nonahydrate, equivalent to a 17% weight percentage of GO to α-Fe_2O_3 (Nag *et al*., 2016) and aluminium nitrate provides approximately 5% molar Al doping relative to iron. Then the prepared metal precursor solution was dropped and added wisely to the GO dispersion with vigorous stirring at room temperature, while keeping a strictly alkaline pH 10 with ammonium hydroxide(to enhance the stability of colloids by electrostatic attraction(De Silva *et al*., 2018). To aid the reduction of GO to rGO, 50mg of ascorbic acid (AA)(for achieving a reduction of 10:1 mass ratio of AA to GO (De Silva *et al*., 2018)) was added, and the mixture was continuously stirred at 70°C for 2 hours. After cooling to room temperature, the resulting gel solution was centrifuged, extensively washed with water and ethanol to eliminate contaminants, and then dried in an oven at 50°C for 24 hours. Finally, the synthesized nanostructure was calcined to obtain Al-α-Fe_2O_3/rGO.

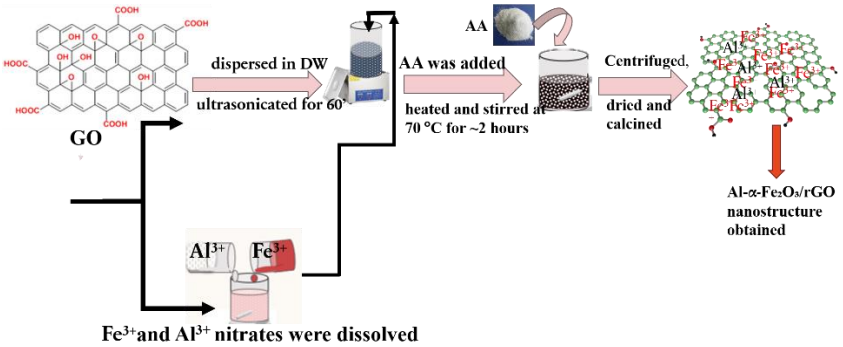

Figure 3.4. Schematic synthesis process for Al-α-Fe_2O_3/rGO nanostructure

3.5 Characterization Techniques

3.5.1 X-Ray diffraction (XRD)

An X-ray diffractometer (XRD-7000, SHIMADZU Corporation, Japan) was used to examine the synthesized sample's structural characteristics and crystallite size using Cu-Kα radiation (λ = 0.15404 nm, 40 kV, 40 mA) at a scan rate of 3 o/min in a 2θ range of 10 ° and 80 °. The Debye-Scherrer equation was used to determine the average crystallite size. (Basak *et al.*, 2022)

$$D=\frac{K\lambda}{\beta\cos(\theta)}=\frac{0.9\ x\ 0.15406}{FWHM\ cos(\theta)}\ldots\ldots\ldots\ldots\ldots\ldots\ldots\ldots\ldots..8$$

where λ (Lambda) is the wavelength of the X-ray source used, standard copper source (Cu Kα), β is the Full Width at Half Maximum (FWHM) of the most intense diffraction peak, θ (Theta) is the Bragg diffraction angle for the intense peak, and D is the average crystallite size (nm).

3.5.2 Field Emission Scanning Electron Microscopy (FESEM) and Energy Dispersive X-ray (EDX) Spectroscopy

state Using a field emission scanning electron microscope (FE-SEM, model SU7000, Hitachi, Japan) in conjunction with energy dispersive X-ray (EDX), the elemental composition, the surface morphology, particle size, and aggregation of the produced nanostructured materials were clarified (Patterson, 2022)

3.5.3 X-Ray Photoelectron Spectroscopic (XPS)

XPS studies were conducted to investigate the elemental composition and oxidation states of elements present on the surface of the nanomaterials

3.5.4 Fourier Transform Infrared Spectroscopy (FTIR)

Functional groups in synthesized nanomaterials were identified using a Fourier Transform Infrared spectrometer (IS50 ABX Thermo Scientific, USA). The spectra were then recorded between 400 and 4000 cm^{-1}

3.5.5 Surface Area analysis

The Brunauer–Emmett–Teller (BET) method is a technique that uses the physical adsorption of a gas on the surface of a solid, usually at the temperature of liquid nitrogen, to determine the specific surface area of a powder. Using adsorption measurements, this technique determines the surface area by quantifying the amount of gas adsorbed(Shimizu & Matubayasi, 2022).

3.5.6 UV-Visible Diffuse Reflectance Spectroscopy (UV-DRS)

The optical absorption properties and the band gap of the synthesized nanomaterials were determined using a UV-Vis diffuse reflectance spectrophotometer (Ray *et al*., 2022). The ultraviolet-visible diffuse reflectance spectroscopy method (Carry 100 UV-Vis, Agilent Technologies, USA). After the solid samples were put in a sample holder, the reflectance spectrum was captured, and the band gap energy of the nanomaterials was ascertained using the Kubelka-Munk function.

3.5.7 UV-Visible Spectroscopy (UV-vis)

The absorption of the synthesized materials was recorded using the UV-Vis spectroscopy (DU800R, DRAWELL).

3.5.8 Photoluminescence (PL)

To measure the photoluminescence, a photoluminescence spectrometer device (Cary Eclipse, S/N: MY18490002, Agilent Technologies) was operated to measure the emission spectrum of the synthesized nanomaterials under optical excitation. This data showed the changes in wavelength of emissions and suppression of the electron-hole recombination (EHR) (Albert Manoharan *et al*., 2018).

3.6 Electrochemical Studies

The potentiostat (model A-09048 Potentiostat) was used to carry out an electrochemical characterization of α-Fe_2O_3, Al-α-Fe_2O_3, and Al-α-Fe_2O_3/rGO nanostructure. Techniques applied, including electrochemical techniques, cyclic voltammetry (CV), electrochemical impedance spectroscopy (EIS), linear sweep voltammetry (LSV) and chronoamperometry (CA). A standard three-electrode system was employed, consisting of the prepared nanomaterial films as the working electrode, a platinum wire as the counter electrode, and Ag/AgCl (3M KCl) as the reference electrode. The electrolyte used for all measurements was a 1.0 M Sodium hydroxide (NaOH) solution (pH ≈ 13.6). All measured potentials were converted to the Reversible Hydrogen Electrode (RHE) scale using the Nernst equation:

$$E_{RHE} = E_{(Ag/AgCl)} + 0.059\,pH + E^{\circ}_{(Ag/AgCl)} \quad \ldots\ldots\ldots\ldots\ldots\ldots\ldots\ldots 8$$

3.6.1 Fabrication of the working electrode

The working electrode of synthesized nanostructure was fabricated as shown in Figure 3.5 below. First, a catalyst slurry was sonicated and drop-casted onto an FTO substrate, then dried. The deposited catalyst layer was calcined to form a uniform catalyst film for electrochemical measurements

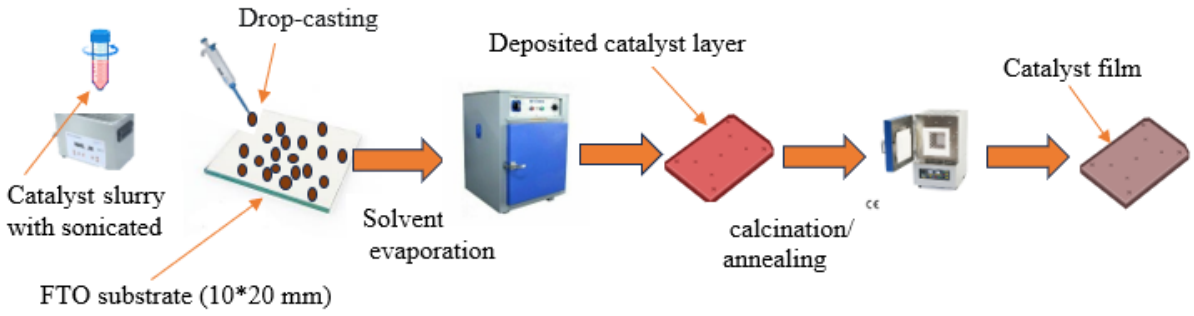

Figure 3.5. Fabrication of film of synthesized nanomaterials for the photoanode electrode

3.7 Photocatalytic Performance Test

The photocatalytic activity of the synthesized samples, α-Fe_2O_3, Al-α-Fe_2O_3 and Al-α-Fe_2O_3/rGO, was tested by degrading 2,4-D in aqueous solutions under visible light irradiation using a 150 W Tungsten halogen lamp in a photo reactor wavelength range was 200 to 800 nm. In these tests, the operating parameters were optimized by varying one factor at a time, and the conditions used for the degradation of 2,4-D are summarized in Table 1. For a typical photocatalytic experiment, 100 mL of a 2,4-D solution of the desired concentration was placed into an open glass reactor and stirred continuously. To establish adsorption-desorption equilibrium, the specified amount of photocatalyst was added to the solution, which was then magnetically stirred for 30 minutes in the dark.

Finally, the photocatalytic activity of the produced photocatalysts was measured using a UV-Vis absorption spectrophotometer, comparing the change in absorbance of 2,4-D with the corresponding λ_max (283 nm).

Barkatullah *et al* (2018) employed salt addition to determine the point of zero charge (pHPZC). Ten Erlenmeyer flasks were each filled with 50 mL of a 0.01 M NaCl solution. After adding 10 mg of the photocatalyst to each solution, the pH was adjusted to 2-12 with 0.1 M NaOH and 0.1 M HCl.

Table 1. Operating parameters in the degradation of 2,4-D

Optimization of pH	Optimization of Catalyst Dosage(mg)	Optimization of Initial Pollutant Concentration(mg/L)	Optimization of Reaction Time(min)
3	10	10	0
5	50	15	30
7	100	20	60
9	150	25	90
11	200	30	120

The percentage of degradation was calculated using the expression shown below.

The percentage of degradation = $\frac{Co-Ct}{Co}$ x 100……9

Where Co is the initial concentration of 2,4-D; Ct is the concentration of 2,4-D at the time interval.

The photocatalysts were tested for reusability during five activity cycles.

3.8 Reusability Test

The reusability tests were performed after the photocatalytic degradation of 2,4-D. After each cycle, the catalyst was recovered by centrifuging the reactant mixture at 5000 rpm for 15 minutes to separate it from the supernatant solution. The catalyst was then washed three times with deionized water and ethanol. The residue was dried and reused in subsequent experiments (Mishra *et al.*, 2025). The photocatalysis method was repeated five times with fresh 2,4-D

CHAPTER FOUR

RESULTS AND DISCUSSION

4.1 X-ray Diffraction (XRD) Analysis

Phase composition and crystalline structure of the synthesized materials were identified by X-ray diffraction (XRD) analysis, and the results are presented in Figure 4.1. Figure 4.1 (a) represents the XRD pattern of the pristine α-Fe_2O_3 nanostructures. All the diffraction peaks found at 2θ values of 24.1°, 33.3°, 35.8°, 40.6°, 49.5°, 54.1°,62.1°, and 64.20° can be identified uniquely with the (012), (104), (110), (113), (024), (116), and (300 crystal planes of rhombohedral hematite structure. The corresponding phase composition and space group R3C are in excellent agreement with standard JCPDS card No. 33-0664, which confirms the successful synthesis of phase-pure, α-Fe_2O_3 (Elbasuney *et al*., 2020).

The influence of aluminium doping on the hematite structure is displayed in Figure 4.1 (b). At higher concentrations of Al dopant (3%, 5%, 7%, and 9%), the hematite phase remains the only crystalline phase detected. No characteristic peaks related to aluminium oxide or other impurities appeared, indicating that the Al ions had been incorporated into the α-Fe_2O_3 crystal lattice successfully instead of creating a second phase. This effective incorporation is also evidenced by the enhanced observation of the (104) and (110) peaks in Figure 4.1 (c). Shift of the diffraction peaks to a greater 2θ angle as the concentration of Al doping is increased. According to Bragg's Law ($n\lambda = 2d\sin\theta$), the enhancement of the diffraction angle (θ) corresponds to a decrease in the interplanar distance (d). This lattice shrinkage is caused by the substitution of larger Fe^{3+} ions (ionic radius 0.645 Å) by Al^{3+} ions with a smaller radius (ionic radius 0.535 Å) in the hematite crystal lattice. These cause distortions and strain because of their smaller ionic radius of Al^{3+}. This shift of the peak is a good indication of successful substitutional doping (Irshad & Want, 2024).

Finally, Figure 4.1 (d) confirms the successful synthesis of the Al-α-Fe_2O_3/rGO composite. The GO pattern displays a characteristic, strong peak at 2θ ≈11.01° of the (001) plane with a high interlayer distance attributed to oxygen functional groups (C-OH, COOH, C=O) on the GO surface. Following reduction, this peak disappears and is replaced by a broad diffraction peak

at 2θ ≈ 24.5° for rGO, characteristic of the (002) plane, indicating the removal of most oxygen functional groups and the restacking of the graphene sheets. The obtained Al-α-Fe_2O_3/rGO composite pattern distinctly shows the presence of both components; sharp, well-defined peaks of the Al-doped hematite phase are dominant, with the broad (002) peak of rGO evident as well. This means that the Al-α-Fe_2O_3 nanostructures are successfully integrated into the rGO sheets (Elbasuney *et al.*, 2020).

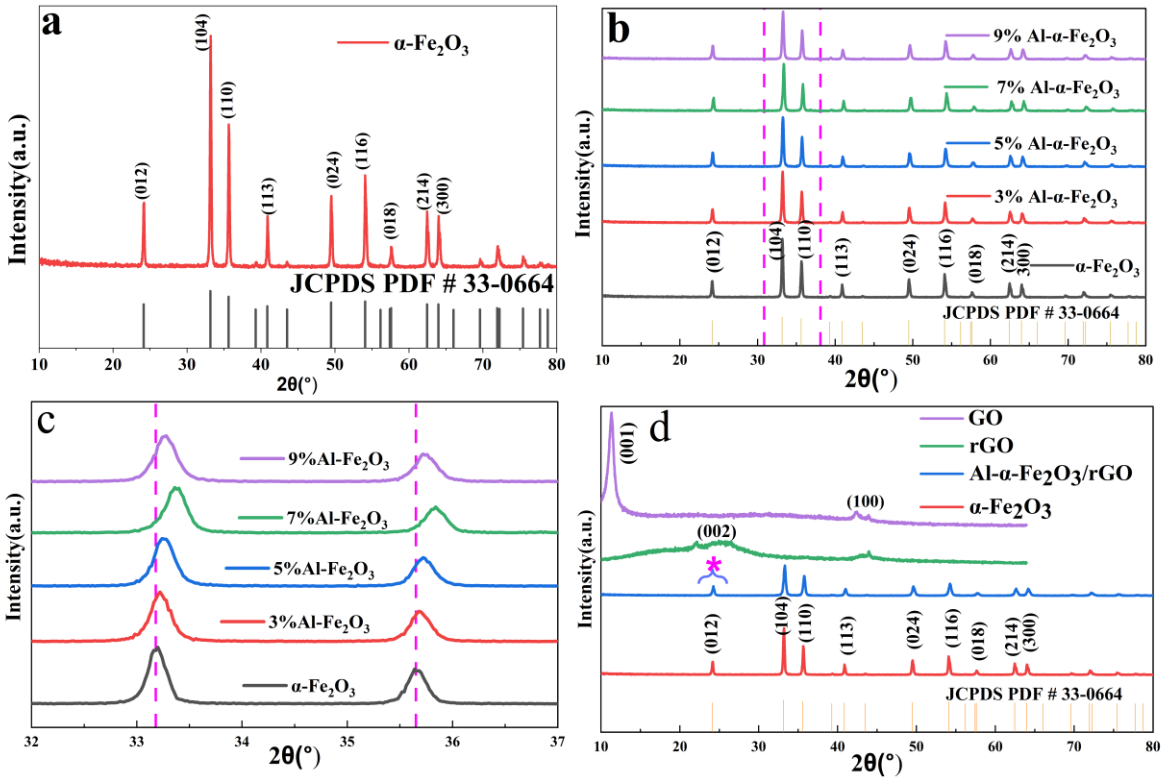

Figure 4.1. (a) XRD data of pure α-Fe_2O_3, (b&c) Al-α-Fe_2O_3 and (d) graphene oxide (GO), reduced graphene oxide (rGO), and the final Al-α-Fe_2O_3/rGO nanostructure

The Debye-Scherrer equation (D = $K\lambda/\beta cos\theta$ = (0.9 x 0.15406)/ (FWHM $cos\theta$) was used to determine the average crystalline size (Basak *et al.*, 2022). Where D stands for the crystal average particle size; k is the Sherrer constant, which is assumed to be 0.9 for this study; λ is an X-ray source wavelength at Cu Kα radiation (0.15406 nm); β represents diffraction peaks full width at half-maximum; and θ is Bragg's angle of diffraction. The results of this analysis are detailed in Table 4.2. The undoped α-Fe_2O_3 has the largest average crystallite size of 40.37 nm. As aluminium doping concentration increases, the crystallite size systematically decreased to

35.40 nm for 3% Al-α-Fe_2O_3, 33.24 nm for 5% Al-α-Fe_2O_3, 32.51 nm for 7% Al-α-Fe_2O_3, and 31.57 nm for the 9% Al-α-Fe_2O_3 nanostructures. The most significant reduction was observed for the Al-α-Fe_2O_3/rGO composite, which exhibited the smallest average crystallite size of 24.42 nm, that enhances the surface area and the quantity of active sites for photocatalysis. Although further doping of the crystallites (higher Al, i.e. 7% or 9%) can further decrease the size of the crystallites, excessive the doping may cause distortions of the structure, or increased defects, or change the electronic properties in a manner that can inhibit the separation of charges or enhance recombination and ultimately reduce photocatalytic efficiency (Irshad *et al.*, 2025; Liu *et al.*, 2023). This Decrement indicates the Al^{3+} ions inhibiting grain growth (Chibania *et al.*, 2022), and the rGO nanosheets acting as a barrier to particle agglomeration during synthesis*(M. Zhang et al.*, 2021)

Table 2. Average crystallite size of synthesized materials determined from XRD peak analysis

Sample name	2θ (Degree)	β (Radian)	D (nm)	Average Cry. size (nm)
α-Fe_2O_3	33.2059 35.6732 54.1180	0.00318 0.00323 0.00321	41.78403 40.86361 38.46627	40.37
3%Al- α-Fe_2O_3	33.2392 35.7053 54.1609	0.003634 0.003551 0.003798	36.56073 37.1663 32.50477	35.40
5%Al- α-Fe_2O_3	33.2740 35.7352 54.2137	0.003716 0.003670 0.004404	35.75071 35.95816 28.02543	33.24
7%Al- α-Fe_2O_3	33.3856 35.8465 54.3508	0.003827 0.0038758 0.0042831	34.70367 34.03815 28.79885	32.5
Al- α-Fe_2O_3/rGO	33.3070 35.7747 54.2409	0.005198 0.005117 0.005627	25.55564 25.78694 21.93158	24.42

4.2 Analysis of Morphology

Figure 4.2 shows SEM images and particle size distribution analysis of α-Fe_2O_3 and Al-α-Fe_2O_3/rGO nanostructures. Figure (4.2a) shows the α-Fe_2O_3 nanostructure and the irregularly shaped agglomerates with harsh surfaces occur at the micrometer size, which is a typical morphology of the hematite nanoparticles synthesized by sol-gel. Figures (4.2b) and (4.2c) represent the Al-α-Fe_2O_3/rGO nanostructures with the Al-doped nanostructures at high magnifications, with small particles that are well dispersed on the rGO sheets and uniformly distributed. It is observable that the layered structure of the rGO can act as a conductive support structure, as shown in Figure 4.2b, which is advantageous in photocatalytic uses of the material. Figure (d) shows the mean size distribution of the particle sizes of the Al-α-Fe_2O_3/rGO nanostructures, with the particle sizes ranging between 50 and 100 nm with an average size of 78 nm. This size distribution is relatively small and less than that of the pure α-Fe_2O_3, and the size of the particle is smaller, which is favorable to increase the surface area and activity of the catalyst(Wu *et al*., 2022).

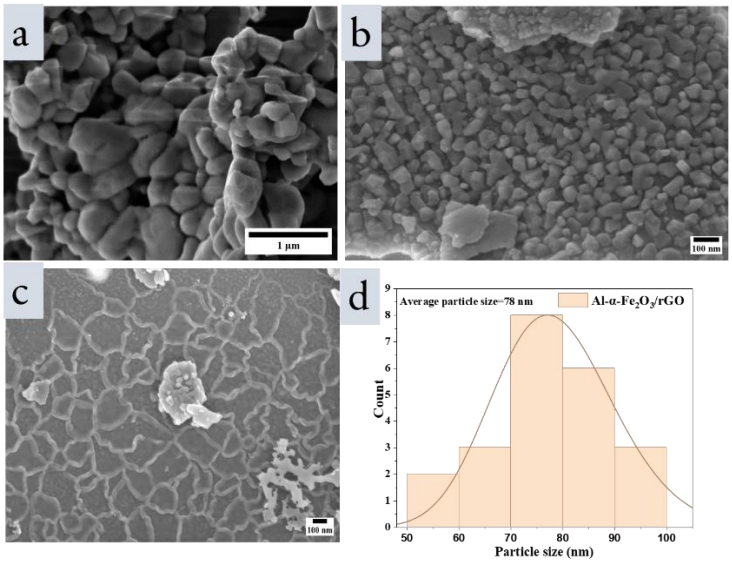

Figure 4. 2. Sem image of (a) α-Fe_2O_3 nanostructure, (b&c) Al-α-Fe_2O_3/rGO nanostructures, and (d) average particle size distribution of Al-α Fe_2O_3/rGO nanostructure.

The morphology of synthesized, α-Fe_2O_3, Al-α-Fe_2O_3 and Al-α-Fe_2O_3/rGO nanostructures were examined using field emission scanning electron microscopy (FE-SEM) as shown in Figure 4.3. The bare α-Fe_2O_3 nanostructure (Figure 4.3 (a, a1) displays an aggregated morphology with irregularly shaped nanoparticles forming clusters with a relatively rough surface. In contrast,

Al-α-Fe_2O_3 (Figures b and b1) illustrates a denser and more compact morphology with slightly smaller particle agglomerates, indicating the effect of aluminium incorporation on the microstructure (Favela-Camacho *et al*., 2019). The introduction of Al^{3+} into the hematite lattice is responsible for lattice contraction and peak broadening in XRD patterns, which are consistent with the strain induced and the inhibition of crystallite growth, leading to the smaller grain sizes visually evident in (Figure 4.1, Table 4.1). For Al-doped α-Fe_2O_3/rGO nanostructure (Figures c and c1) where the characteristic nanostructured α-Fe_2O_3 particles are intimately anchored on reduced graphene oxide sheets, exhibiting a porous, layered architecture that promotes better charge transfer and surface area. Al-doped α-Fe_2O_3/rGO and graphene generate Fe-O-C bonds, which are responsible for developing this little cluster (Kaidar *et al*., 2024).

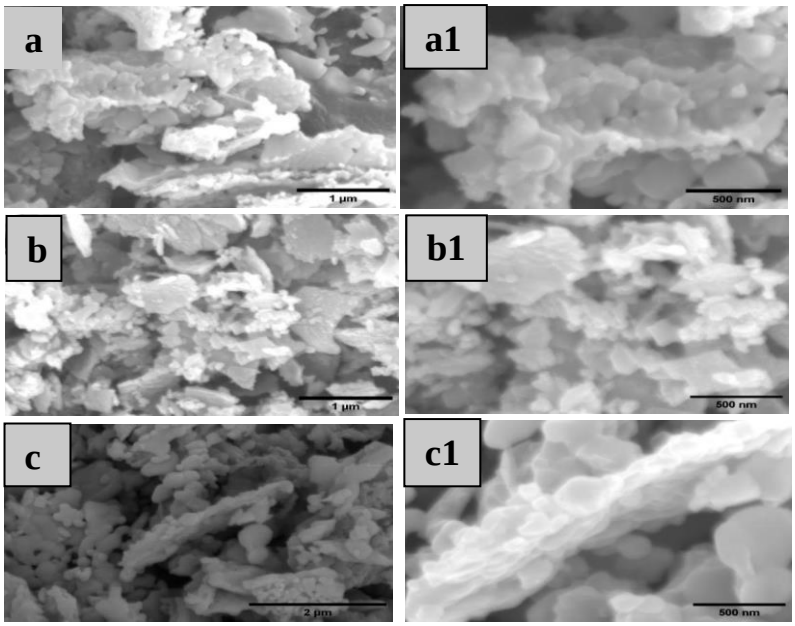

Figure 4.3. FESEM images of (a, a1) α-Fe_2O_3, (b, b1) Al-α-Fe_2O_3, and (c, c1) Al-α-Fe_2O_3/rGO nanostructures

These Al-α-Fe_2O_3 nanostructures are dispersed and decorated onto these rGO sheets, which appear well anchored to the rGO matrix, signifying good dispersion and strong interfacial interaction. The rGO may be playing the role, preventing large-scale agglomeration of metal oxide by providing a platform for separation.

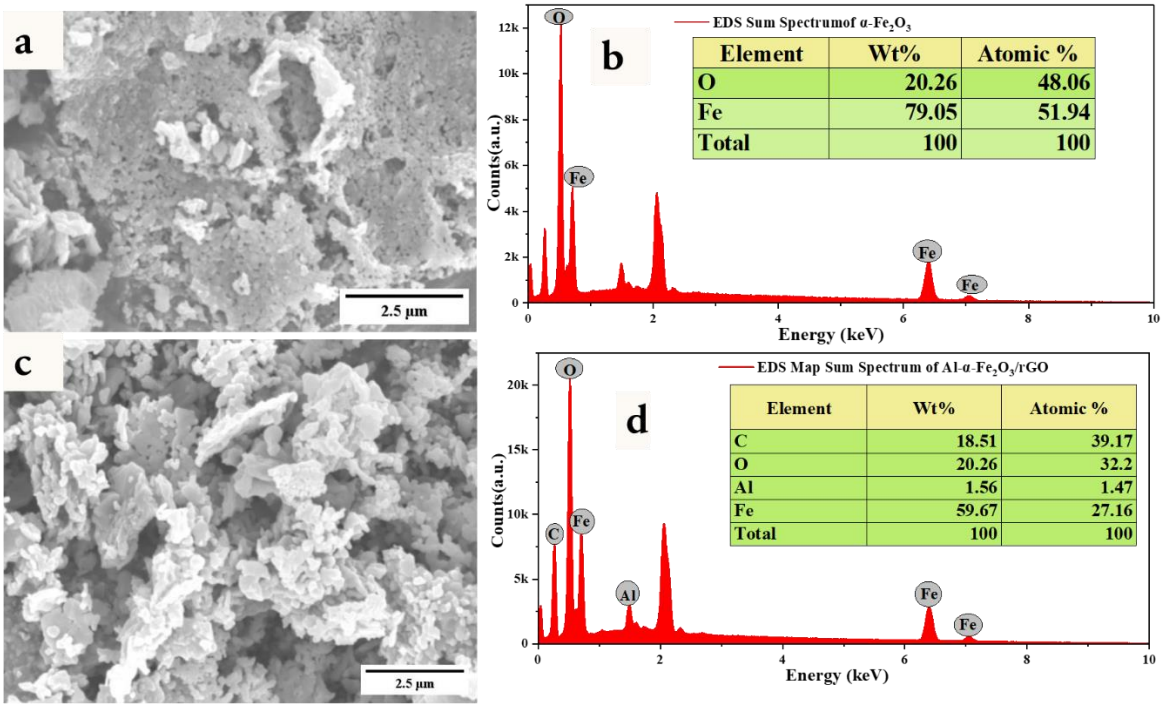

Figure 4.4. SEM-EDX spectra of (a, b) α-Fe_2O_3, and (c, d) Al-α-Fe_2O_3/rGO nanostructure

Figure 4.4 (a-d) shows the SEM-EDX spectra of α-Fe_2O_3, (a, b) and (c, d) Al-α-Fe_2O_3/rGO. The SEM image of pure α-Fe_2O_3 (Figure 4.4a) indicates a morphology characterized by irregular, aggregated particles. The EDX spectrum for α-Fe_2O_3 (Figure 4.4b) clearly shows prominent peaks for Oxygen (O) and Iron (Fe), confirming the elemental composition of the sample. The inset table quantifies these elements, indicating an Oxygen content of 20.26 wt% (48.06 atomic%) and an Iron content of 79.05 wt% (51.94 atomic%). These percentages are consistent with the expected composition of α-Fe_2O_3. For Al-α-Fe_2O_3/rGO, the graphic (Figure 4.3c) clearly shows the SEM image of the nanostructure shows a distinct change in morphology compared to pure α-Fe_2O_3. While aggregation is still present, the overall structure appears to incorporate sheet-like features, which are characteristic of reduced graphene oxide (rGO), showing successful integration of Al^{3+} ions into α-Fe_2O_3, resulting in the desired nanostructure. The EDX spectrum for the Al-α-Fe_2O_3/rGO nanostructure (Figure 4.4d), the inset table quantifies these elements, confirms the presence of four main elements of the components listed, C, O, Al, and Fe. The presence of a significant carbon peak (18.51 wt%, 39.17 atomic%) confirms the incorporation of rGO into the composite. Aluminium (Al) is also detected at 1.56

wt% (1.47 atomic%), verifying the successful doping of α-Fe_2O_3 with Al. Oxygen and Iron are present at 20.26 wt% (32.2 atomic%) and 59.67 wt% (27.16 atomic%), respectively, reflecting the α-Fe_2O_3 component within the composite. The elemental analysis thus provides strong evidence for the successful synthesis of the Al-α-Fe_2O_3/rGO nanostructure.

The mapping patterns (Figure 4.5a) show a homogeneous distribution of O, Fe for α-Fe_2O_3, and Fe, Al, C and O elements in the Al-α-Fe_2O_3/rGO nanostructure (Figure 4.5c) confirms the presence of Al and C in Al-α-Fe_2O_3/rGO nanostructure, together with Fe as well as O elements.

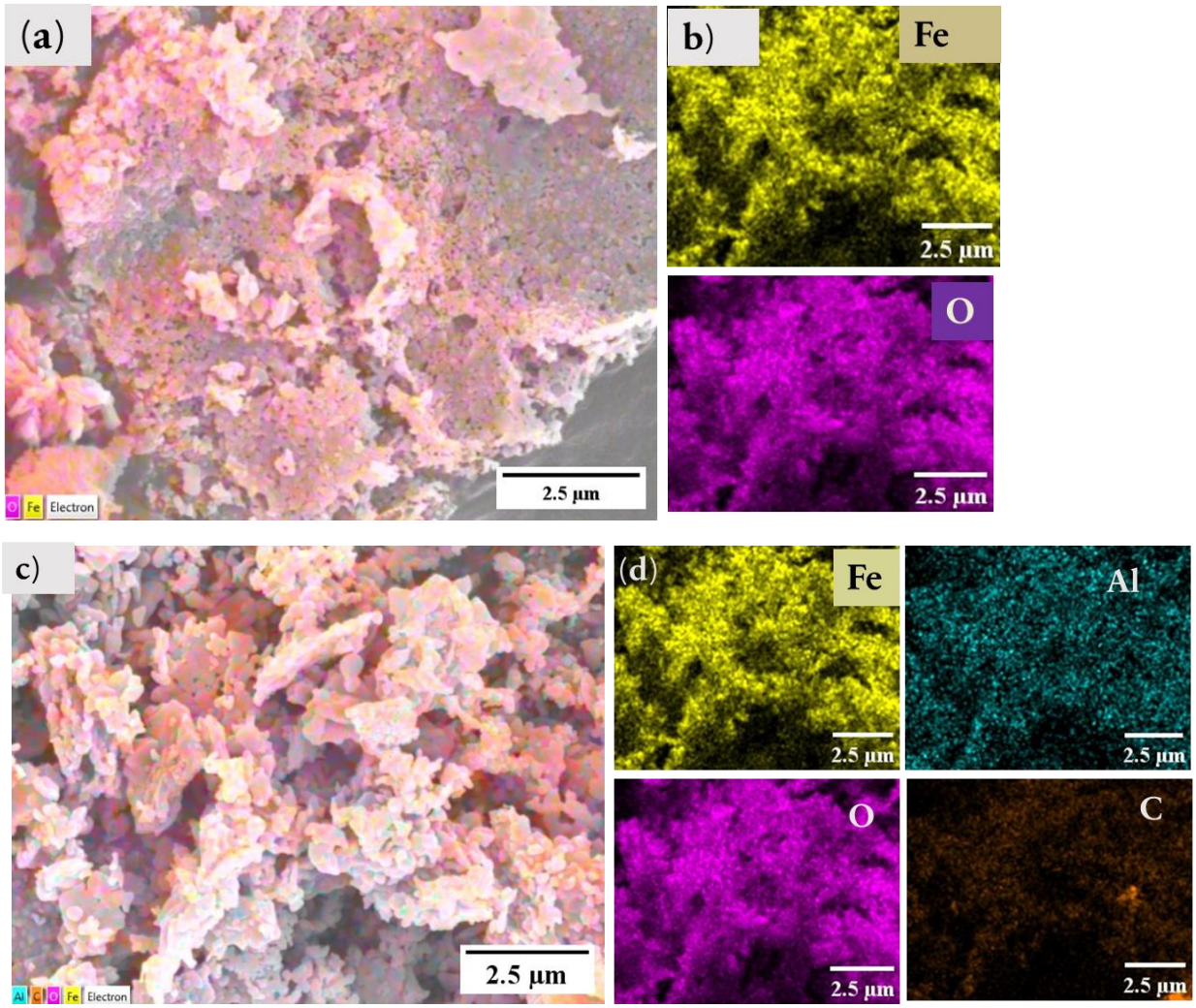

Figure 4.5. SEM-EDX elemental mapping of (a) α-Fe_2O_3, and (b) Al-α-Fe_2O_3/rGO nanostructures

4.3 X-Ray Photoelectron Spectroscopic (XPS)

XPS spectroscopy was used to investigate the surface composition and associated valence states of the elements present on the Al- α-Fe_2O_3/rGO nanostructure, as shown in Figure 4.6. The XPS survey spectrum in Figure 4.6a shows that the elements Fe, O, C, and Al, consistent with the expected elemental composition (Verma *et al*., 2022). The high-resolution of the Fe 2p spectrum (Figure 4.6b) shows the two peaks the which show the binding energy (BE) values for the Fe 2p1/2 and Fe 2p3/2 at 723 eV and 710.15 eV, respectively and indicative of Fe^{3+} ions in α-Fe_2O_3 (Verma *et al*., 2022). The O 1s spectrum (Figure 4.5c) shows a major peak at binding energies of 529.23 eV attributed to oxygen anions (O-Fe-O) and a lesser peak at 531.014 eV corresponding to surface hydroxyl (-OH), consistent with reports (Upendranath *et al*., 2024). The broad C 1s signal (Figure 4.6d) is deconvoluted into three peaks at 284.35, 285.7, and 286 eV, which are attributed to graphitic C-C/C=C, C=O, and C-H, confirming functional groups, in the rGO (Zong *et al*., 2022). The Al 2p spectrum (Figure 4.6e) indicates that the peak is at 73.35 eV. This binding energy corresponds with the presence of the aluminium, which has been embedded in the hematite lattice, which proves metallic aluminium (Al^0) which confirm plasmonic aluminium nanoparticles) in the α-Fe_2O_3 structure (Yuan *et al*., 2021).

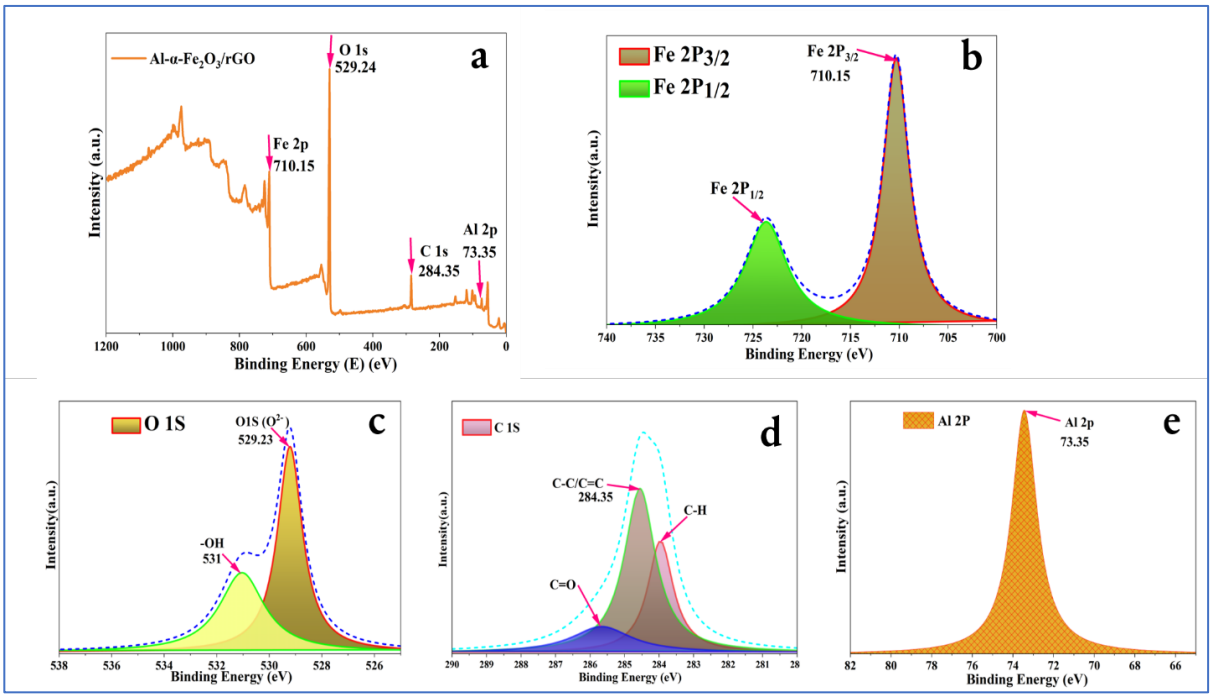

Figure 4.6. (a) High-resolution XPS profiles and survey scans of: (b) Fe 2p, (c)O 1s, (d) C 1S and (e) Al 2P of Al-α-Fe_2O_3/rGO nanostructure

4.4 Infrared Fourier-transform spectroscopy (FTIR) Analysis

The FTIR spectra of the synthesized GO, α-Fe_2O_3, Al-α-Fe_2O_3 and Al-α-Fe_2O_3/rGO nanostructures were examined in the 400–4000 cm^{-1} wavelength range, are shown in Figure 4.7. The FTIR spectrum for GO (Figure 4.7, green line) displays several absorption peaks with corresponding functional groups. The broad band at 3400 cm^{-1} stretching vibrations was for hydroxide groups(-OH) group and adsorbed water molecule; the C = O carboxyl group was at 1730 cm^{-1}; the C = C of aromatic rings was at 1630 cm^{-1}; the C – OOH of the carboxylic acids was stretched at 1378 cm^{-1}; 1226 cm^{-1} represents the epoxide (C–O) functional groups, while the alkoxy C–OH functional group was represented by the one at 1051 cm^{-1}. Thus, the existence of these oxygen-containing functional groups in the GO structure indicated that the precursor graphite was successfully oxidized to generate graphene oxide.

For α-Fe_2O_3(black line, Figure 4.7) and Al-α-Fe_2O_3 (red line, Figure 4.7), the FTIR spectra are dominated by absorption in the low wavenumber region, peaks typically observed at 548 cm^{-1} and 460 cm^{-1}, which are characteristic of Fe-O stretching vibrations of α-Fe_2O_3. The spectrum analysis of the Al-doped α-Fe_2O_3/rGO (Figure 4.7, blue line) displays both characteristic features, Fe-O and Graphene components. The characteristic Fe-O stretching vibrations 548 cm^{-1} and 460 cm^{-1} confirm the presence of α-Fe_2O_3. Compared to the GO spectrum, the intensity of oxygen-containing functional groups was significantly reduced or even absent in the Al-α-Fe_2O_3/rGO nanostructure. This reduction in oxygen-containing functional groups indicates the formation of reduced graphene oxide (rGO) from GO during the composite preparation. While some residual C-O stretching at 1226 cm^{-1} and C=C vibrations 1630cm^{-1}, the -OH stretching band around 3400 cm^{-1} is present, indicating restoring the graphitic network of the characteristics of rGO.

Overall, the FT-IR spectra of the Al-α-Fe_2O_3/rGO nanostructure confirm the formation of the composite.

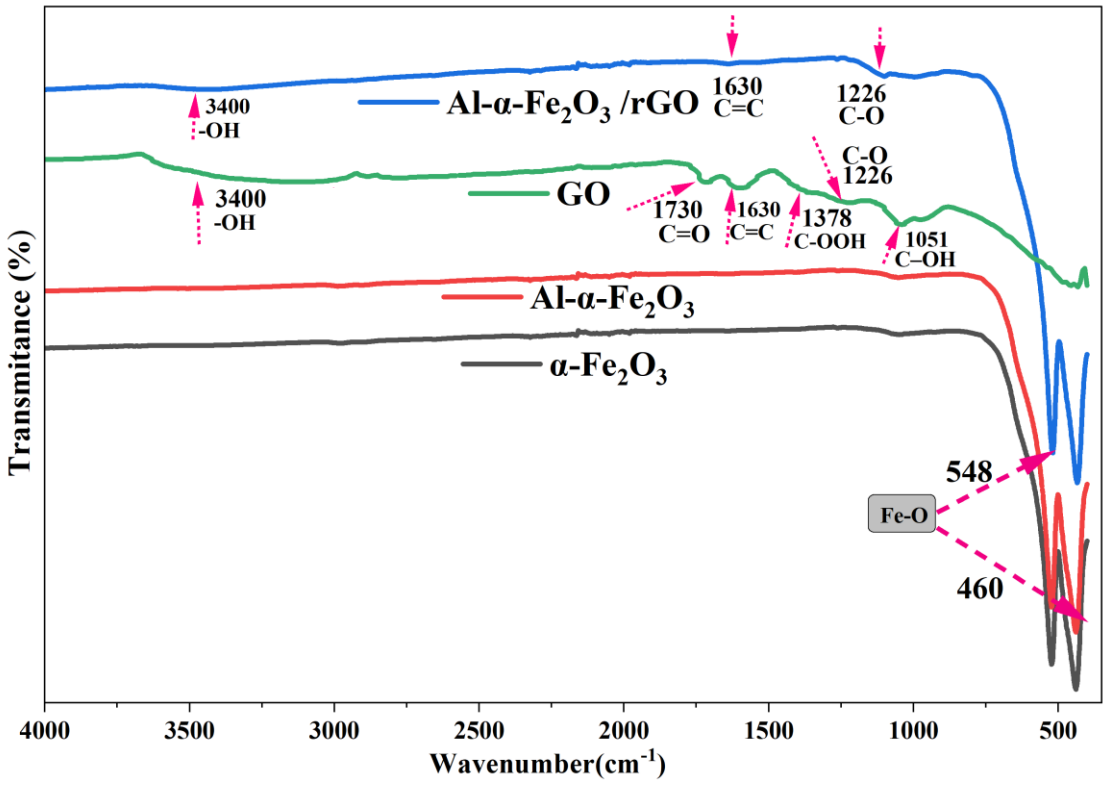

Figure 4.7. FTIR Spectrum of α-Fe_2O_3, Al-α-Fe_2O_3, Al-α-Fe_2O_3/rGO, and GO

4.5 Brunauer-Emmett-Teller (BET) Surface Area Analysis

Isotherms of nitrogen adsorption were measured to address specific surface area α-Fe_2O_3, Al-α-Fe_2O_3 and Al-α-Fe_2O_3/rGO nanostructures as indicated in Figure 4.8. All the samples display mesoporous features and all exhibit type II curves of the isotherms (Figure 4.8a, b&c), which means that the structure contains mesopores. Doping with aluminium and low concentration of graphene oxide greatly boosts the amount of nitrogen adsorbed and total surface area, as evidenced by the changes in the isotherm curves and increased surface area. The measured by Brunauer-Emmett-Teller (BET) analysis (Figure 4.8d) with the specific surface areas rising to about 2.4 m^2/g in the case of pure α-Fe_2O_3, 7.29 m^2/g in the case of Al-α-Fe_2O_3, and (Figure 4.8e) 33.32 m^2/g in the case of Al-α-Fe_2O_3/rGO. The increment in the surface area results in increased active sites in which photocatalytic reactions occur and optimal separation of charge and adsorption of reactant molecules in the process of degrading 2,4-D herbicides and hydrogen production (Dargahi, Hasani, *et al.*, 2021; Zhou *et al.*, 2020).

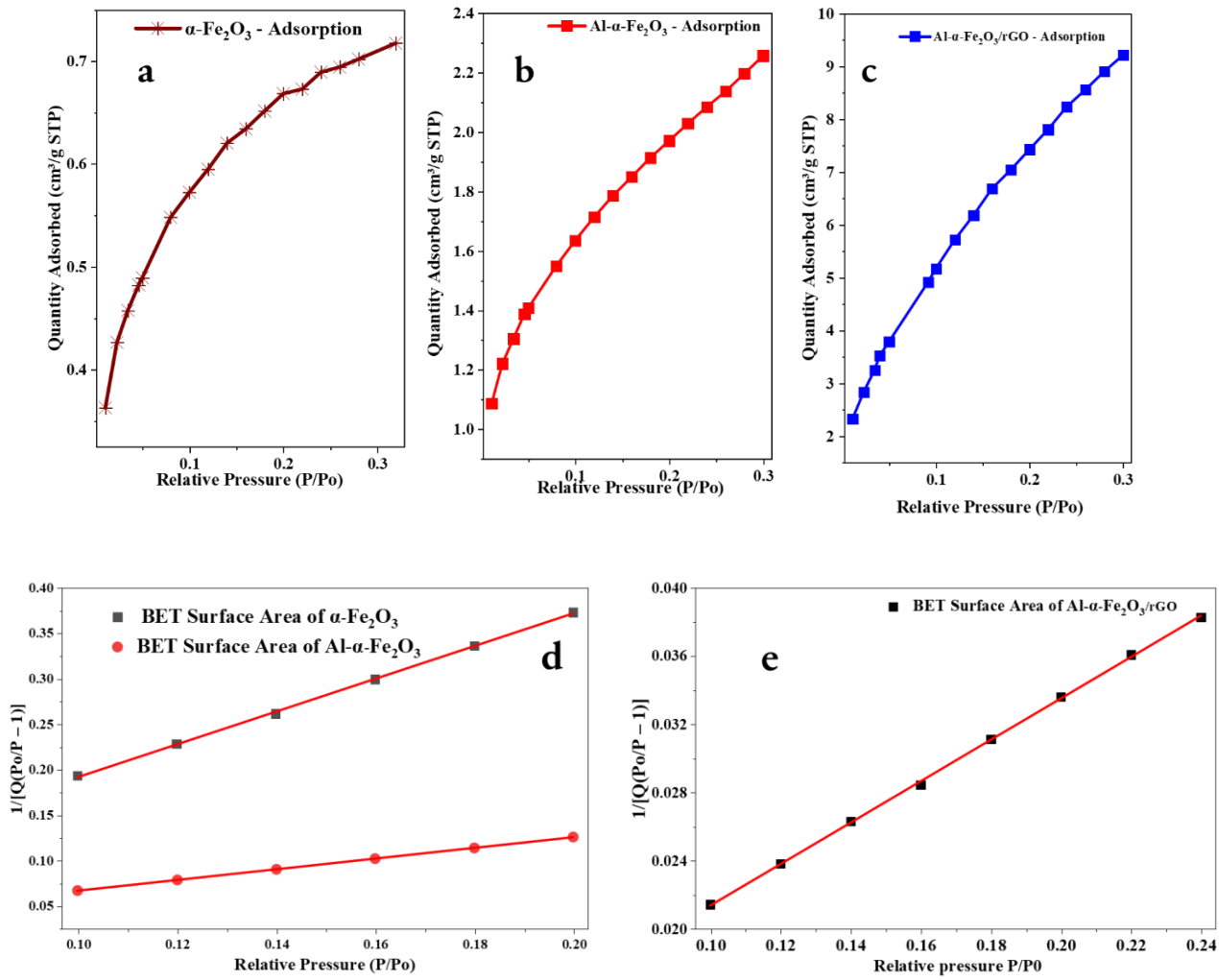

Figure 4.8. Nitrogen adsorption isotherms for (a) α-Fe_2O_3, (b) Al-α-Fe_2O_3, and (c) Al-α-Fe_2O_3/rGO nanostructures and (d) BET surface area plots for α-Fe_2O_3, Al-α-Fe_2O_3 and (e) BET surface area plots for Al-α-Fe_2O_3/rGO

4.6 Optical Properties Study

4.6.1 Ultraviolet -visible diffuse reflectance spectroscopy (UV-Vis DRS) Analysis

The UV-Vis DRS spectra of the synthesized α-Fe_2O_3, Al-doped α-Fe_2O_3 and Al-doped α-Fe_2O_3/rGO nanostructures are shown in Figure 4.9. The bandgap energies (Eg) of these materials were determined using the Kubelka-Munk function plot (shown in Equation 10) as shown in Figure 4.6, by the linear extrapolations in the plots.

$$[F(R)\ hv)]^{1/n} = A\ (hv\text{-}Eg) \quad \ldots\ldots\ldots\ldots\ldots\ldots\ldots\ldots\ldots\ldots\ldots\ldots 10$$

Where F(R) is the Kubelka-Munk function, which is expressed in equation 11, h is Planck's constant, n depends on the type of electron transition (n = 2 for indirect and n = 1/2 for direct transitions), A is a constant, v light frequency of light, and Eg is the band gap energy.

$$F(R) = \frac{K}{S} = \frac{(1-R)^2}{2R} \quad \ldots\ldots 11$$

Where R is reflectance, k absorption coefficient and S is the scattering coefficient.

From Figure 4.6a, it is observed that the bare α-Fe_2O_3 exhibits a bandgap energy of 2.07 eV. With increasing Al doping concentration (3% (Figure 4.8a), 5% (Figure 4.8c), and 7% (Figure 4.8d) the bandgap energy slightly decreases to values of 1.94 eV, 1.935 eV, and 1.917 eV, respectively. This reduction in bandgap suggests that Al doping introduces changes in the electronic structure, potentially enhancing visible light absorption. In addition to doping Al also exhibits plasmonic properties as a non-noble metal, thus inducing local surface plasmon resonance (LSPR), enhancing the electromagnetic field around the nanostructure, improving light absorption under visible light, and enhancing the efficiency(Altaf *et al.*, 2023). Additionally, the Al-doped α-Fe_2O_3/rGO (Figure 4.9 e) shows a further reduced bandgap energy of about 1.86 eV, indicating improved light harvesting capabilities due to synergistic effects between the doped with plasmonic properties of Al and rGO. These results are beneficial for photocatalytic and photoelectrochemical performance.

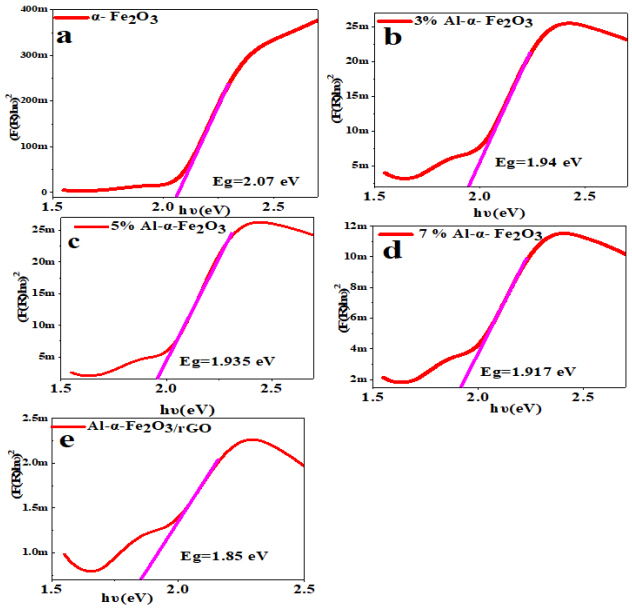

Figure 4.9. Tauc plot band gap calculation of synthesized, (a) α-Fe_2O_3, (b-d) Al-α-Fe_2O_3 and (e) Al-α-Fe_2O_3/rGO

4.6.2 Uv-vis Analysis

Figure 4.10 shows the UV-Vis absorbance spectra of α-Fe_2O_3, Al-α-Fe_2O_3 with various doping concentrations (3%, 5%, 7%), and Al-α-Fe_2O_3/rGO nanostructures. The absorption intensity increases progressively with Al doping concentration, reaching the highest absorbance in the Al-α-Fe_2O_3/rGO nanostructure. This indicates that in absorbance through the UV to visible range, light harvesting improved due to the combined synergetic effect of Al doping and rGO. As seen in the bandgap analysis, Al doping narrows the bandgap slightly and extends the absorption to visible light. Al also supports plasmonic properties, which can support LSPR to generate intense local electromagnetic fields near the nanostructures, further enhancing light absorption, facilitating charge carrier generation (T. Zhang *et al*., 2021). The Al-α-Fe_2O_3/rGO nanostructure shown in Figure 4.10 (green line) shows an absorbance increase and broadening of the absorption band, which could be attributed to the synergistic effect of Al plasmonics with the excellent conductivity of rGO that promotes efficient charge separation and transfer.

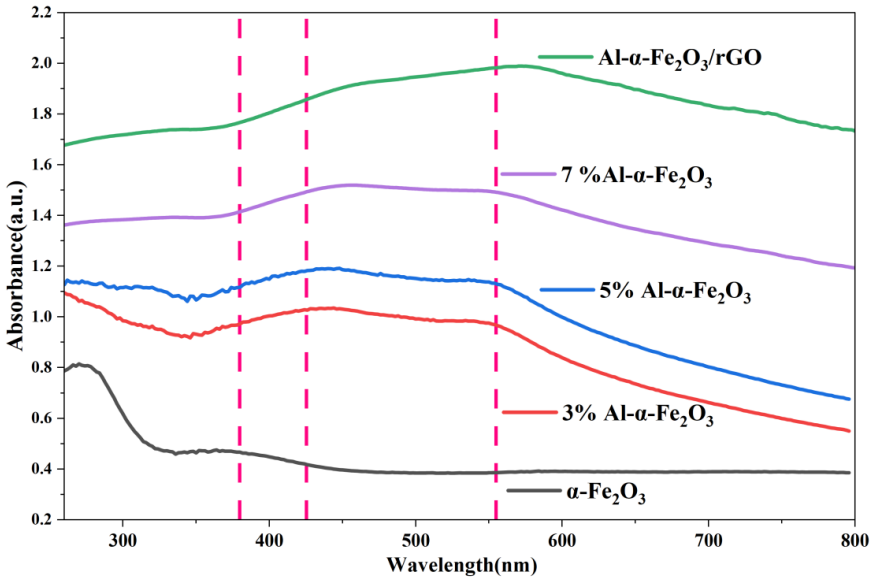

Figure 4.10. Uv-vis spectra of synthesized α-Fe_2O_3, Al-α-Fe_2O_3 and Al-α-Fe_2O_3/rGO

4.6.3 Photoluminescence (PL) Analysis

In addition to Uv-vis and Uv-vis DRS, the optical properties were further characterized by PL techniques. Figure 4.11a presents the photoluminescence (PL) spectra of α-Fe_2O_3 and Al-α-Fe_2O_3 nanostructures with doping concentrations 3,5,7, 9%. The PL peak emission centered at

650 nm corresponds to the recombination of photogenerated electron-hole pairs. As shown in Figure 4.11a, with increasing Al doping concentration, the intensity of the emission peak decreases, indicating that Al doping decreases the recombination of charge carriers(e-h). The reduction in PL intensity upon Al doping can be attributed induced LSPR enhances the local electromagnetic field, facilitating non-radiative energy transfer pathways and decreasing radiative recombination, thus lowering PL intensity (Khan & Idriss, 2017). The inset in the Figure 4.11a panel provides an enlarged view of the PL emission peak for the different α-Fe_2O_3 and Al-doped α-Fe_2O_3 samples. The 5% Al-doped nanostructure exhibits the lowest PL intensity among the doping levels characterized, suggesting it has the most effective suppression of electron-hole recombination, and it is the optimal doping concentration for enhancing photocatalytic performance (Khan & Idriss, 2017). Above or below this concentration, the recombination rate appears higher than the 5% Al-doped, as evidenced by the increased PL intensity in Figure 4.11a inset diagram. Figure 4.11b shows the PL spectra comparing α-Fe_2O_3, 5% Al-α-Fe_2O_3 (as optimum), and Al-α-Fe_2O_3/rGO. In both cases, the doped and composite samples show reduced PL intensity compared to pure α-Fe_2O_3, indicating suppressed electron-hole recombination and improved charge separation due to Al doping and composite formation (Zheng & Fang, 2021).

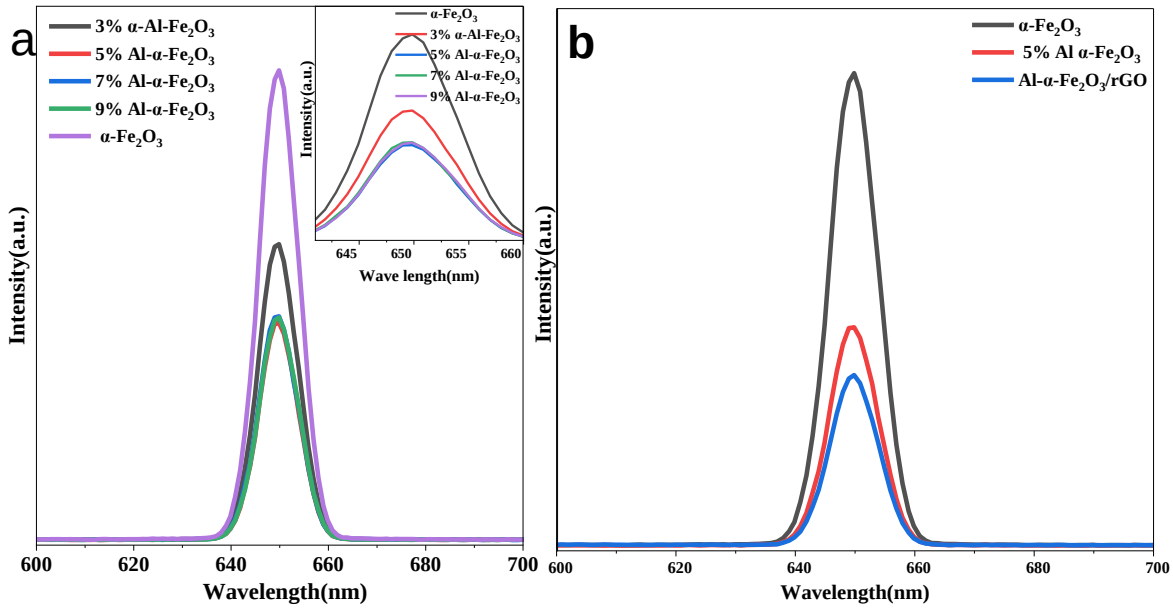

Figure 4.11. Photoluminescence (PL) spectra of α-Fe_2O_3, Al-α-Fe_2O_3 and Al-α-Fe_2O_3/rGO nanostructures.

4.7 Photocatalytic activity

4.7.1 pH_{PZC} determination

To conduct a photocatalytic performance experiment, it's crucial to understand the surface charge of the photocatalyst and the type of pollutant in the solution. pH_{PZC} was used to identify the point where the surface of the photocatalyst becomes negative or positively charged characteristic of materials, particularly adsorbents/catalysts, that describes the pH value at which the net electrical charge on the catalyst surface is zero. In the case of 2,4-D has a carrier anionic charge in aqueous solution requires a positively charged surface catalysis. The pHPZC of synthesized Al-α-Fe_2O_3/rGO nanostructure was found at 8.1. Thus, at a pH value below pHPZC (<8.1), the catalyst surface was positive and attracted the negative charge 2,4-D molecules (Alluhaybi *et al.*, 2023).

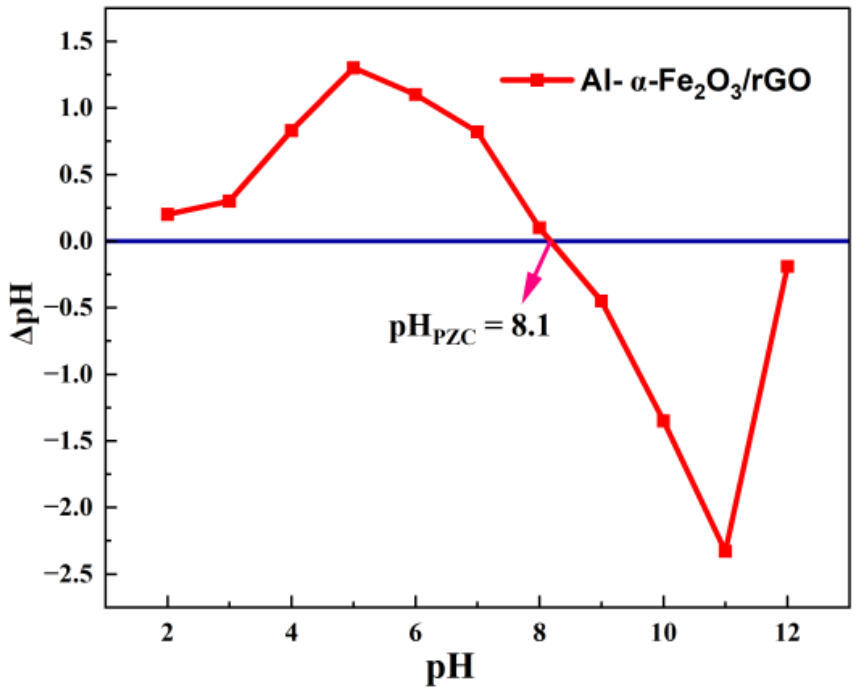

Figure 4.12. pHPZC of synthesized Al-α-Fe_2O_3/rGO nanostructure, determined in 0.01 M NaCl with 0.1 g/L adsorbent across an initial pH range of 2-12.

4.7.2 Factors That Affect Photocatalytic Activity of the Degradation of 2,4-D

4.7.2.1 Effect pH of Solution

The pH of a solution affects the photocatalytic breakdown of organic pollutants like 2,4-D in aqueous solutions. This study examined how solution pH in the range of 3-12 affects the photocatalytic activity for 2,4-D breakdown. Experiments were conducted using an initial 2,4-D concentration of 20 mg/mL and a catalyst dosage of 0.5 g/L (50 mg in 100 mL) over 30 minutes. The results illustrated in Figure 4.13a show that the photocatalytic removal efficiency of 2,4-D increased as the pH decreased, as the highest photocatalytic breakdown efficiency of 2,4-D was seen at acidic pH (pH =3).

This enhanced removal under acidic conditions can be related to the acid dissociation constant (pKa) of 2,4-D and the point of zero charge (pHPZC) of the synthesized Al-α-Fe_2O_3/rGO photocatalyst. The pKa of 2,4-D is 2.64, indicating that above this pH (Amiri *et al*., 2021). The 2,4-D molecule exists as an anion, and the pHPZC of the photocatalyst is 8.1; the catalyst surface is positively charged under pH values lower than 8.1. Therefore, the electrostatic attraction between the negatively charged 2,4-D ions at acidic conditions and the positively charged catalyst surface increased interaction and subsequently enhanced photocatalytic degradation efficiency. A similar conclusion regarding the effect of solution pH on 2,4-D degradation was reported in earlier investigations, showing that under acidic circumstances, enhanced adsorption and mineralization of 2,4-D were found due to favorable charge interactions (Amiri *et al*., 2021; Kamble *et al*., 2004)

4.7.2.2 Effect of Catalyst Dosage

The amount of catalyst dosage plays a significant role plays to determining the photocatalytic degradation of 2,4-D efficiency. In this study, the photocatalyst's performance for 2,4-D degradation was conducted at pH=3 with an initial 2,4-D concentration of 20 mg/L, and varying catalyst dosage ranging from 0.1-2.5 g/L over 30 minutes. As shown in Figure 4.13b, the photocatalytic effectiveness of Al-α-Fe_2O_3/rGO increased as the catalyst amount increased from 0.1 to 1 g/L. This shows that the photocatalyst's Al-α-Fe_2O_3/rGO increased surface area and active sites facilitate 2,4-D pollutant breakdown. However, a further increase in catalyst dosage beyond 1 g/L led to agglomeration of the catalyst (to make light scattering effects and prevent light penetration), a decrease in the active sites on the catalyst surface (Elimian *et al*., 2025),

thus reducing the generation of reactive species necessary for degradation. Therefore, 1 g/L was identified as the optimal catalyst dosage for photocatalytic degradation of 2,4-D under the studied conditions.

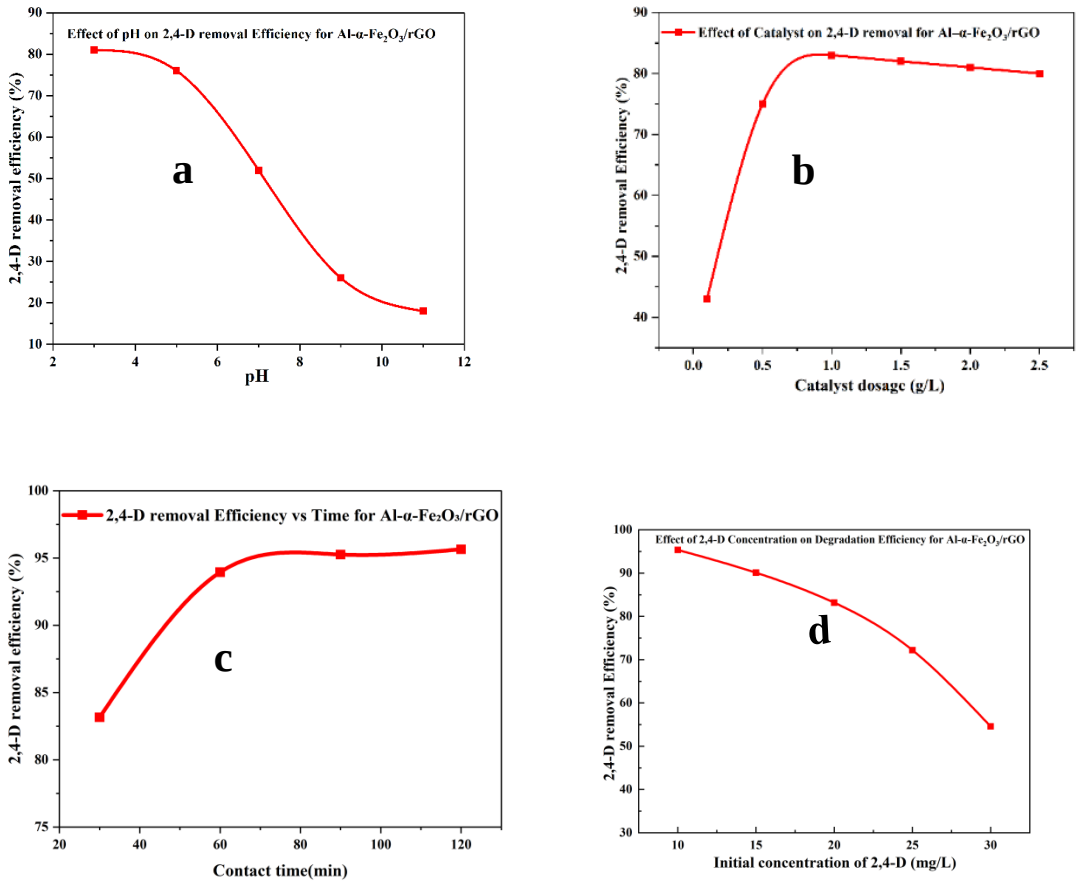

Figure 4.13. Effect of operational parameters of 2,4-D using Al-α-Fe_2O_3/rGO nanostructure: (a) pH, (initial concentration = 20 mg/L, dosage =0.5 g/L, time = 30-minute, pH= 3-11, (b) catalyst dosage, (initial concentration = 20 mg/L, dosage = 0.1-2.5 g/L, time = 30-minute, pH= 3, (c) irradiation time, (initial concentration = 20 mg/L, dosage = 1 g/L, time = 0-120-minute, pH= 3) (d) initial 2,4-D concentration of 2,4-D,(initial concentration = 10-30 mg/L, dosage = 1 g/L, time = 60-minute, pH= 3)

4.7.2.3 Effect of Contact Time

The contact time between the photocatalyst and 2,4-D solution critically influences the degradation efficiency. In this study, the photocatalyst's performance for 2,4-D degradation was conducted at pH=3 with an initial 2,4-D concentration of 20 mg/L, catalyst dosage 1 g/L over a varying time interval 0-120 minutes. Figure 4.13c clearly illustrates that increasing contact time duration improves 2,4-D removal efficacy for up to 60 minutes, which this most likely because of unsaturated active sites on the photocatalyst surface that allow for ongoing pollutant breakdown. Above 60 minutes, the removal efficiency plateaus, indicating that equilibrium has been reached and that additional contact time results in minimal incremental degradation (Mehralipour *et al*., 2023). Therefore, 60 minutes were selected as the optimum contact time in this study.

4.7.2.4 Effect of Initial 2,4-D Concentration

The study assessed the impact of initial 2,4-D concentrations ranging from 10-30 mg/L on photocatalyst efficiency under specific conditions: pH = 3, catalytic dosage = 1 g/L, and for 60 minutes. Figure 4.13d shows that the photocatalyst efficiency of Al-α-Fe_2O_3/rGO decreases with higher 2,4-D concentrations. The results indicate that occupying an empty active site on the photocatalyst causes the catalyst surface to become saturated and inactivated, resulting in lower degrading efficiency (Amiri *et al*., 2021). Therefore, 10 mg/L was identified as the optimal initial concentration of 2,4-D under the studied conditions.

The UV-Visible spectroscopy measures the absorbance of 2,4-D at 283 nm (Mehralipour *et al.*, 2023). Figure 4.14 shows a progressive decrease in the characteristic absorbance peak of 2,4-D around 283 nm as the reaction time increases from 0 to 120 minutes. This decrease indicates the effective photocatalytic degradation of 2,4-D by the Al-α-Fe_2O_3/rGO nanostructure under the optimized conditions of pH 3, 1 g/L catalyst dosage, 10 mg/L 2,4-D concentration, and 60 minutes reaction time, achieved 93.97% degradation efficiency.

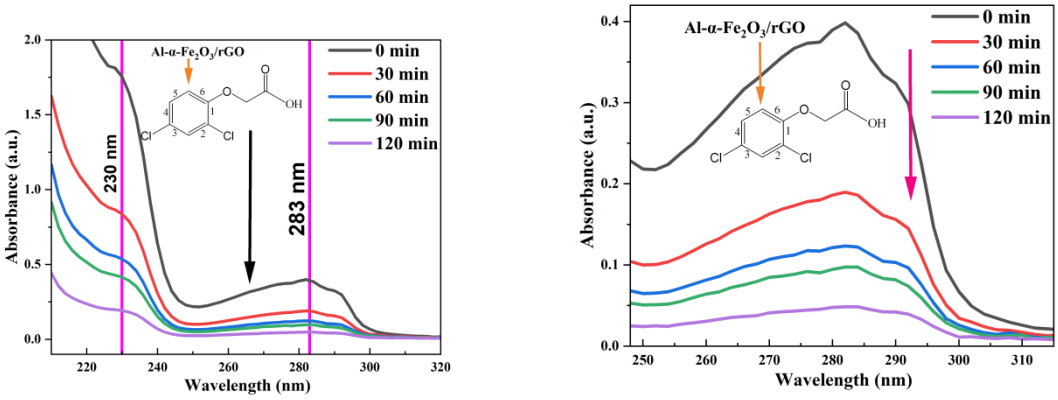

Figure 4.14. Photocatalytic Degradation of 2,4-D (pH 3, 1 g/L Catalyst,10 ppm, time up to 120 min) by Al-α-Fe_2O_3/rGO

4.7.3 Comparative Photocatalytic Efficiency of Synthesized Materials

This section evaluates and compares the photocatalytic performance of various synthesized materials, such as bare α-Fe_2O_3, Al-α-Fe_2O_3, and Al-α-Fe_2O_3/rGO nanostructures, as shown in Figure 4.15, to understand the effect of Al doping and rGO incorporation on the photocatalytic degradation efficiency of 2,4-D under identical optimal conditions. As indicated in Figure 4.15a, the shaded area, an adsorption equilibrium was detected for 30 minutes before light exposure, with minimal 2,4-D adsorption occurring on the catalyst surfaces in dark conditions, indicating poor pollutant removal without photocatalysis. Under visible light, the normalized concentration ratio (C/C_0) of 2,4-D decreases with increasing irradiation time for all nanostructures, including α-Fe_2O_3, Al-α-Fe_2O_3, and Al-α-Fe_2O_3/rGO, indicating progressive pollutant 2,4-D degradation. The degradation efficiency was calculated by the formula $\frac{1-C}{Co}$*100%, where C_0 is the initial concentration and C is the concentration at a given irradiation time (Ye *et al.*, 2022). Among the three, the Al-α-Fe_2O_3/rGO nanostructure exhibited the highly efficient degradation of 2,4-D and reduced its concentration close to zero within 120 min. This highly exhibited efficiency due to the synergistic effect of aluminium doping and reduced graphene oxide incorporation, improved visible light absorption through localized surface plasmon resonance and efficient electron transport (Al Marzouqi & Selvaraj, 2023; Chu *et al.*, 2024). Similarly, Al-α-Fe_2O_3 nanostructures showed improved performance compared to α-Fe_2O_3 for photocatalytic activity

and removal efficiency. Al-α-Fe_2O_3 improved degradation efficiency is due to aluminium doping, which creates defect states and improves charge separation(Yin *et al.*, 2023).

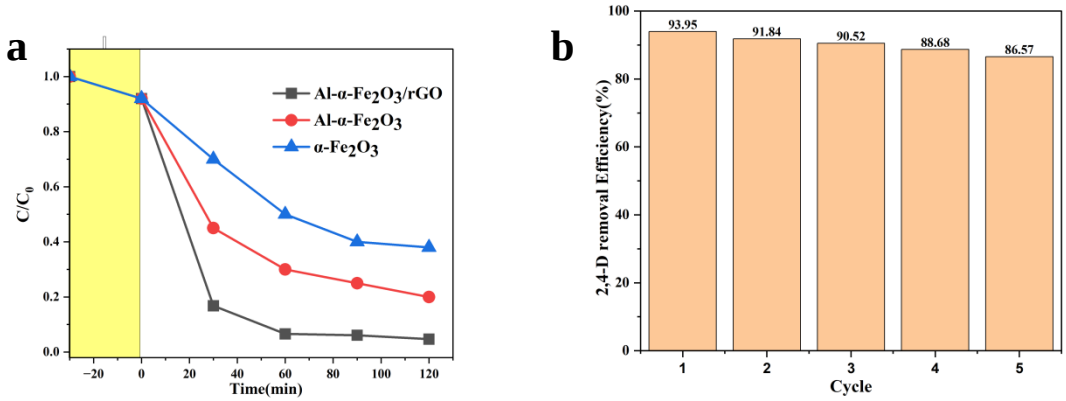

Figure 4. 15. Photocatalytic degradation performance of α-Fe_2O_3, Al-doped α-Fe_2O_3, and Al-α-Fe_2O_3/rGO nanostructure over time in 2,4-D solution (pH 3, 1 g/L Catalyst,10 ppm and 60-minute) (a) and reusability test of Al-α-Fe_2O_3/rGO for 2,4-D degradation over 5 cycles (pH 3, 1 g/L Catalyst,10 ppm and 60-minute) (b)

4.7.4 Photocatalyst Reusability and Stability Test

To perform photocatalyst reuse, 1 g/L of Al-α-Fe_2O_3/rGO was added to 10mg/L 2,4-D in 100ml of aqueous solution and exposed to visible light for 60 minutes for five cycles. After each process, the catalyst was centrifuged, cleaned with water and ethanol, and dried before reuse. Figure 4.15b shows that the removal efficiencies of 2,4-D were observed as 93.95% for the first cycle, 91.84% for the second, 90.52% for the third, 88.68% for the fourth, and 86.57% for the fifth cycle. The minor efficiency drop may be observed due to mechanical catalyst loss during recovery (Silva *et al.*, 2024) and the possibility of active site blocking by intermediate degradation by-products(Yang *et al.*, 2023).

4.7.5 Photocatalytic Degradation Kinetics

The kinetics of 2,4-D degradation of α-Fe_2O_3, Al-α-Fe_2O_3, and Al-α-Fe_2O_3/rGO photocatalysts were investigated using the pseudo-first-order kinetic model, as shown in Figure 4.16. The rate constants (k) were calculated by graphing ln (C_0 / C_t) *versus* irradiation time (Yasmeen *et al.*, 2024), where C_0 and C_t are the initial and concentrations at time t of 2,4-D, respectively. The plot of ln (C0 / Ct) *versus* time shows linear behavior for all three photocatalysts, with

correlation coefficients (R^2>0.98), confirming the applicability of the pseudo-first-order kinetic model. The rate constant k for the Al-α-Fe_2O_3/rGO nanostructure was 0.02577 min^{-1}, 0.01481 min^{-1} for Al-α-Fe_2O_3 and 0.00631 min^{-1} for α-Fe_2O_3. The combination of reduced graphene oxide incorporation with aluminium doping improves visible light absorption and effective charge carrier separation and transfer, due to the increased rate constant of Al-α-Fe_2O_3/rGO. On the other hand, because of its low conductive efficiency and higher electron-hole recombination rates, α-Fe_2O_3 showed the slowest kinetics (Wang *et al.*, 2021).

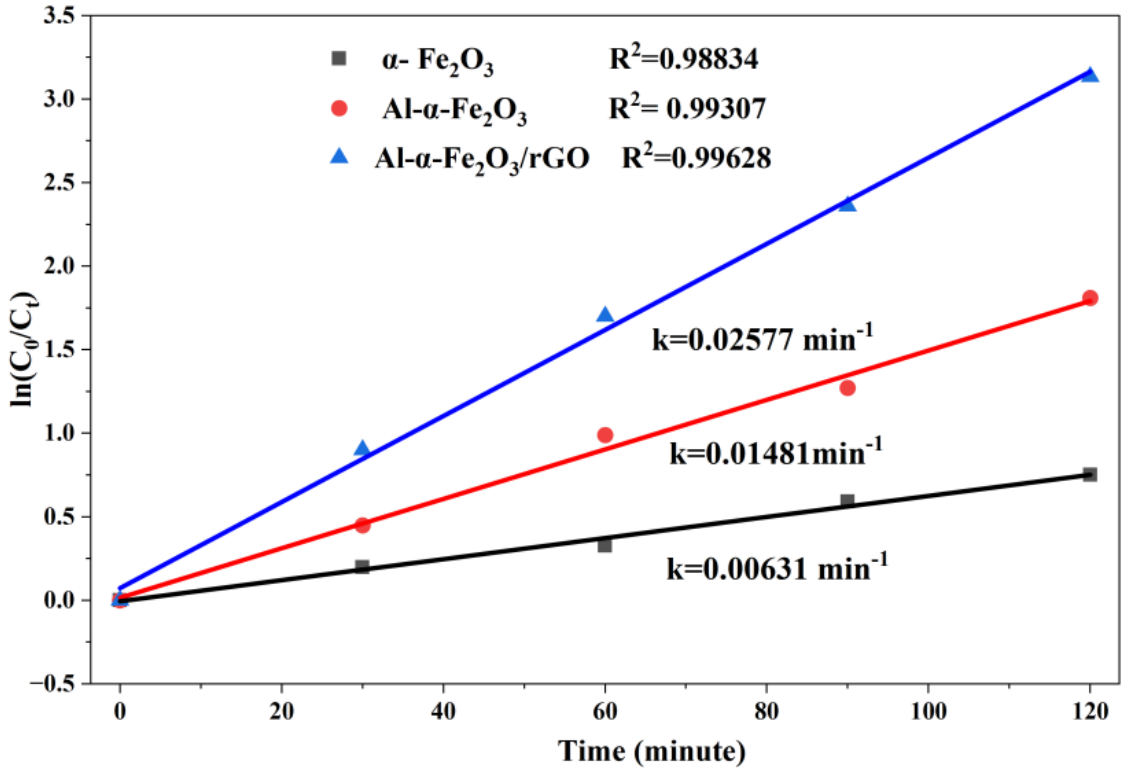

Figure 4. 16. Pseudo first-order kinetic model for 2,4-D removal of α-Fe_2O_3, Al-α-Fe_2O_3, and Al-α-Fe_2O_3/rGO nanostructures. The experiments were conducted with an initial 2,4-D concentration of 10 ppm, at pH 3, and a catalyst dosage of 1 g/L. The rate constants (k) and correlation coefficients (R^2) for each material are: α-Fe_2O_3 (k = 0.00631 min^{-1}, R^2 = 0.98834), Al-α-Fe_2O_3 (k = 0.01481 min^{-1}, R^2 = 0.99307), and Al-α-Fe_2O_3/rGO (k = 0.02577 min^{-1}, R^2 = 0.99628).

4.7.6 Degradation Mechanism of 2,4-D

The degradation mechanism diagram for the photocatalytic breakdown of 2,4-D by Al-α-Fe_2O_3/rGO is schematically shown in Figure 4.17. The photocatalytic degradation mechanisms were started, the photocatalyst absorbs photons with energy equal to or greater than its band gap, to generate electron-hole pairs(Zhang *et al*., 2022). The holes migrate to the VB, whereas electrons migrate; they participate in redox reactions, producing reactive oxygen species such as hydroxyl (· OH) and superoxide radicals(O_2^-). These radicals, ROS, are highly reactive and attack organic pollutants(2,4-D), leading to their degradation into harmless end products (Mehralipour *et al*., 2023). In plasmonic photocatalysts, localized surface plasmon resonance (LSPR) further enhances visible light absorption and charge carrier generation(Zhao *et al*., 2021), improving overall photocatalytic efficiency.

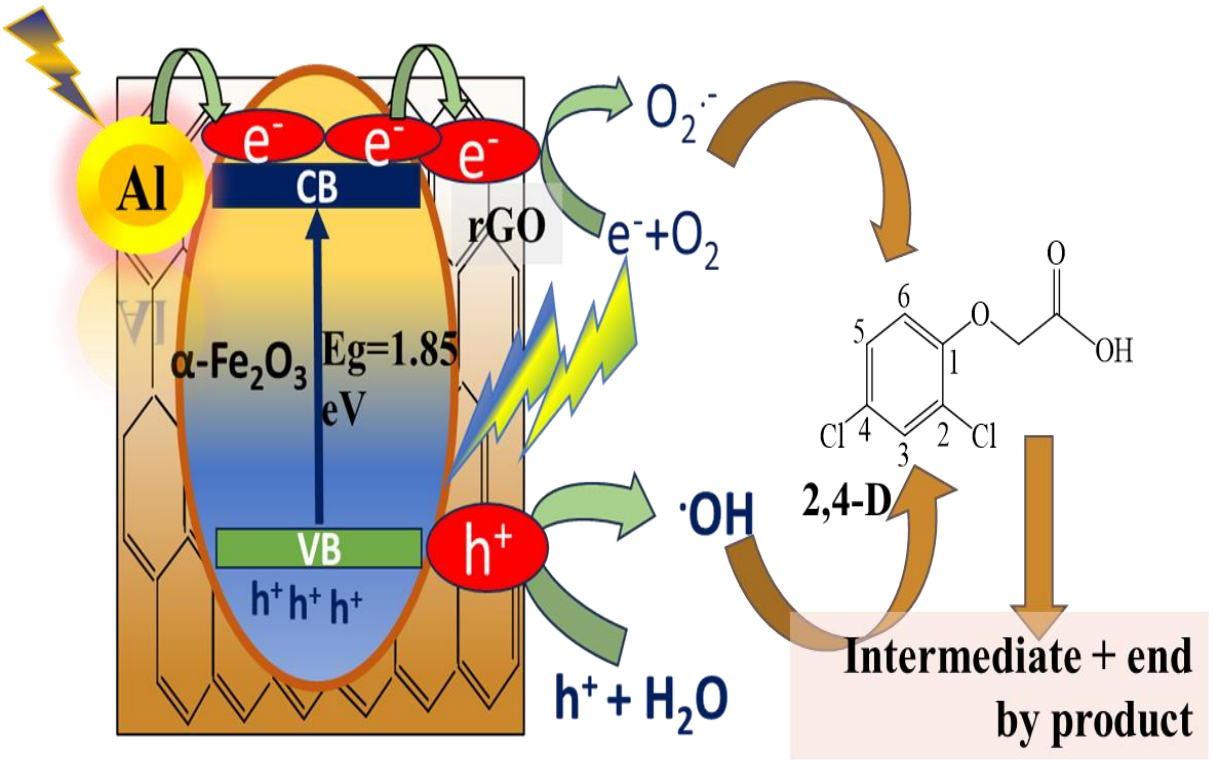

Figure 4.17. Photocatalytic degradation mechanism of 2,4-D using Al-α-Fe_2O_3/rGO nanostructures.

4.7. 7 Comparison of the catalytic degradation of 2,4-D with other literature reports

Table 3. Comparison of the catalytic degradation of 2,4-D with other literature reports

Name of Catalyst	Light source used	Catalyst dosage (g/ L)	2,4-D initial concentration (ppm)	Reaction time (min)	Degradation efficiency (%)	Reference
Mn-doped ZnO/Graphene	LED	2	10	120	66.2	(Ebrahimi *et al*., 2020)
rGO/$ZnBi_2O_4$ (2% rGO)	Visible	1	30	120	90	(Tho *et al*., 2020)
CNQDs (1%)/$CuBi_2O_4$	visible light	1	33	110	92.35	(Huong *et al*., 2024)
$ZnIn_2S_4$/g-C_3N_4	visible light	20	100	180	90	(Qiu *et al*., 2016)
ZnO/γ-Fe_2O_3	UVA	20	20	240	52.5	(Lee & Abdullah, 2015)
Al- α-Fe_2O_3/rGO	visible light	10	10	60	93.95	This study

4.8 Photoelectrochemical Catalytic Performance Test Result

4.8.1 Cyclic Voltammetry (CV) Characterization

The cyclic voltammograms (CV) of α-Fe_2O_3 doped with different amounts of Al (0, 3, 5, 7, and 9%) at a scan rate of 50 mV/s *versus* RHE are shown in Figure 4.18a. The curves show the effect of Al doping on the current density and the electrochemical activity. When doping is increased, the redox properties are usually altered, which is due to changes in charge transport, defect density, and surface-active sites (Irshad *et al*., 2025). The optimum amount of Al of 5% comes out as the optimum amount of doping as it exhibits the highest redox peak currents and hence better electrochemical performance as we have seen than other lower and higher doping concentrations. This suggests that the highest CV curve area makes the highest specific capacity in the case of 5% Al doping.

In Figure 4.18b, the curves of CV of Al-α-Fe_2O_3/rGO nanostructure are presented at various scan rates (20-100 mV/s). With increasing scan rate, the peak currents rise in line with the classic Randel's Sevcik behavior, in which the square root of the scan rate is proportional to peak current I p, where the process is diffusion-controlled (Pillai *et al*., 2022). In Figure 4.18c, CV cycles (1-5) of Al-α-Fe_2O_3/rGO nanostructure are repeated. The successive cycles' coincidence suggests an excellent electrochemical stability and reversibility (Wu *et al.*, 2021). The reproducible redox peaks across cycles confirm the stability of the nanostructure electrode, which is an important consideration for sustainable operation in photoelectrochemical(Wu *et al*., 2021). Figure 4.18d shows the CV of a bare fluorine-doped tin oxide (FTO) electrode at 50 m V/s vs. Ag/AgCl. The current-potential profile with quasi-rectangular current and potential attempt with no major redox peaks means that there is no faradaic background, which confirms that the observed features in the remaining panels are due to the existence of active materials (Aranda *et al*., 2019).

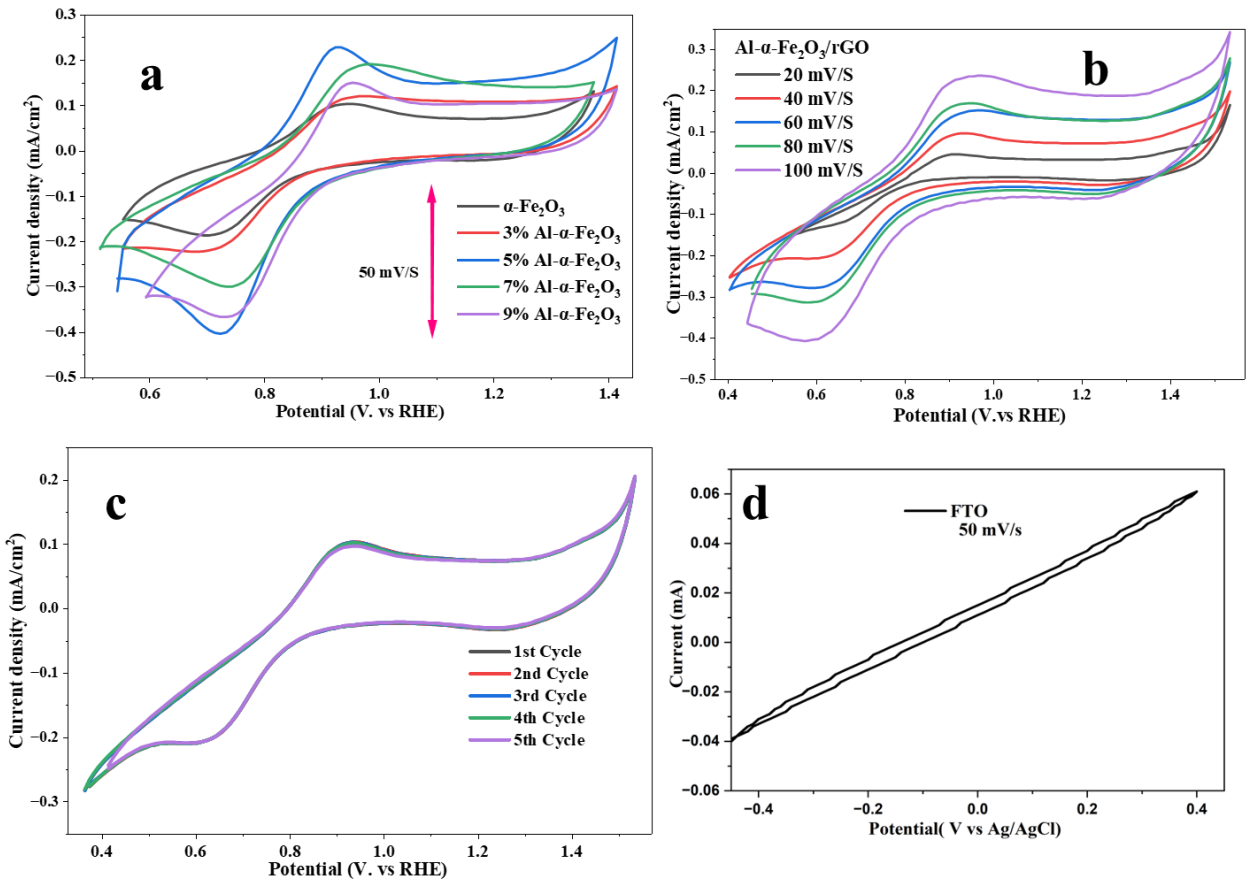

Figure 4.18. CV curves of (a) α-Fe_2O_3 and Al-α-Fe_2O_3 with different doping concentrations, (b)Al-α-Fe_2O_3/rGO nanostructure with different scan rates, (c) CV cycles of Al-Fe_2O_3/rGO and (d) FTO substrate. All measurements were performed in 1 M NaOH within a potential range of -0.4 V to 0.41 V vs Ag/AgCl

4.8.2 Electrochemical Impedance Spectroscopy (EIS)

An electrochemical impedance spectroscopy (EIS) study was carried out to gain further factors responsible for the significant increase in photocurrent density observed in the Al-α-Fe_2O_3/rGO nanostructure compared to the Al- α-Fe_2O_3 and α-Fe_2O_3. The EIS Nyquist plot is presented in Figure 4.18, which clearly shows that the semicircle for the Al- α-Fe_2O_3/rGO (blueline) is smaller than that of the α-Fe_2O_3 (blackline) and Al- α-Fe_2O_3 (redline) nanostructures, resulting in improved charge carrier separation and transport. The EIS of α-Fe_2O_3 (Figure 4.19, black line) shows the largest semicircle, which results in high charge transfer resistance (Rct), correlating with the lowest photocurrent density observed in the LSV measurements (Figure 4.20). Al-α-

Fe_2O_3, the enhanced Rct is associated with a higher photocurrent density that indicates the good separation of charges and electronic conductivity of α-Fe_2O_3 doped with Al (Bakhtiargonbadi *et al.*, 2020). Moreover, the Al-α Fe_2O_3/rGO nanostructure has a lower Rct, which was explained by the charge transport supported by the synergetic effect of Al and rGO (Liang & Cheng, 2018). Such enhancement charge transfer does this to enhance photocurrent performance, which was about 22.28 times higher than bare α-Fe_2O_3 in LSV. Such integrated outcomes (LSV and EIS) revealed that, in the synergistic impacts of the Al doping, based on the plasmonic enhancement, and rGO conductive pathways, the PEC activity is greatly enhanced by the better dynamics of charge carriers and interfacial charge transfers (Bashir *et al.*, 2023).

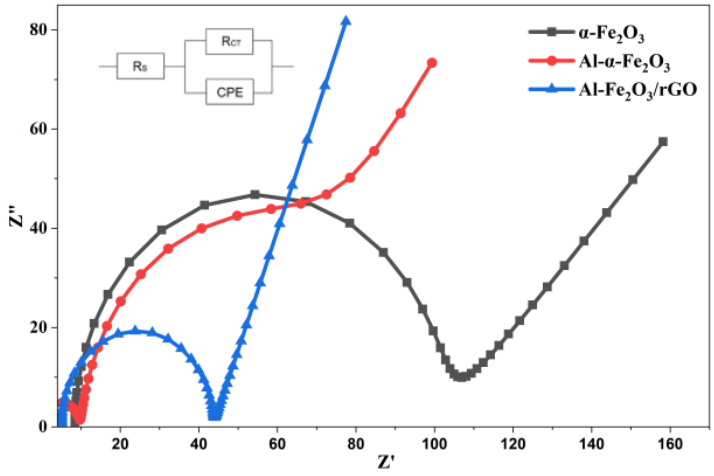

Figure 4.19. Nyquist plots from EIS of α-Fe_2O_3, Al- α-Fe_2O_3, Al- α-Fe_2O_3/rGO nanostructures in 1M NaOH electrolyte solution.

4.8.3 Linear Sweep Voltammetry (LSV) and Chronoamperometric (CA) Analysis

Figure 4.20 presents the LSV measurements of α-Fe_2O_3, Al-α-Fe_2O_3, and Al-α-Fe_2O_3/rGO photoanode under light illumination. At 1.23 V *vs* RHE, the photocurrent density of α-Fe_2O_3 was 0.140 mA/cm^2, whereas the photocurrent densities of Al- α-Fe_2O_3, Al- α-Fe_2O_3/rGO were 1.32 and 3.12 mA/cm^2 under continuous illumination, respectively, with a 1.23 V *vs* RHE. The doping of Al into α-Fe_2O_3 enhanced the photocurrent density to 1.32mA/cm^2. This enhancement is attributed to the dual role Al dopant acts as both an electronic inducer (Kleiman-Shwarsctein *et al.*, 2010) and a plasmonic enhancer (Gao *et al.*, 2012), which improves charge carrier separation and induces light absorption through the plasmonic effect. Specifically, the

photocurrent density value of Al- α-Fe_2O_3 was 9.42 times larger than the bare α-Fe_2O_3. Furthermore, the Al- α-Fe_2O_3/rGO nanostructure increases photocurrent density further to 3.12 mA/cm^2 under the same conditions, which is about 22.28 times larger than that of α-Fe_2O_3. This value indicates the synergetic effect of plasmonic enhancement of Al for light harvesting. (Gao *et al*., 2012) and superior charge transport facilitated by the rGO network(Vinoth *et al*., 2016).

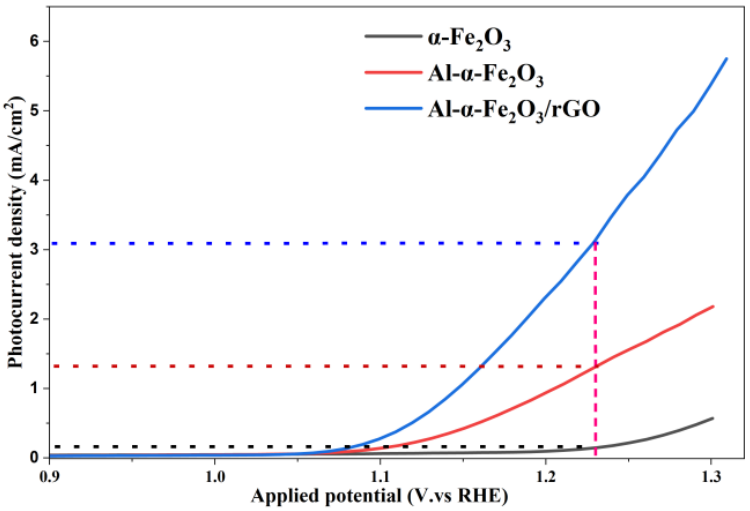

Figure 4.20. LSV plot curve for α-Fe_2O_3, Al-α-Fe_2O_3 and Al-α-Fe_2O_3/rGO photoanode in 1M NaOH electrolyte with a scan rate of 5 mV/S.

Figure 4.21a shows the chronoamperometric response of Al-α-Fe_2O_3 and Al-α-Fe_2O_3/rGO photoanode under periodic light illumination with light ON-OFF cycles of 25 seconds. The Al-α-Fe_2O_3/rGO photoanode exhibits a stable photocurrent density of 3.12 mA/cm^2 during each light illumination period, whereas Al-α-Fe_2O_3 produced a photocurrent density of 1.32 mA/cm^2 under the same conditions. Both photoanode electrodes displayed fast and reproducible switching behavior, indicating efficient charge carrier separation and rapid photo response. Figure 4.21b further showed that, not only stronger responses to light but also Al-α-Fe_2O_3/rGO longer term stability, the electrode maintains Photo current density 3.12 mA/cm^2 under continuous light illumination at 1.23 V *vs* RHE for 35000S. The enhanced photocurrent stability and magnitude of Al-α-Fe_2O_3/rGO further confirm its superior charge transport capabilities and catalytic activity, consistent with the results from LSV and EIS analyses.

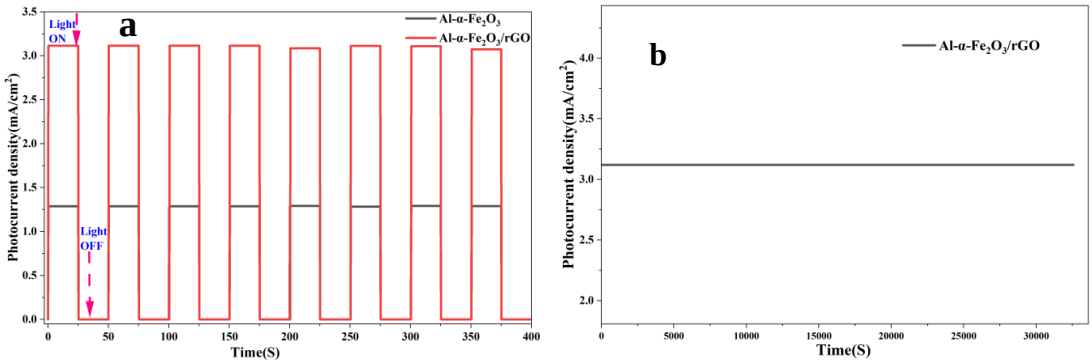

Figure 4.21 (a) Chronoamperometry (CA) photocurrent response of Al-α-Fe_2O_3 and Al-α-Fe_2O_3/rGO nanostructures and (b) Photocurrent stability test of the Al-α-Fe_2O_3/rGO nanostructure under continuous illumination at 1.23 V *vs* RHE in 1M NaOH electrolyte.

2.8.4 Mechanism of photoelectrochemical (PEC) water splitting by Al-α-Fe_2O_3/rGO photoanode

The mechanism of PEC water splitting using an Al-α-Fe_2O_3/rGO photoanode and Pt as the cathode was shown in Figure 4.22. When incident light (hv) shines upon Al-α-Fe_2O_3/rGO photoanode, the electron-hole pairs are produced. The conduction band (CB) of the α-Fe_2O_3 transfers the photogenerated electrons to the reduced graphene oxide (rGO) layer, enabling quick movement to the external circuit and reducing recombination. The circulated electrons pass to the outer circuit to Pt cathode, where they reduce the protons ($4H^+$) to generate hydrogen gas ($2H_2$). At the same time, the holes produced by the photogeneration that are in the valence band (VB) in the α-Fe_2O_3 are involved in the oxidation of water molecules on the photoanode surface to generate oxygen gas(O_2) and release more protons ($4H^+$).

At photoanode

$$2H_2O(l) \rightarrow O_2(g) + 4H^+ + 4e^-$$

At the cathode

$$4H^+ + 4e^- \rightarrow 2H_2(g)$$

The overall photoelectrochemical water splitting reaction

$$2H_2O(l) \rightarrow 2H_2(g) + O_2(g)$$

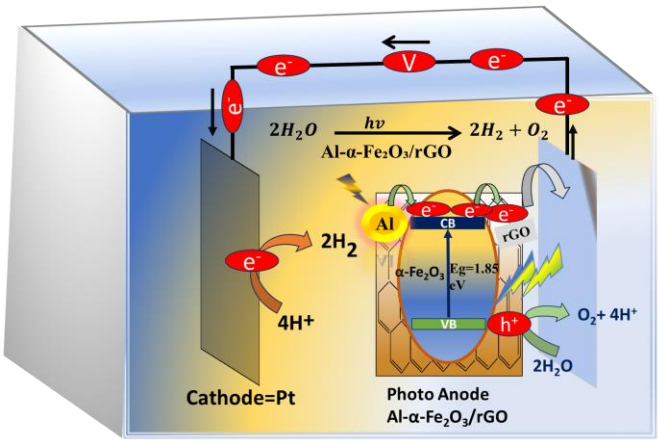

Figure 4. 22. Schematic illustration mechanism of photoelectrochemical water splitting of Al-doped α-Fe_2O_3/rGO Photoanode

Table 4. Comparison of the photocurrent density of the photoanode for PEC water splitting

Photoanode material	Bias (V *vs.* RHE)	Photocurrent Density (mA cm^{-2})	Electrolyte/ Conditions	References
FeOOH/H-TiO_2 nanorods array	1.23	1.0	1 M NaOH, 1 sun	(Panzeri *et al.*, 2021)
CdS/CdSe/TiO_2	1.23	0.94	1 M NaOH, 1 sun	(Ahmed *et al.*, 2018)
β-Bi_2O_3 (nanoporous)	1.23	0.95	1 M NaOH, 1 sun	(Chitrada *et al.*, 2016)
BVO/rGO (10% rGO)	1.23	0.55	1 M NaOH	(Soltani et al., 2018)
CoOOH/(Ti,C)-Fe_2O_3 nanorods	1.23	1.85	1 M NaOH	(Ye *et al.*, 2018)
Al-α-Fe_2O_3/rGO	1.23	3.12	1M NaOH, 1 sun	This study

CHAPTER FIVE

CONCLUSIONS AND RECOMMENDATIONS

5.1 Conclusions

In conclusion, this study synthesized Al-α-Fe_2O_3/rGO nanostructures using the sol-gel technique with sonication, followed by comprehensive characterization, and the result confirmed the successful synthesis of Al-α-Fe_2O_3/rGO. The Al-α-Fe_2O_3/rGO photocatalyst demonstrated the outstanding performance degradation of 2,4-D, achieving 93.95% removal efficiency within 60 minutes under visible light. In PEC water splitting to produce hydrogen, the Al-α-Fe_2O_3/rGO photo anode exhibited a photocurrent density of 3.12 mA/cm² at 1.23 V *vs* RHE, which is 22.28 times higher than bare α-Fe_2O_3, and exhibited excellent stability over 35,000 seconds under continuous illumination. The enhanced attributes of Al doping improve charge separation and reduce recombination through a plasmonic enhancer, which induces localized surface plasmon resonance (LSPR) to increase visible light absorption and promote hot electron generation. The rGO coupled provides an efficient charge transport pathway and results in high electrical conductivity. Overall, these findings indicate the potential of Al-α-Fe_2O_3/rGO nanostructures as efficient, stable, and low-cost plasmon-enhanced photocatalysts for environmental remediation and solar-driven PEC hydrogen production

5.2 Recommendations

To maximize PEC and photocatalytic performance, future studies should study the advanced spectroscopy can reveal comprehensive paths of plasmonic enhancement and charge transfer in Al-α-Fe_2O_3/rGO nanostructure. Research should also explore the scalability and practical application of these nanostructures in actual wastewater treatment systems and large-scale PEC hydrogen production. Furthermore, expanding the investigation to include various organic contaminants and herbicides to assess the broad applicability and adaptability of Al-α-Fe_2O_3/rGO photocatalyst.

REFERENCES

Adfar, Q., Hussain, S., & Maktedar, S. S. (2025). Insights into energy and environmental sustainability through photoactive graphene-based advanced materials: perspectives and promises. *New Journal of Chemistry*.

Agrawal, A., Cho, S. H., Zandi, O., Ghosh, S., Johns, R. W., & Milliron, D. J. (2018). Localized surface plasmon resonance in semiconductor nanocrystals. *Chemical Reviews*, *118*(6), 3121-3207.

Ahamad, A., Ahamad, J., & Javed Naim, M. (2023). Current perspective on pesticides: Their classification, behaviour, potential use and toxic effects. *Journal of Angiotherapy*, *7*(1).

Ahmad, M. F., Ahmad, F. A., Alsayegh, A. A., Zeyaullah, M., AlShahrani, A. M., Muzammil, K., Saati, A. A., Wahab, S., Elbendary, E. Y., & Kambal, N. (2024). Pesticides' impacts on human health and the environment, with their mechanisms of action and possible countermeasures. *Heliyon*.

Ahmed, R., Xu, Y., & Zangari, G. (2018). Photoelectrochemical activity of CdS/CdSe deposited onto TiO_2 photoanodes: comparing performance with vs. without sacrificial reagents. *ECS Transactions*, *85*(13), 1031.

Akash, S., Sivaprakash, B., Rajamohan, N., Pandiyan, C. M., & Vo, D.-V. N. (2022). Pesticide pollutants in the environment–A critical review on remediation techniques, mechanism and toxicological impact. *Chemosphere*, *301*, 134754.

Al Marzouqi, F., & Selvaraj, R. (2023). Surface plasmon resonance induced photocatalysis in 2D/2D graphene/g-C_3N_4 heterostructure for enhanced degradation of amine-based pharmaceuticals under solar light illumination. *Catalysts*, *13*(3), 560.

Alagiri, M., & Hamid, S. B. A. (2015). Sol–gel synthesis of α-Fe_2O_3 nanoparticles and its photocatalytic application. *Journal of Sol-Gel Science and Technology*, *74*(3), 783-789.

Alluhaybi, A. A., Alharbi, A., Alshammari, K. F., & El-Desouky, M. G. (2023). Efficient adsorption and removal of the herbicide 2, 4-dichlorophenylacetic acid from aqueous solutions using MIL-88 (Fe)-NH_2. *ACS omega*, *8*(43), 40775-40784.

Alp, E. (2023). Comparative study of improvement of hematite as visible light-driven photocatalyst by doping with zinc and copper. *Düzce Üniversitesi Bilim ve Teknoloji Dergisi*, *11*(1), 502-512.

Altaf, U., Ansari, M. Z., & Rubab, S. (2023). Influence of aluminium doping on structural and optical properties of tin oxide nanoparticles. *Materials Chemistry and Physics*, *297*, 127304.

Amano, F. (2021). Photoelectrochemical oxygen evolution. *Solar-to-Chemical Conversion: Photocatalytic and Photoelectrochemcial Processes*, 163-187.

Amiri, F., Dehghani, M., Amiri, Z., Yousefinejad, S., & Azhdarpoor, A. (2021). Photocatalytic degradation of 2, 4-dichlorophenoxyacetic acid from aqueous solutions by Ag_3PO_4/TiO_2 nanoparticles under visible light: kinetic and thermodynamic studies. *Water Science and Technology*, *83*(12), 3110-3122.

Amirjani, A., Amlashi, N. B., & Ahmadiani, Z. S. (2023). Plasmon-enhanced photocatalysis based on plasmonic nanoparticles for energy and environmental solutions: a review. *ACS Applied Nano Materials*, *6*(11), 9085-9123.

Aranda, A., Landers, R., Carnelli, P., Candal, R., Alarcon, H., & Rodríguez, J. (2019). Influence of silver electrochemically deposited onto zinc oxide seed nanoparticles on the

photoelectrochemical performance of zinc oxide nanorod films. *Nanomaterials and nanotechnology*, *9*, 1847980419844363.

Awan, T. I., Afsheen, S., & Mushtaq, A. (2025). Noble Metal Nanoparticles for Pollutant Decomposition. In *Influence of Noble Metal Nanoparticles in Sustainable Energy Technologies* (pp. 223-249). Springer.

Bakhtiargonbadi, F., Esfahani, H., Moakhar, R. S., & Dabir, F. (2020). Fabrication of novel electrospun Al and Cu doped ZnO thin films and evaluation of photoelectrical and sunlight-driven photoelectrochemical properties. *Materials Chemistry and Physics*, *252*, 123270.

Basak, M., Rahman, M. L., Ahmed, M. F., Biswas, B., & Sharmin, N. (2022). The use of X-ray diffraction peak profile analysis to determine the structural parameters of cobalt ferrite nanoparticles using Debye-Scherrer, Williamson-Hall, Halder-Wagner and Size-strain plot: Different precipitating agent approach. *Journal of Alloys and Compounds*, *895*, 162694.

Bashir, S., Jamil, A., Alazmi, A., Khan, M. S., Alsafari, I. A., & Shahid, M. (2023). Synergistic effects of doping, composite formation, and nanotechnology to enhance the photocatalytic activities of semiconductive materials. *Optical Materials*, *135*, 113264.

Beckie, H. J., Busi, R., Lopez-Ruiz, F. J., & Umina, P. A. (2021). Herbicide resistance management strategies: how do they compare with those for insecticides, fungicides and antibiotics? *Pest Management Science*, *77*(7), 3049-3056.

Besenhard, M. O., LaGrow, A. P., Hodzic, A., Kriechbaum, M., Panariello, L., Bais, G., Loizou, K., Damilos, S., Cruz, M. M., & Thanh, N. T. K. (2020). Co-precipitation synthesis of stable iron oxide nanoparticles with NaOH: New insights and continuous production via flow chemistry. *Chemical Engineering Journal*, *399*, 125740.

Bhat, R. S., Sajankila, S. P., & AG, B. (2025). Iron oxide (α-Fe_2O_3) nanoparticles: synthesis, characterization, and the degradation of methyl red. *Applied Physics A*, *131*(8), 1-12.

Busti, N. D., Parra, R., & Sousa Góes, M. (2021). Synthesis, properties, and applications of iron oxides: versatility and challenges. In *Functional Properties of Advanced Engineering Materials and Biomolecules* (pp. 349-385). Springer.

Chen, S.-F., Chen, W.-J., Song, H., Liu, M., Mishra, S., Ghorab, M. A., Chen, S., & Chang, C. (2024). Microorganism-driven 2, 4-D biodegradation: Current status and emerging opportunities. *Molecules*, *29*(16), 3869.

Chibania, A., Kendilb, D., Benhaouac, B., Kemerchoud, I., & Bekkare, D. (2022). Physical properties of thin films of (α-Fe_2O_3) aluminum doped by spray pyrolysis methods. *Digest Journal of Nanomaterials & Biostructures (DJNB)*, *17*(4).

Chitrada, K. C., Gakhar, R., Chidambaram, D., Aston, E., & Raja, K. S. (2016). Enhanced performance of β-Bi_2O_3 by in-situ photo-conversion to Bi_2O_3-BiO_2-x composite photoanode for solar water splitting. *Journal of The Electrochemical Society*, *163*(7), H546.

Chu, J., Liu, Z., Liu, P., Xie, J., Xiang, J., & Qiu, F. (2024). Synergistic effect of graphene enhances the responsivity of hybrid perovskite photodetector. *Cell Reports Physical Science*, *5*(7).

Coelho, E. R. C., Brito, G. M. d., Frasson Loureiro, L., Schettino Jr, M. A., & Freitas, J. C. C. d. (2020). 2, 4-dichlorophenoxyacetic acid (2, 4-D) micropollutant herbicide removing from water using granular and powdered activated carbons: a comparison applied for

water treatment and health safety. *Journal of Environmental Science and Health, Part B*, *55*(4), 361-375.

Dargahi, A., Hasani, K., Mokhtari, S. A., Vosoughi, M., Moradi, M., & Vaziri, Y. (2021). Highly effective degradation of 2, 4-Dichlorophenoxyacetic acid herbicide in a three-dimensional sono-electro-Fenton (3D/SEF) system using powder activated carbon (PAC)/Fe_3O_4 as magnetic particle electrode. *Journal of Environmental Chemical Engineering*, *9*(5), 105889.

Dargahi, A., Shokoohi, R., Asgari, G., Ansari, A., Nematollahi, D., & Samarghandi, M. R. (2021). Moving-bed biofilm reactor combined with three-dimensional electrochemical pretreatment (MBBR–3DE) for 2, 4-D herbicide treatment: application for real wastewater, improvement of biodegradability. *RSC advances*, *11*(16), 9608-9620.

De Silva, K. K. H., Huang, H.-H., & Yoshimura, M. (2018). Progress of reduction of graphene oxide by ascorbic acid. *Applied surface science*, *447*, 338-346.

Ebrahimi, R., Mohammadi, M., Maleki, A., Jafari, A., Shahmoradi, B., Rezaee, R., Safari, M., Daraei, H., Giahi, O., & Yetilmezsoy, K. (2020). Photocatalytic degradation of 2, 4-dichlorophenoxyacetic acid in aqueous solution using Mn-doped ZnO/graphene nanocomposite under LED radiation. *Journal of Inorganic and Organometallic Polymers and Materials*, *30*(3), 923-934.

Elbasuney, S., El-Sayyad, G. S., Yehia, M., & Abdel Aal, S. K. (2020). Facile synthesis of RGO-Fe_2O_3 nanocomposite: A novel catalyzing agent for composite propellants. *Journal of Materials Science: Materials in Electronics*, *31*(23), 20805-20815.

Elimian, E., Sánchez-Montes, I., & El-Din, M. G. (2025). Hybrid metal-free floatable photocatalysts for catalytic degradation of organic contaminants and inactivation of pathogens in water. *Applied Surface Science Advances*, *28*, 100811.

Favela-Camacho, S. E., Samaniego-Benítez, E. J., Godinez-Garcia, A., Avilés-Arellano, L. M., & Pérez-Robles, J. F. (2019). How to decrease the agglomeration of magnetite nanoparticles and increase their stability using surface properties. *Colloids and Surfaces A: Physicochemical and Engineering Aspects*, *574*, 29-35.

Feliczak-Guzik, A. (2022). Nanomaterials as photocatalysts—synthesis and their potential applications. *Materials*, *16*(1), 193.

Fernandez, M. E., del Rosario Morel, M., Clebot, A. C., Zalazar, C. S., & de los Milagros Ballari, M. (2022). Effectiveness of a simple biomixture for the adsorption and elimination of 2, 4-dichlorophenoxyacetic acid (2, 4-D) herbicide and its metabolite, 2, 4-dichlorophenol (2, 4-DCP), for a biobed system. *Journal of Environmental Chemical Engineering*, *10*(1), 106877.

Forti, J. C., Loretti, G. H., Tadayozzi, Y. S., & de Andrade, A. R. (2020). A phytotoxicity assessment of the efficiency 2, 4-D degradation by different oxidative processes. *Journal of environmental management*, *266*, 110588.

Ganzagh, S. G., Yousefi, A. R., Rahdar, A., & Mohammadi, M. (2025). Lignin-based nanoencapsulation for sustainable herbicide delivery: controlled release and bioactivity of 2, 4-D and MCPA compared to commercial formulations. *Scientific Reports*, *15*(1), 24532.

Gao, H., Liu, C., Jeong, H. E., & Yang, P. (2012). Plasmon-enhanced photocatalytic activity of iron oxide on gold nanopillars. *ACS nano*, *6*(1), 234-240.

Gao, H., Zhu, L., Peng, X., Zhou, X., & Qiu, M. (2022). Fe-doped WO_3 nanoplates with excellent bifunctional performances: Gas sensing and visible light photocatalytic degradation. *Applied surface science*, *592*, 153310.

Gatou, M.-A., Syrrakou, A., Lagopati, N., & Pavlatou, E. A. (2024). Photocatalytic TiO_2-based nanostructures as a promising material for diverse environmental applications: a review. *Reactions*, *5*(1), 135-194.

Girón-Navarro, R., Linares-Hernández, I., Teutli-Sequeira, E. A., Martínez-Miranda, V., & Santoyo-Tepole, F. (2021). Evaluation and comparison of advanced oxidation processes for the degradation of 2, 4-dichlorophenoxyacetic acid (2, 4-D): a review. *Environmental Science and Pollution Research*, *28*(21), 26325-26358.

Gwatidzo, V. O., Chipomho, J., & Parwada, C. (2023). Understanding mechanisms of herbicide selectivity in agro-ecosystems: A review. *Advanced Chemicobiology Research*, 79-88.

Habte, A. T., & Ayele, D. W. (2019). Synthesis and characterization of reduced graphene oxide (rGO) started from graphene oxide (GO) using the tour method with different parameters. *Advances in Materials Science and Engineering*, *2019*(1), 5058163.

Hameed, B., Salman, J., & Ahmad, A. (2009). Adsorption isotherm and kinetic modeling of 2, 4-D pesticide on activated carbon derived from date stones. *Journal of hazardous materials*, *163*(1), 121-126.

Hang, B. T., Anh, T. T., & Thang, D. H. (2021). Hydrothermal Synthesis of α-Fe_2O_3 as Anode for Fe/Air Battery. *Journal of nanoscience and nanotechnology*, *21*(4), 2545-2551.

Hosseini, S. E. (2022). Fossil fuel crisis and global warming. In *Fundamentals of low emission flameless combustion and its applications* (pp. 1-11). Elsevier.

Hosseini, S. E., & Wahid, M. A. (2020). Hydrogen from solar energy, a clean energy carrier from a sustainable source of energy. *International Journal of Energy Research*, *44*(6), 4110-4131.

Huang, W., Zhang, D., & Wang, M. (2023). A Review: Research Progress on Photoelectric Catalytic Water Splitting of α-Fe_2O_3. *Current Nanoscience*, *19*(6), 758-769.

Huong, N. T. T., Khanh, D. N. N., Vy, N. T. T., Khoa, L. H., Nghia, N. N., & Phuong, N. T. K. (2024). Application of Box–Behnken Design to Optimize Visible-Light Degradation of 2, 4-Dichlorophenoxyacetic Acid Using Hybrid CNQDs/$CuBi_2O_4$ Catalyst. *Journal of Cluster Science*, *35*(5), 1449-1462.

Irshad, I., Nazir, A., Tahir, A., Lone, A., & Want, B. (2025). Effect of Aluminium (Al)-doping on electrochemical performance of hydrothermally synthesized hematite (α-$AlxFe_2-xO_3$) nanospheres for supercapacitor application. *Journal of Energy Storage*, *107*, 114987.

Irshad, I., & Want, B. (2024). Effect of Al^{+3} substitution on optical, magnetic, and ferroelectric properties of hematite (α-$AlxFe_2- xO_3$) nanostructures. *Applied Physics A*, *130*(8), 594.

Jiang, Q., Ji, C., Riley, D. J., & Xie, F. (2018). Boosting the efficiency of photoelectrolysis by the addition of non-noble plasmonic metals: Al & Cu. *Nanomaterials*, *9*(1), 1.

Johnston, M. B., & Herz, L. M. (2016). Hybrid perovskites for photovoltaics: charge-carrier recombination, diffusion, and radiative efficiencies. *Accounts of chemical research*, *49*(1), 146-154.

Johri, M., Rajaguru, B., & Gavhane, B. (2023). IMPACT OF PESTICIDES ON THE ENVIRONMENT. *Research and Reviews in Agriculture Science Volume III*, 61.

Jorfi, S., Rahim, F., Rahmani, A., Jaafarzadeh, N., Ghaedrahmat, Z., Almasi, H., & Zahedi, A. (2021). Herbicide residues in water resources: a scoping review. *Avicenna Journal of Environmental Health Engineering*, *8*(2), 126-133.

Joseph, C. G., Farm, Y. Y., Taufiq-Yap, Y. H., Pang, C. K., Nga, J. L., & Puma, G. L. (2021). Ozonation treatment processes for the remediation of detergent wastewater: A comprehensive review. *Journal of Environmental Chemical Engineering*, *9*(5), 106099.

Kaidar, B., Imash, A., Smagulova, G., Keneshbekova, A., Kazhdanbekov, R., Yensep, E., Akalim, D., & Lesbayev, A. (2024). Magnetite-Incorporated 1D Carbon Nanostructure Hybrids for Electromagnetic Interference Shielding. *Nanomaterials*, *14*(15), 1291.

Kamble, S. P., Deosarkar, S. P., Sawant, S. B., Moulijn, J. A., & Pangarkar, V. G. (2004). Photocatalytic degradation of 2, 4-dichlorophenoxyacetic acid using concentrated solar radiation: batch and continuous operation. *Industrial & Engineering Chemistry Research*, *43*(26), 8178-8187.

Karaca, A. E. (2023). Development and analysis of novel photoelectrochemical reactor for solar based clean hydrogen production.

Kaur, N., Kumar, A., Malik, T., Girdhar, M., Singh, M., Singh, R., Tariq, M., & Mohan, A. (2025). Herbicide use and weed management strategies in hemp cultivation. *Journal of Cannabis Research*, *7*(1), 27.

Kaur, R., Singh, D., Kumari, A., Sharma, G., Rajput, S., Arora, S., & Kaur, R. (2021). Pesticide residues degradation strategies in soil and water: a review. *International Journal of Environmental Science and Technology*, 1-24.

Khan, M., & Idriss, H. (2017). Advances in plasmon-enhanced upconversion luminescence phenomena and their possible effect on light harvesting for energy applications. *Wiley Interdisciplinary Reviews: Energy and Environment*, *6*(6), e254.

Khan, U., Akbar, A., Yousaf, H., Riaz, S., & Naseem, S. (2015). Ferromagnetic properties of Al-doped Fe_2O_3 thin films by sol-gel. *Materials Today: Proceedings*, *2*(10), 5415-5420.

Kleiman-Shwarsctein, A., Huda, M. N., Walsh, A., Yan, Y., Stucky, G. D., Hu, Y.-S., Al-Jassim, M. M., & McFarland, E. W. (2010). Electrodeposited aluminum-doped α-Fe2O3 photoelectrodes: experiment and theory. *Chemistry of Materials*, *22*(2), 510-517.

Köksoy, H., & Uraz, G. (2023). Biodegradation of 2, 4-D and trifluralin herbicides by the bacteria Pseudomonas spp. using factorial design of experiments. *Journal of International Environmental Application and Science*, *18*(3), 87-99.

Koul, B., Bhat, N., Abubakar, M., Mishra, M., Arukha, A. P., & Yadav, D. (2022). Application of natural coagulants in water treatment: a sustainable alternative to chemicals. *Water*, *14*(22), 3751.

Kumar, A., Choudhary, P., Kumar, A., Camargo, P. H., & Krishnan, V. (2022). Recent advances in plasmonic photocatalysis based on TiO_2 and noble metal nanoparticles for energy conversion, environmental remediation, and organic synthesis. *Small*, *18*(1), 2101638.

Kumar, P., Thakur, N., Kumar, K., & Jeet, K. (2023). Photodegradation of methyl orange dye by using Azadirachta indica and chemically mediated synthesized cobalt doped α-Fe_2O_3 NPs through the co-precipitation method. *Materials Today: Proceedings*.

Lai, J., Xuan, S., & Leung, K. C.-F. (2022). Tunable synthesis of hematite structures with nanoscale subunits for the heterogeneous photo-Fenton degradation of azo dyes. *ACS Applied Nano Materials*, *5*(10), 13768-13778.

Lee, K. M., & Abdullah, A. H. (2015). Synthesis and characterization of zinc oxide/maghemite nanocomposites: influence of heat treatment on photocatalytic degradation of 2, 4-

dichlorophenoxyacetic acid. *Materials Science in Semiconductor Processing*, *30*, 298-306.

Li, J., Lou, Z., & Li, B. (2021). Engineering plasmonic semiconductors for enhanced photocatalysis. *Journal of Materials Chemistry A*, *9*(35), 18818-18835.

Li, R., Wang, X., & Chen, M. (2023). Non-noble metal and nonmetallic plasmonic nanomaterials with located surface plasmon resonance effects: Photocatalytic performance and applications. *Catalysts*, *13*(6), 940.

Liang, X., & Cheng, Q. (2018). Synergistic reinforcing effect from graphene and carbon nanotubes. *Composites Communications*, *10*, 122-128.

Liu, J., Jia, Y., Ji, L., Bandaru, S., Bai, G., Cheepurupalli, K. K., & Zhang, X. (2023). Study of Al-doped and Al_2O_3 heterostructures for improving α-Fe_2O_3 catalysis for the oxygen evolution reaction. *The Journal of Physical Chemistry C*, *127*(17), 8342-8351.

Liu, P., Wen, S., Zhu, S., Hu, X., & Wang, Y. (2025). Microbial Degradation of Soil Organic Pollutants: Mechanisms, Challenges, and Advances in Forest Ecosystem Management. *Processes*, *13*(3), 916.

Liu, Q., Chen, C., Yuan, G., Huang, X., Lü, X., Cao, Y., Li, Y., Hu, A., Lu, X., & Zhu, P. (2017). Morphology-controlled α-Fe_2O_3 nanostructures on FTO substrates for photoelectrochemical water oxidation. *Journal of Alloys and Compounds*, *715*, 230-236.

Liu, Y. (2023). *Defect Investigation on Hematite Photoanodes* University of Waterloo].

Magnoli, K., Carranza, C. S., Aluffi, M. E., Magnoli, C. E., & Barberis, C. L. (2020). Herbicides based on 2, 4-D: its behavior in agricultural environments and microbial biodegradation aspects. A review. *Environmental Science and Pollution Research*, *27*(31), 38501-38512.

Malindzisa, N. P. (2022). *Evaluation of glyphosate and 2, 4-Dichlorophenoxyacetic acid combinations to control glyphosate-resistant hairy fleabane [(Conyza bonariensis (L.) Cronquist]* University of Pretoria (South Africa)].

Mammar, R. B., & Hamadou, L. (2023). Highly broadband plasmonic Pt nanoparticles modified α-Fe_2O_3/TiO_2 nanotubes for efficient photoelectrochemical water splitting. *Optical Materials*, *143*, 114191.

Mamun, A. A., & Talukder, M. A. (2025). Improved photocatalytic activity of α-Fe_2O_3 by introducing B, Y, and Nb dopants for solar-driven water splitting: a first-principles study. *Materials Advances*.

Martins, R. X., Carvalho, M., Maia, M. E., Flor, B., Souza, T., Rocha, T. L., Félix, L. M., & Farias, D. (2024). 2, 4-D Herbicide-induced hepatotoxicity: unveiling disrupted liver functions and associated biomarkers. *Toxics*, *12*(1), 35.

Mathew, J. T., Inobeme, A., Shaba, E. Y., Abdullahi, A., Azeh, Y., Monday, M., Bini, E. M., Tanko, M. S., Haruna, I., & Jiya, M. J. (2025). Adsorptive Removal of Chlorinated Herbicides from Water Using Activated Carbon. In *Pesticide Removal Methods from Wastewater* (pp. 163-201). Apple Academic Press.

Matus, E., Sukhova, O., Kerzhentsev, M., Ismagilov, I., Yashnik, S., Ushakov, V., Stonkus, O., Gerasimov, E., Nikitin, A., & Bharali, P. (2022). Hydrogen production through Bi-reforming of methane: improving Ni catalyst performance via an exsolution approach. *Catalysts*, *12*(12), 1493.

Meftaul, I. M., Venkateswarlu, K., Dharmarajan, R., Annamalai, P., & Megharaj, M. (2020). Movement and fate of 2, 4-D in urban soils: A potential environmental health concern. *ACS omega*, *5*(22), 13287-13295.

Mehralipour, J., Motie, A., & Kermani, M. (2023). Optimizing the Photocatalytic Degradation of 2, 4-Dichlorophenoxyacetic Acid Herbicide from Aqueous Solution.

Mesbah, M., Sarraf, M., Dabbagh, A., Nasiri-Tabrizi, B., Paria, S., Banihashemian, S., Bushroa, A., Faraji, G., Tsuzuki, T., & Hosseini, H. M. (2020). Synergistic enhancement of photocatalytic antibacterial effects in high-strength aluminum/TiO2 nanoarchitectures. *Ceramics International*, *46*(15), 24267-24280.

Mishra, P. P., Behera, D., Suman, S., Das, N., Tripathy, B. C., Kumar, J., & Behera, A. K. (2025). Synergistic efficiency of modified banana leaf derived cellulose-gC 3 N 4 hybrid composite: a sustainable approach for visible-light-driven photodegradation of dyes. *RSC advances*, *15*(17), 13712-13727.

Mohd Ghazi, R., Nik Yusoff, N. R., Abdul Halim, N. S., Wahab, I. R. A., Ab Latif, N., Hasmoni, S. H., Ahmad Zaini, M. A., & Zakaria, Z. A. (2023). Health effects of herbicides and its current removal strategies. *Bioengineered*, *14*(1), 2259526.

Mondal, A., Prabhakaran, A., Gupta, S., & Subramanian, V. R. (2021). Boosting photocatalytic activity using reduced graphene oxide (RGO)/semiconductor nanocomposites: issues and future scope. *ACS omega*, *6*(13), 8734-8743.

Muter, O. (2023). Current trends in bioaugmentation tools for bioremediation: a critical review of advances and knowledge gaps. *Microorganisms*, *11*(3), 710.

Nag, S., Roychowdhury, A., Das, D., & Mukherjee, S. (2016). Synthesis of α-Fe2O3-functionalised graphene oxide nanocomposite by a facile low temperature method and study of its magnetic and hyperfine properties. *Materials Research Bulletin*, *74*, 109-116.

Navidpour, A. H., Abbasi, S., Li, D., Mojiri, A., & Zhou, J. L. (2023). Investigation of advanced oxidation process in the presence of TiO_2 semiconductor as photocatalyst: property, principle, kinetic analysis, and photocatalytic activity. *Catalysts*, *13*(2), 232.

Panzeri, G., Dell'Oro, R., Panzeri, A., Sansotera, M., Russo, V., Bianchi, C. L., & Magagnin, L. (2021). FeOOH modified H-TiO_2 nanorod array (NRA) for stable and improved low-bias photoelectrochemical water splitting. *Journal of The Electrochemical Society*, *168*(8), 086505.

Patil, S., & Jagadale, S. (2023). Co-precipitation methods for the synthesis of metal oxide nanostructures. In *Solution methods for metal oxide nanostructures* (pp. 39-60). Elsevier.

Patterson, B. J. (2022). Effects of Titanium Dioxide Nanoparticle Injections on Tissue Function and Morphology in Goldfish (Carassius auratus).

Pillai, R., Preetha, S., Narasimhamurthy, B., & Lekshmi, I. (2022). Biosensing of catechol via amperometry using laccase immobilized nickel oxide/graphite modified screen-printed electrodes. *Materials Today: Proceedings*, *62*, 5434-5438.

Popov, N., Ristić, M., Bošković, M., Perović, M., Musić, S., Stanković, D., & Krehula, S. (2022). Influence of Sn doping on the structural, magnetic, optical and photocatalytic properties of hematite (α-Fe_2O_3) nanoparticles. *Journal of physics and chemistry of solids*, *161*, 110372.

Qiu, P., Yao, J., Chen, H., Jiang, F., & Xie, X. (2016). Enhanced visible-light photocatalytic decomposition of 2, 4-dichlorophenoxyacetic acid over $ZnIn_2S_4$/g-C_3N_4 photocatalyst. *Journal of Hazardous Materials*, *317*, 158-168.

Rasheed, R., Al-Algawi, S., Kareem, H., & Mansoor, H. (2018). Preparation and characterization of hematite iron oxide (α-Fe2O3) by sol-gel method. *Chem. Sci. J*, *9*(4).

Sánchez-Bastardo, N., Schlögl, R., & Ruland, H. (2021). Methane pyrolysis for zero-emission hydrogen production: a potential bridge technology from fossil fuels to a renewable and sustainable hydrogen economy. *Industrial & Engineering Chemistry Research*, *60*(32), 11855-11881.

Sandoval, M. A., Vidal, J., Calzadilla, W., & Salazar, R. (2022). Solar (electrochemical) advanced oxidation processes as efficient treatments for degradation of pesticides. *Current Opinion in Electrochemistry*, *36*, 101125.

Sayed, M., Yu, J., Liu, G., & Jaroniec, M. (2022). Non-noble plasmonic metal-based photocatalysts. *Chemical Reviews*, *122*(11), 10484-10537.

Shamim, A., Neelam, K., Kamaal, S., Ali, A., & Ahmad, M. (2024). Removal of pesticide pollutants from aqueous waste utilizing nanomaterials via photocatalytic process: a review. *International Journal of Environmental Science and Technology*, *21*(4), 4653-4684.

Sharma, P., Jang, J. W., & Lee, J. S. (2019). Key strategies to advance the photoelectrochemical water splitting performance of α-Fe2O3 photoanode. *ChemCatChem*, *11*(1), 157-179.

Sharma, S., Agarwal, S., & Jain, A. (2021). Significance of hydrogen as an economic and environmentally friendly fuel. *Energies*, *14*(21), 7389.

Shimizu, S., & Matubayasi, N. (2022). Surface area estimation: replacing the Brunauer–Emmett–Teller model with the statistical thermodynamic fluctuation theory. *Langmuir*, *38*(26), 7989-8002.

Silva, M. J., Alves, P., Gomes, J., Ferreira, P., & Martins, R. C. (2024). Evaluation of the reusability of photocatalytic P25/PDMS membranes when hindering their hydrophobic recovery. *Catalysis Today*, *432*, 114580.

Sim, H. J., Li, Z., Xiao, P., & Lu, H. (2022). The influence of lateral size and oxidation of graphene oxide on its chemical reduction and electrical conductivity of reduced graphene oxide. *Molecules*, *27*(22), 7840.

Singh, P. K., Kumar, U., Kumar, I., Dwivedi, A., Singh, P., Mishra, S., Seth, C. S., & Sharma, R. K. (2024). Critical review on toxic contaminants in surface water ecosystem: sources, monitoring, and its impact on human health. *Environmental Science and Pollution Research*, *31*(45), 56428-56462.

Singh, S. (2021). Energy crisis and climate change: Global concerns and their solutions. *Energy: crises, challenges and solutions*, 1-17.

Soltani, T., Tayyebi, A., & Lee, B.-K. (2018). Efficient promotion of charge separation with reduced graphene oxide (rGO) in $BiVO_4$/rGO photoanode for greatly enhanced photoelectrochemical water splitting. *Solar Energy Materials and Solar Cells*, *185*, 325-332.

Song, H., Luo, S., Huang, H., Deng, B., & Ye, J. (2022). Solar-driven hydrogen production: recent advances, challenges, and future perspectives. *ACS Energy Letters*, *7*(3), 1043-1065.

Stucchi, M., Meroni, D., Safran, G., Villa, A., Bianchi, C. L., & Prati, L. (2022). Noble Metal Promoted TiO_2 from Silver-Waste Valorisation: Synergism between Ag and Au. *Catalysts*, *12*(2), 235.

Sun, D., Jia, L., Wang, C., Liu, H., & Chen, R. (2021). Preparation of the additive-modified α-Fe_2O_3/g-C_3N_4 Z-scheme composites with improved visible-light photocatalytic activity. *Journal of Environmental Chemical Engineering*, *9*(5), 106274.

Synowiec, M., Zákutná, D., Trenczek-Zajac, A., & Radecka, M. (2023). The impact of nanometric Fe_2O_3 on the magnetic, electronic, and photocatalytic behavior of TiO_2@ Fe_2O_3 heterostructures. *Applied surface science*, *608*, 155186.

Székács, A. (2021). Herbicide mode of action. In *Herbicides* (pp. 41-86). Elsevier.

Tahir, D., Heryanto, H., Ilyas, S., Fahri, A. N., Rahmat, R., Rahmi, M. H., Taryana, Y., & Sukaryo, S. G. (2021). Excellent electromagnetic wave absorption of Co/Fe_2O_3 composites by additional activated carbon for tuning the optical and the magnetic properties. *Journal of Alloys and Compounds*, *864*, 158780.

Tamboli, A. M., Tamboli, M. S., Shinde, S. K., Byeon, J., Truong, N. T. N., Kim, C., & Park, C. (2022). Uniform and fully decorated novel Li-doped α-Fe_2O_3 nanoparticles for high performance supercapacitors. *Journal of Alloys and Compounds*, *928*, 167242.

Tho, N. T. M., Khanh, D. N. N., Thang, N. Q., Lee, Y.-I., & Phuong, N. T. K. (2020). Novel reduced graphene oxide/$ZnBi_2O_4$ hybrid photocatalyst for visible light degradation of 2, 4-dichlorophenoxyacetic acid. *Environmental Science and Pollution Research*, *27*(10), 11127-11137.

Trivedi, N. S., Kharkar, R. A., & Mandavgane, S. A. (2019). 2, 4-Dichlorophenoxyacetic acid adsorption on adsorbent prepared from groundnut shell: Effect of preparation conditions on equilibrium adsorption capacity. *Arabian Journal of Chemistry*, *12*(8), 4541-4549.

Tufa, L. T., Oh, S., Kim, J., Jeong, K.-J., Park, T. J., Kim, H.-J., & Lee, J. (2018). Electrochemical immunosensor using nanotriplex of graphene quantum dots, Fe3O4, and Ag nanoparticles for tuberculosis. *Electrochimica Acta*, *290*, 369-377.

Uma, K., Chong, S., Mohan, S. C., Jothivenkatachalam, K., Yang, T. C.-K., & Lin, J.-H. (2020). Multi-functional RGO-supported α-Fe_2O_3 nanocomposites for high-performance pseudocapacitors and visible light–driven photocatalytic applications. *Ionics*, *26*(7), 3491-3500.

Upendranath, K., Vishwanath, R., Ravitheja, G., Lamani, A., Sriram, G., Oh, T. H., Kurkuri, M. D., & Altalhi, T. (2024). Sol-gel synthesis of $LaFeO_3$ perovskite oxide for distinct ridges detection of level II and III latent fingerprints. *Inorganic Chemistry Communications*, *170*, 113210.

Vanitha, T., Suresh, G., Bhandi, M. M., Mudiam, M. K. R., & Mohan, S. V. (2023). Microbial degradation of organochlorine pesticide: 2, 4-Dichlorophenoxyacetic acid by axenic and mixed consortium. *Bioresource Technology*, *382*, 129031.

Verma, M. D., Ranjan, K. R., Mukherjee, D. M. D., & Solanki, D. P. R. (2022). Bioinspired synthesis of hematite nanoparticles-reduced graphene oxide composite for application in Bpa detection: a new in-sight. *Available at SSRN 4134082*.

Vinayagam, R., Sharma, G., Murugesan, G., Pai, S., Gupta, D., Narasimhan, M. K., Kaviyarasu, K., Varadavenkatesan, T., & Selvaraj, R. (2022). Rapid photocatalytic degradation of 2, 4-dichlorophenoxy acetic acid by ZnO nanoparticles synthesized using the leaf extract of Muntingia calabura. *Journal of Molecular Structure*, *1263*, 133127.

Vinoth, R., Karthik, P., Muthamizhchelvan, C., Neppolian, B., & Ashokkumar, M. (2016). Carrier separation and charge transport characteristics of reduced graphene oxide supported visible-light active photocatalysts. *Physical Chemistry Chemical Physics*, *18*(7), 5179-5191.

Wan, H., Hu, L., Liu, X., Zhang, Y., Chen, G., Zhang, N., & Ma, R. (2023). Advanced hematite nanomaterials for newly emerging applications. *Chemical Science*, *14*(11), 2776-2798.

Wang, L., Zhou, X., Nguyen, N. T., & Schmuki, P. (2015). Plasmon-Enhanced Photoelectrochemical Water Splitting Using Au Nanoparticles Decorated on Hematite Nanoflake Arrays. *ChemSusChem*, *8*(4), 618-622.

Wang, M., Ye, M., Iocozzia, J., Lin, C., & Lin, Z. (2016). Plasmon-mediated solar energy conversion via photocatalysis in noble metal/semiconductor composites. *Advanced Science*, *3*(6), 1600024.

Wang, Y., Wang, S., Wu, Y., Wang, Z., Zhang, H., Cao, Z., He, J., Li, W., Yang, Z., & Zheng, L. (2021). A α-Fe2O3/rGO magnetic photocatalyst: enhanced photocatalytic performance regulated by magnetic field. *Journal of Alloys and Compounds*, *851*, 156733.

Wu, Q., He, T., Zhang, Y., Zhang, J., Wang, Z., Liu, Y., Zhao, L., Wu, Y., & Ran, F. (2021). Cyclic stability of supercapacitors: materials, energy storage mechanism, test methods, and device. *Journal of Materials Chemistry A*, *9*(43), 24094-24147.

Wu, T., Han, M.-Y., & Xu, Z. J. (2022). Size effects of electrocatalysts: more than a variation of surface area. *ACS nano*, *16*(6), 8531-8539.

Wyżga, P., Macyk, J., Lin, Y.-C., Jensen, E. H., Guzik, M. N., Bieńkowski, K., Solarska, R., & Macyk, W. (2024). 3D-Printed Reactor for Coupling Photoelectrochemical (Sea) Water Splitting with Solid-State H_2 Storage. *Catalysts*, *14*(12), 941.

Xi, Z., & Liu, M. (2025). Advancing photoelectrochemical systems for sustainable energy and chemical production: challenges and opportunities. *npj Materials Sustainability*, *3*(1), 18.

Yang, Z., Chen, Y., Zhang, S., & Zhang, J. (2023). Identification and understanding of active sites of non-noble iron-nitrogen-carbon catalysts for oxygen reduction electrocatalysis. *Advanced Functional Materials*, *33*(26), 2215185.

Yasmeen, S., Burratti, L., Duranti, L., Agresti, A., & Prosposito, P. (2024). Study of photodegradation of bentazon herbicide by using ZnO-Sm2O3 nanocomposite under UV light. *International Journal of Molecular Sciences*, *25*(24), 13319.

Ye, K.-H., Wang, Z., Li, H., Yuan, Y., Huang, Y., & Mai, W. (2018). A novel CoOOH/(Ti, C)-Fe_2O_3 nanorod photoanode for photoelectrochemical water splitting. *Science China Materials*, *61*(6), 887-894.

Ye, Q., Yang, M., Li, W., Dong, Z., Qi, W., & Zhao, L. (2022). Heterogeneous irradiation system: enhanced degradation of methylene blue by electron beam irradiation combined with graphite carbon nitride/carbon nanodots. *Environmental Science and Pollution Research*, *29*(39), 58762-58772.

Yin, J., Wang, N., Lin, C., Liu, W., Myung, S.-T., & Jin, Y. (2023). Aluminium-doping induced micro-porous structure and improved anion redox reversibility in cobalt-free lithium-rich cathode materials for their enhanced electrochemical performance. *Chemical Engineering Journal*, *474*, 145552.

Yuan, J.-T., Wang, Z., Wang, L., & Liu, R.-J. (2020). Preparation, surface modification, and characteristics of α-Fe_2O_3 nanoparticles. *Journal of nanoscience and nanotechnology*, *20*(5), 3031-3037.

Yuan, Y., Liang, S., Liu, W., Zhao, Q., Peng, P., Ding, R., Gao, P., Sun, X., & Liu, E. (2021). Al-Doped Fe_2O_3 nanoparticles: advanced anode materials for high-capacity lithium-ion batteries. *Dalton Transactions*, *50*(15), 5115-5119.

Zada, A., Muhammad, P., Ahmad, W., Hussain, Z., Ali, S., Khan, M., Khan, Q., & Maqbool, M. (2020). Surface plasmonic-assisted photocatalysis and optoelectronic devices with

noble metal nanocrystals: design, synthesis, and applications. *Advanced Functional Materials*, *30*(7), 1906744.

Zhang, L., Zhang, J., Yu, H., & Yu, J. (2022). Emerging S-scheme photocatalyst. *Advanced materials*, *34*(11), 2107668.

Zhang, M., Zhao, F., Yang, Y., Li, H., An, T., & Zhang, J. (2021). The effect of rGO-Fe_2O_3 nanocomposites with spherical, hollow and fusiform microstructures on the thermal decomposition of TKX-50. *Journal of physics and chemistry of solids*, *153*, 109982.

Zhang, T., Xu, M., & Li, J. (2021). Enhanced photocatalysis of TiO2 by aluminum plasmonic. *Catalysis Today*, *376*, 162-167.

Zhao, J., Xue, S., Ji, R., Li, B., & Li, J. (2021). Localized surface plasmon resonance for enhanced electrocatalysis. *Chemical Society Reviews*, *50*(21), 12070-12097.

Zheng, M., & Fang, G. (2021). Luminescence enhancement of lead halide perovskite light-emitting diodes with plasmonic metal nanostructures. *Nanoscale*, *13*(39), 16427-16447.

Zhou, H., Sheng, X., Xiao, J., Ding, Z., Wang, D., Zhang, X., Liu, J., Wu, R., Feng, X., & Jiang, L. (2020). Increasing the efficiency of photocatalytic reactions via surface microenvironment engineering. *Journal of the American Chemical Society*, *142*(6), 2738-2743.

Zhou, X., Liu, G., Yu, J., & Fan, W. (2012). Surface plasmon resonance-mediated photocatalysis by noble metal-based composites under visible light. *Journal of Materials Chemistry*, *22*(40), 21337-21354.

Zhu, Z., Guo, F., Xu, Z., Di, X., & Zhang, Q. (2020). Photocatalytic degradation of an organophosphorus pesticide using a ZnO/rGO composite. *RSC advances*, *10*(20), 11929-11938.

Zong, H., Gao, X., Liu, Q., Hao, Y., Hao, G., Wang, S., Zhou, H., Xiao, L., & Jiang, W. (2022). Preparation of rGO, Fe2O3, and Fe2O3/rGO for the catalytic thermal decomposition of microspherical TKX-50. *Journal of Thermal Analysis and Calorimetry*, *147*(22), 12779-12790.

Appendix

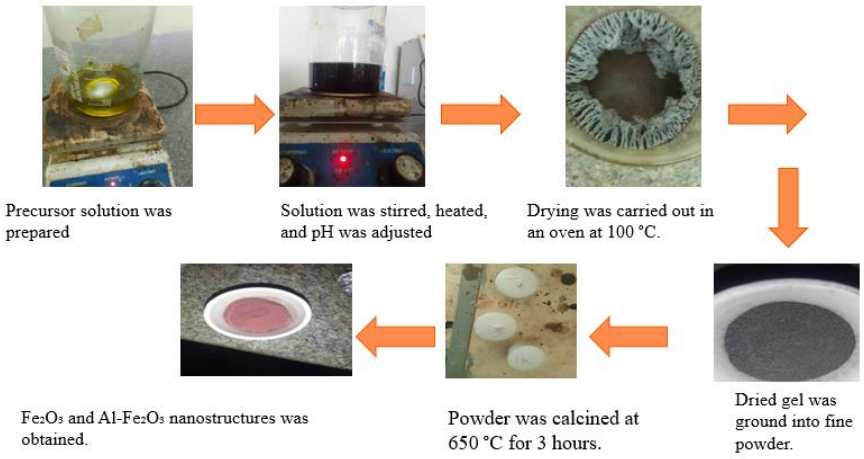

Figure 7. 1. Synthesis procedure for Fe_2O_3 and Al-Fe_2O_3 by sol-gel method

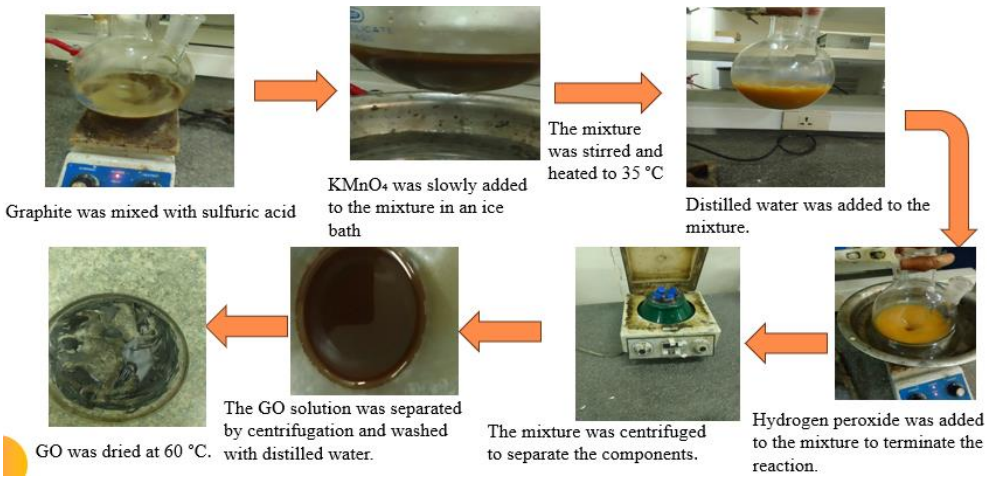

Figure 7. 2. Synthesis graphene oxide (GO) by modified Hummers' method

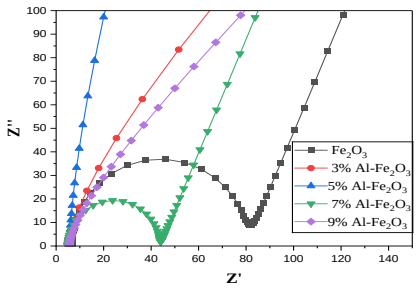

Figure 7. 3. EIS of Fe_2O_3 with different concentration of Al doping

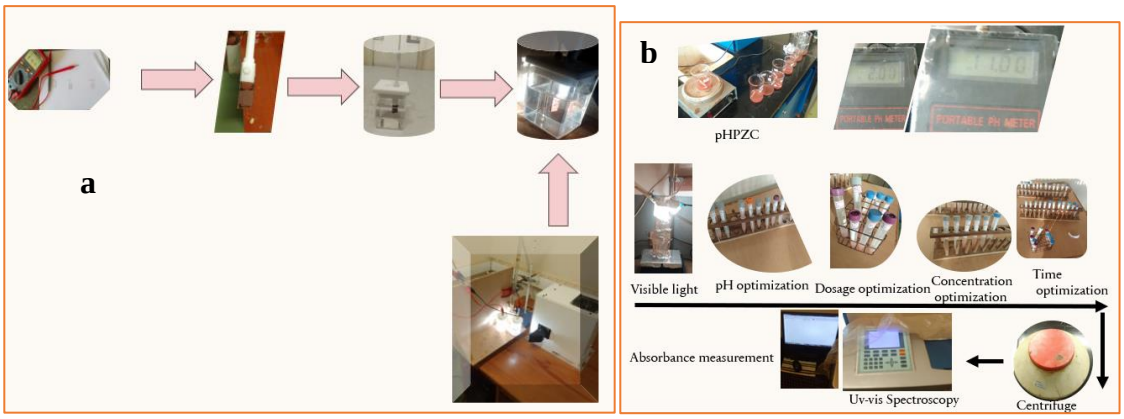

Figure 7.4.Preparation of Fe_2O_3/Al–Fe_2O_3/Al–Fe_2O_3/rGO (a)photoanode and PEC test and (b)Photocatalytic experimental procedure of 2,4-D